Performance of Armor Materials for the ITER Divertor

by

KATHRYN ELEANOR HAUTANEN

B.S. University of Massachusetts at Amherst
(1988)

M.S. University of Wisconsin - Madison
(1990)

SUBMITTED TO THE DEPARTMENT OF
NUCLEAR ENGINEERING IN PARTIAL
FULFILLMENT OF THE
REQUIREMENTS FOR THE
DEGREE OF

MASTER OF SCIENCE

at the

MASSACHUSETTS INSTITUTE OF TECHNOLOGY

December 12, 1995

© Massachusetts Institute of Technology 1995

Signature of Author
Department of Nuclear Engineering

Certified by
Professor Mujid Kazimi
Department of Nuclear Engineering
Thesis Advisor

Certified by
Professor John Meyer
Department of Nuclear Engineering
Thesis Advisor

Accepted by
Professor Jeffrey Freidberg
Chairman, Department Committee on Graduate Students
Department of Nuclear Engineering

MASSACHUSETTS INSTITUTE
OF TECHNOLOGY

APR 22 1996

LIBRARIES

Science

Performance of Armor Materials for the ITER Divertor

by

Kathryn Eleanor Hautanen

Submitted to the Department of Nuclear Engineering on December 12, 1995
in Partial Fulfillment of the Requirements for the Degree of
Master of Science in Nuclear Engineering

Abstract

Neutronic analyses using MCNP4A were performed on the TAC-4 design of the International Thermonuclear Experimental Reactor (ITER) divertor. The purpose of this study was to compare the performance of three candidate materials, graphite, beryllium and tungsten, in the divertor environment. The focus of the study was the effect of neutron damage on the mechanical properties, using the displacements per atom (dpa) as the method of determination. From this calculation of dpa, an extrapolation to published data under a fast fission fluence was done. In general, the graphite divertor showed a severe decrease in its thermal conductivity. The effects of this decrease in thermal conductivity on the heat transfer properties of a graphite armor were calculated. The maximum allowable thickness of a graphite armor given this degradation in the thermal conductivity was determined and the evolution of the surface temperature over a full power year was calculated.

The code DKR-PULSAR was then used with input flux from MCNP to determine the activation and the afterheat for the materials. The pulsing scheme modeled was 1000 pulses of 1000 seconds in duration with a 2200 second turnaround time. Results show that tungsten is the most highly activated. In general, the tungsten has an activity two orders of magnitude higher than the beryllium which in turn has an activity approximately two orders of magnitude higher than the graphite.

The important materials issues for each of the candidate materials have been determined and recommendations as to materials selection for the ITER divertor have been made. Due to its extreme levels of activation, the use of tungsten as an armor must be minimized.

Thesis Supervisors:	Professor Mujid Kazimi	Professor John Meyer
Titles:	Professor of Nuclear Engineering	Professor of Nuclear Engineering

Acknowledgments

I would like to thank Professors Mujid Kazimi and John Meyer for their unfailing support and encouragement. Their attention to detail proved to be a great asset in this thesis work. I also deeply appreciate discussions with Professor Kenneth Russell on general nuclear materials issues. Discussions with Dr. Robert Granetz were also helpful towards my understanding of related plasma phenomena.

Dr. Mohamed Sawan from the University of Wisconsin also proved to be an invaluable asset for the MCNP modeling. Without his help with the ITER model I am sure this work never would have been completed. I would also like to thank Professor Paul Henderson at the University of Wisconsin for supplying the DKR-PULSAR code and computational run-time on the HP-753/99 computer.

There are always those whom without their support this work never would have been completed. In this case, much of the credit has to go to the staff at the Plasma Fusion Center Library: Jason Thomas and Kathy Powers. After three million (it seems) database searches and sending them off after truly obscure footnotes, they *still* seemed glad to see me whenever I entered the library. I also truly appreciate the cookies — they did make me feel better!

I would like to thank those students of the Nuclear Engineering Department that I drove insane with my never-ending questions: Everett Redmond II, Stead Kiger, and Eric Iverson. Special thanks to Brett Mattingly for sparing a few hours on Toolboy with the minimum of groveling on my part. I would like to single out Bilal Bhutta for all his help with Neutron, MCNP, the Cray, my Macintosh and the chocolate.

Last, but not least, I send my apologies to all the trees and sand particles that sacrificed themselves for this work.

TABLE OF CONTENTS

LIST OF FIGURES

LIST OF TABLES

'The time has come,' the Walrus said,
'To talk of many things:
Of shoes—and ships—and sealing-wax—
Of cabbages–and kings–
And why the sea is boiling hot–
And whether pigs have wings.'

Lewis Carroll

CHAPTER 1

'Where should I begin, please your Majesty?' he asked.
'Begin at the beginning,' the King said, gravely, 'and
go on till you come to the end: then stop.'
Lewis Carroll

Introduction

1.1 Objective

The objective of the present study is to examine those material qualities that are important for the design and good operation of a divertor for the International Thermonuclear Experimental Reactor (ITER). Many studies have investigated the unique qualities of the environment and the divertor operation in them. However, very few have taken into account the fact that the materials properties are not constant in time. Since the divertor is in a high neutron irradiation environment, many of the material properties will degrade under operation. A few general changes that can be expected are a decrease in thermal conductivity, a decrease in the heat capacity, swelling and hardening, and activation. Therefore, in order to design properly the divertor for heat removal this evolution of physical and mechanical properties must be accounted for. This evolution of properties due to intense neutron radiation is the focus of this study.

1.2 Background

Fusion has been under investigation for many years as a potential energy source. While fission is well engineered and understood physically - fusion has proved to be a much more challenging concept. The engineering complexity that is involved in the design of a fusion reactor is much greater than that involved in other engineering designs. Also, the underlying physics of fusion is poorly understood. Fusion has been the object of intense study for over 40 years and the scientific community is still not close to building a power producing reactor. One crucial step in the design and construction of a power producing reactor is to construct an experimental reactor to investigate the engineering and physics problems on an appropriate scale . There has been an international effort since the late 1980's to design a large scale prototype thermonuclear reactor. This reactor, the International Thermonuclear Experimental Reactor, ITER, is of a scale previously unheard of in the fusion community. Chapter 2 will discuss the design of ITER in detail.

A fusion reactor has many components - many of which are important. However, one component that is a subject of intense investigation is the divertor. The purpose of a divertor is to prevent impurities from entering the plasma. Its operation is crucial in order to achieve ignition. However, by its very design, the divertor is in the most harsh environment out of the reactor components. It is a very difficult engineering design problem because of:

1. high erosion due to incoming high energy particles;
2. thermal fatigue due to a cyclic working condition;
3. neutron damage and hence changes in materials properties; and
4. activation of materials.

1.3 Scope

Though the design of ITER has yet to be confirmed, in order to perform this study it was necessary to select a design to base this work on. Therefore, the design selected was the most current at the start of this work, i.e. the design presented at the Fourth Meeting of the Technical Advisory Committee, January 10-12, 1994 - hereafter referred to as TAC-4.[1]

While the divertor is designed to be a removable component of the reactor, the removal is still a costly and time consuming procedure. The replacement time for one casette is to be less than eight weeks, and the replacement time for the entire divertor is to be less than six months.[2] Therefore, it is crucial that the divertor be of a robust design to withstand this operating environment for an acceptable minimum time without failure. Therefore, the scope of this study is to examine the material changes in the divertor armor during one year of operation. These changes include: atomic displacements generation from neutron irradiation and consequent material properties changes, transmutation, heat transfer properties and erosion.

CHAPTER 2

Simplify, simplify.
Henry David Thoreau

The ITER Divertor

2.1 Description of ITER

The purpose of ITER is "to demonstrate the scientific and technological feasibility of fusion energy for peaceful purposes."[1] ITER would show this by demonstrating controlled ignition and extended burn of deuterium-tritium plasmas. It would also allow for the demonstration of technologies essential to a reactor integrated system, and for the testing of the high heat-flux and nuclear components. The principal parameters of ITER are listed in Table 2.1. While 1.5 GW is listed as the nominal fusion power, there are actually three operational modes. Initially ITER will operate under ohmic operation which will have a fusion power of 7.9 MW, this will be followed by a Basic Performance Phase (BPP) which will have a fusion power of 1.5 GW, and finally ITER will operate in a Enhanced Performance Phase (EPP) which will have a fusion power of 3.0 GW. The toroidal cross section is shown in Figure 2.1.

Table 2.1: Principal Parameters of the ITER Design

Fusion Power (nominal)	1.5 GW
Burn Time (nominal)	1000 seconds
Plasma Current	24 MA
Plasma Current Pulse Duration (t_{pulse})	1400 s (at I=24MA)
Pulse repetition period	≥ 2200 s
Major Radius (nominal)[1]	7.7 m
Plasma Major Radius (R_o)	8.1 m
Plasma Minor Radius (a)	3.0 m
Elongation (κ)	1.6
Divertor Configuration	Single Null
Toroidal Field at R_o	5.7 Tesla
Toroidal Field Ripple at plasma edge	± 2%

---

[1] The major radius is defined as the barycenter of the plasma cross section.

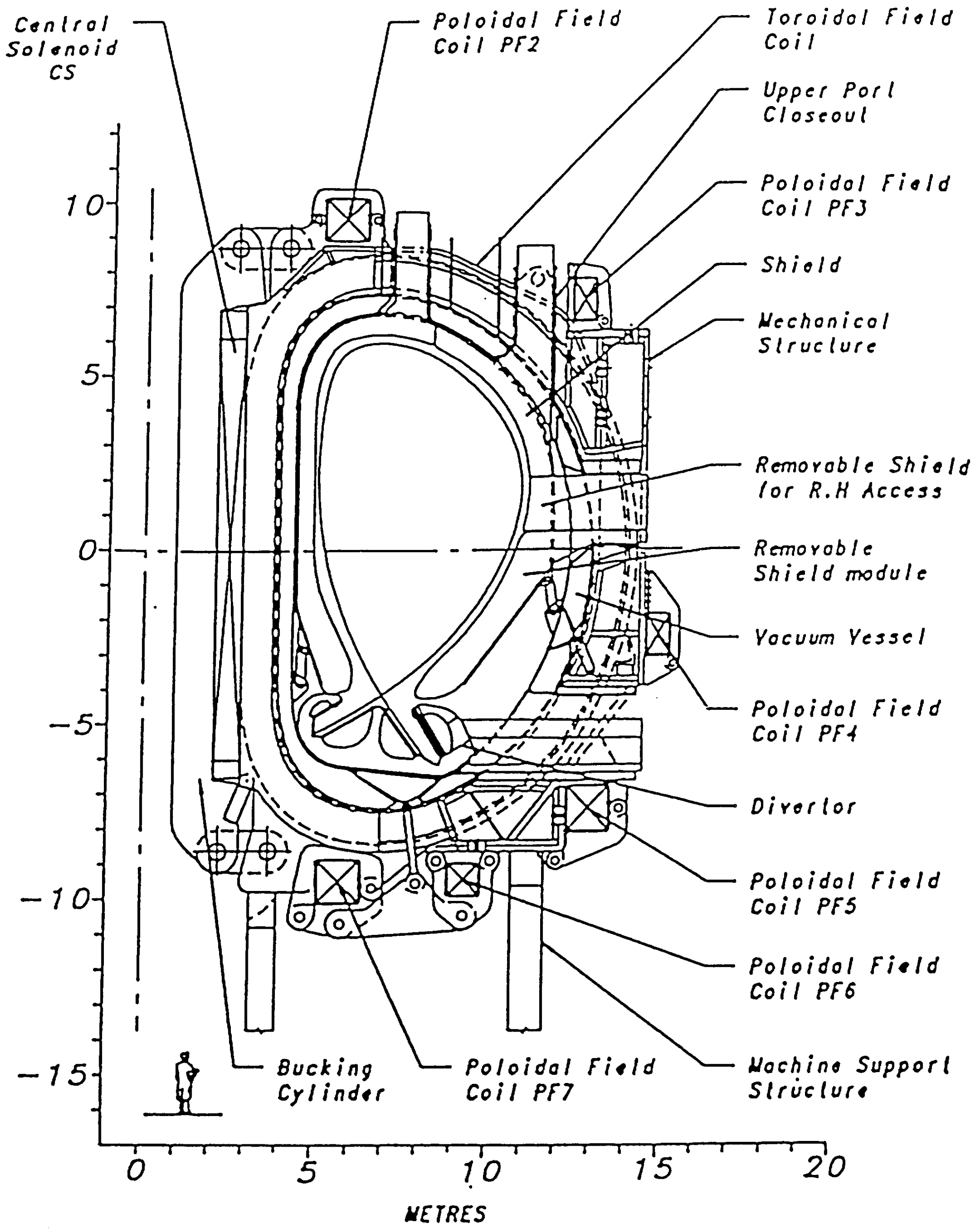

Figure 2.1: ITER Toroidal Cross Section. Note the location of the divertor.[1]

2.2 Divertor

The design of the divertor for any large scale reactor, such as ITER, has been recognized as a very difficult engineering challenge. The role of divertor is to direct particle and energy flows along the open magnetic field lines in the scrape-off layer to a remote target and pumping region. The plasma interacts with the surface of the divertor and causes sputtering. The open field lines and their angle on incident to the divertor are shown in in Figure 2.2. Note that the field lines intercept the energy dump targets. Therefore, the particles that are following these field lines will be directed straight onto these dump targets. Also, note that the divertor dome directly faces the main vacuum chamber. This divertor dome will also have large particle fluxes. Thus the role of the divertor is to separate this major source of impurities from the main plasma, to obtain high power exhaust and high helium pumping and to allow the rapid re-circulation of tens of milligrams of tritium per second. [1]

The purpose of the ITER divertor is to exhaust the majority (60 - 80 %) of the alpha particle power (P_α ~ 300 MW nominally, but as much as ~ 600 MW at the beta limit). This translates to a power load of 40 - 60 MW/m^2 on the energy dump targets when perpendicular to the magnetic field lines. While this load can be reduced by tilting the targets, space constraints limit the amount that the plates can be tilted. Due to these limitations, the maximum tilting possible can reduce the load by only a factor of 3. This reduction translates to a peak load of ~ 15 - 20 MW/m^2 striking the divertor dump targets. In order to withstand this heat load, the cladding of the Cu high heat flux components must be very thin (~ 2 mm for Be or W, 5 mm C) which leads to a very short component lifetime.

In addition to normal operation, the divertor must also be able to withstand partial or complete loss of particle confinement of the main plasma. The partial loss of plasma confinement, specifically a giant edge localized mode (ELM), can deposit ~ 14 MJ/m^2 on the divertor targets. The total loss of main plasma confinement, a disruption, can deposit ~140 MJ/m^2 on the target plates within 0.1 to 3 ms. This deposition of a large amount of energy would cause evaporation and surface melting (Be and W) or sublimation (C), thus reducing the thickness of the cladding on the high heat flux components and hence, the working lifetime of the divertor. An acceptable lifetime would be > 500 disruptions, so that the cladding must be as thick as possible (1 cm Be or W, 4 cm C), thus reducing the steady state heat removal capability to 5 MW/m^2. The maximum thickness is limited in order to avoid melting or sublimation of the cladding.

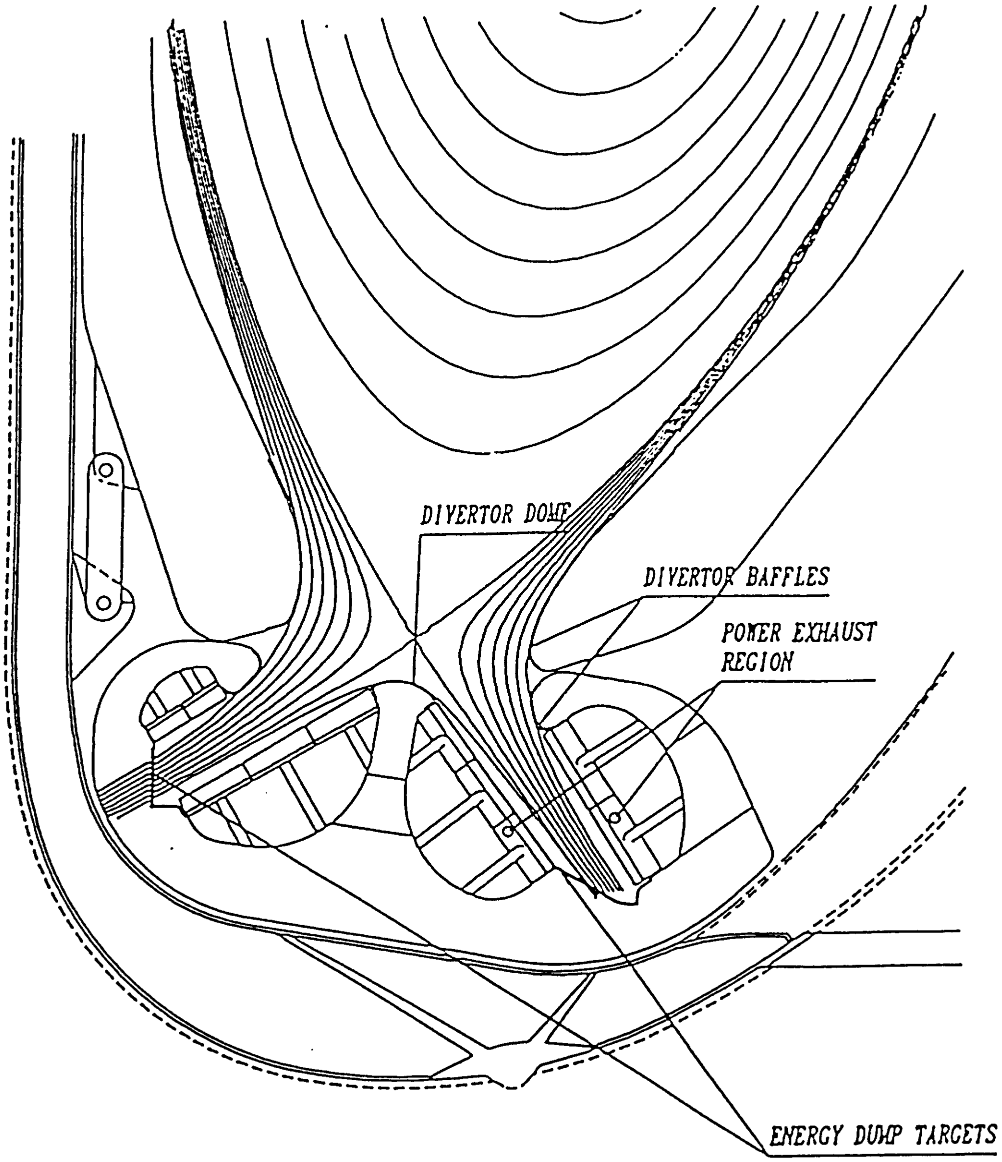

Cross-section through a divertor cassette showing the baffle, the dome, the power exhaust region and the energy dump targets

Figure 2.2 Cross section of the divertor. The energy dump targets and the dome are the components of interest.[1]

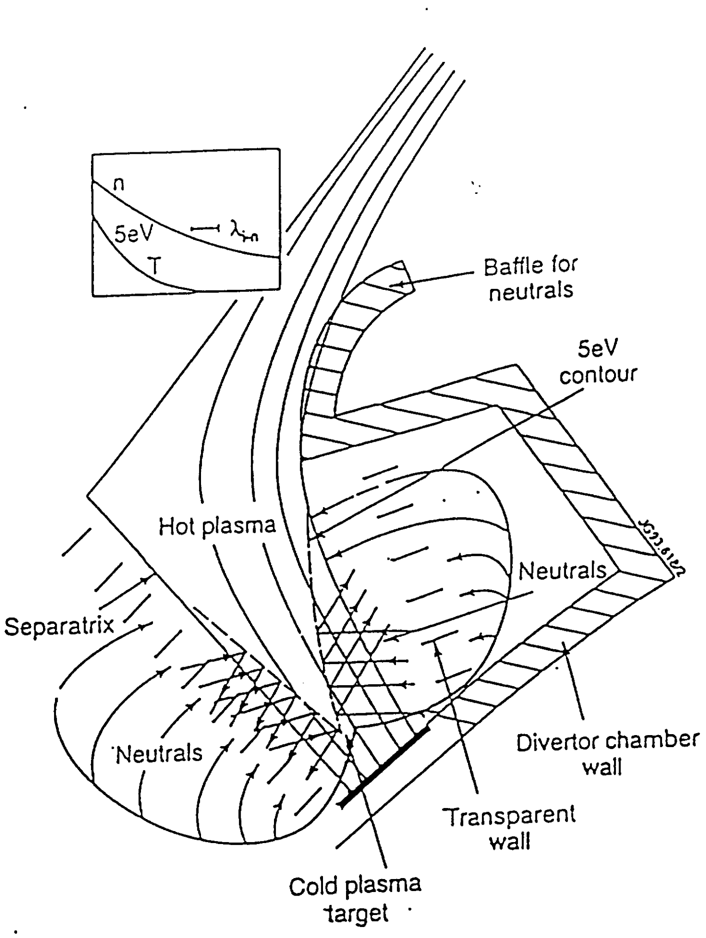

Figure 2.3 Flame-like ionization front that is formed above divertor energy dump target.[1]

It could be thought that hydrogen or deuterium would be an ideal gas to inject, since it would not introduce large amounts of impurities into the main plasma. However, there is only ~ 50 eV energy loss per ion/electron pair created and ~ 400 eV per charge exchange event. Therefore, a large amount of gas would have to be introduced to see any appreciable decrease in power. This large amount of gas could also drive the plasma to the density limit. An increase in core density is seen with D_2 injection in DIII-D experiments.[3] A better choice for injection is either neon or argon which has high radiation rates compared to hydrogen. As neon and argon are noble gases, they do not get trapped in walls and thus recycle, so the impurity concentration control would also be good. Experiments with Ne injection in DIII-D show a decrease by a factor of three of the average heat loads striking the divertor while the confinement time, τ_E, remains nearly constant.[3]

It is feasible that a mixture of Ne and Ar could provide an approximately constant radiation rate of 10^{-19} W/m^3 between 10 and 30 eV.[4] If this gas mixture were injected into the ITER divertor such that an impurity concentration of 1% were achieved, the radiated power would exceed 40% of the power flow across the separatrix.[4] However, it is very difficult to maintain

2.3 Dynamic Gas Target Divertor

The gaseous divertor concept has been studied for ITER and is referred to as a "dynamic gas target." The general idea of a gaseous divertor is to puff a neutral gas in front of the divertor. The high energy plasma which interacts with this neutral gas will transfer its energy through collision that cause the ionization of these formerly neutral particles. This will cause energy to radiate away in the form of X-rays. It is hoped that the temperature of the electrons within the plasma may be reduced to temperatures less than 5 eV through this process. This reduction in temperature of the plasma striking the divertor would decrease the peak heat flux and also the material losses through sputtering.

While the concept appears quite simple, satisfying the requirements for its success is quite a challenge. In order for high radiation losses to be achieved outside of closed flux surfaces, the total plasma pressure must drop by approximately an order of magnitude. This pressure reduction, which is equivalent to a decrease in the flux onto the target, can be achieved through the interaction of the divertor plasma with neutral particles as mentioned above. The electron temperature must remain below 5 eV for this change in density and flux to occur with reasonable neutral and plasma densities. Experiments have shown that T_e below 5 eV in the divertor can be achieved through impurity radiation. This onset of temperatures less than 5 eV is at a flame-like ionization front well above the divertor target. This 5 eV ionization front is shown in Figure 2.3.

A gaseous divertor can be explained as follows. The divertor region plasma can be cooled by the injection of a neutral gas into the divertor channel. For best circulation, the divertor design of choice would be a slot design, which is currently the model for ITER. This neutral gas would become ionized and would thus radiate away heat. Several modes of energy loss are achieved by gas injection: excitation, dissociation, ionization, charge exchange and elastic ion/neutral collisions.[4] The former remove energy from the plasma electrons, and the latter two remove energy from the plasma ions. The injection of the gas could also increase cross field ion transport through collisional transport or turbulence.

the plasma impurity-free. Only a 1% concentration of Ar in the main plasma would cause excessive energy loss and fuel dilution.[4]

2.4 L-H Transition and Edge Localized Modes

There exists an enhanced confinement mode in tokamak operation that is referred to as "H-mode" or high-mode where the other mode is referred to as "L-mode" or low mode. The plasma alternates between these modes in one confinement time. When the plasma undergoes the transition between L mode to H mode, the following changes occur. A transport barrier is set up at the edge of the plasma which is characterized by a sudden increase in density and a sharp drop in particle ionization at the plasma boundary. Also, very steep density and temperature gradients are created at the edge. An enhanced confinement time (factor of 2) is indicated by an increase in plasma stored energy without any change in input power. Due to the increased confinement time and the improved particle confinement, there is an increase in the number of impurities, thus an increase in radiated power from the main plasma.[5]

Since there is improved particle and energy confinement, the plasma density begins to rise uncontrollably, which if not balanced by an increase in input power will lead to a decrease in plasma energy. Also, there is energy loss from the impurity particles, (P_{rad}). Both of these phenomena can lead to a reversion to L-mode, due to excessive energy loss from the plasma. The transport barrier at the edge can also cause some difficulties. The density profile leads to very steep gradients just inside the separatrix; therefore, the pressure gradient, dp/dr, can grow very large at the edge. If this gradient grows too large, it can lead to a ballooning mode instability, which is known as an edge localized mode, or an ELM. The ELMs result in a rapid reduction of $\bar{n}_e$, τ_E, and impurity concentrations though the ejection of particles from the edge of the plasma.

There are two types of ELMs, giant and grassy. Giant ELMs are rather infrequent and cause large perturbations to the plasma. Grassy ELMs occur at a high, regular repetition rate. The effect of each grassy ELM is rather small, but their repetitive nature can be of due to their overall effect on the plasma.[5] Yet, ELMs are not necessarily bad for the plasma. In an ELM-free plasma the $\bar{n}_e$, and P_{rad} continue to increase causing a transition back to L-mode after ~ 100 μs. In a plasma with grassy ELMs, both the density and the impurity radiation remain well-controlled in H-mode; however, the confinement is slightly less than a factor of two greater than L-mode. In a plasma with grassy ELMs - which have been sustained for 10 seconds or longer, density and impurity concentrations remain in a steady state. Therefore, if a reactor such as ITER requires the improved confinement time offered by H-mode, it may be necessary to have ELMs in order to operate in steady state. However, these puffs of particles being rejected regularly from the plasma may have some effect on the divertor lifetime.

Regular giant ELMs would place a limit on the divertor lifetime. A 1000s discharge would have ~ 220 ELMs (if there was one every confinement time), each depositing greater than 14 MJ/m^2. These 220 ELMs would erode approximately 500 μm off the divertor plate. Therefore, regular giant ELMs reduce target lifetime regardless of design and materials choice. The number of ELMs that occur in a plasma are dependent on the elongation of the plasma. The more elongated the plasma, the fewer the ELMs. At this time, the elongation, κ, of ITER is 1.6.

The erosion of the dump targets is a serious issue. The dump targets are bombarded by mainly plasma ions. The temperature in front of the target may be sufficiently low to avoid physical sputtering for some materials. Chemical sputtering is a serious concern for carbon; however, redeposition does help to control erosion if redeposition occurs on the same location which is not necessarily assured.

The material is both vaporized and ablated away due to the temperature reached and the incident particles. However, there is an accompanying phenomenon which arises from large plasma dumps onto the material surface. This protective effect is known as plasma (or vapor) shielding. There has been much investigation, through both experiments and modeling, into this area; results are summarized in section 2.5.

2.5 Plasma Shielding

Plasma shielding can be described as follows. At the onset of a disruption, hot plasma electrons and ions strike the divertor surface. This is accompanied by a large rise in divertor temperature, thus the surface of the divertor starts to thermally ablate, or vaporize. This cloud of material rapidly expands in the direction of the incoming plasma particles. Also this cloud, which has a finite density, begins to attenuate incoming particles. The kinetic energy of some of these incoming electrons and ions is transferred to the cloud, thus ionizing the atoms. However, the majority of the energy is still dumped into the solid material behind the vapor. More vapor is generated since the material is still being heated. Since the shield is ionized the expansion is affected by the presence of a magnetic field. At the front of the divertor the magnetic field is approximately parallel to the surface, hence the outward expansion of the cloud is hindered and the density begins to climb. As the cloud is ionized, radiation is emitted isotropically. Thus, the surface of the divertor continues to be heated but at a reduced rate. However a point is eventually reached where the density is such that most of the radiation that is created in the cloud is reabsorbed before reaching the material surface. A protective plasma shield is now formed which absorbs all incoming energy, and thus extends the life of the divertor. This protective shield can be formed in microseconds. Figure 2.4 shows schematically all the processes that occur to create plasma shielding during a disruption.

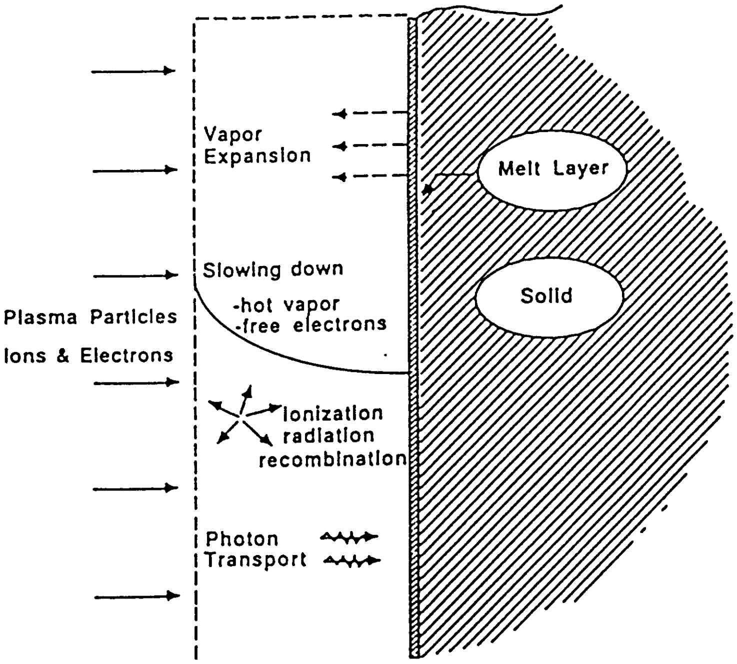

Figure 2.4 Processes that occur during plasma shielding during a disruption. [6]

Many experiments have been conducted, and many numerical models have been created to describe the phenomenon. In 1994, three research groups collaborated on a extensive project to model as accurately as possible the effects of a disruption on the erosion of a carbon divertor. The IPP, KfK and the ENEA [7-9] collaborated on an extensive study of the effect of plasma shielding and the lifetime of the divertor. This study avoided many of the compromising simplifications that other studies such as that done by Höbel et al[10] incorporated. For example in Höbel's work the model used made the following assumptions and restrictions: the model was 1D, aluminum was the material used, the impinging beam was comprised only of protons, the proton beam was incident perpendicularly, no magnetic forces were accounted for, the divertor was simulated as a solid plasma, and finally, no melt front was incorporated into the model. In the simulation by the joint collaboration, many of these restrictions were eliminated. The model took account of the fact that there was a magnetic field present, the particles (both ions and electrons) are incident at a 2° angle, the materials used was carbon so it was not necessary to account for a melt layer (carbon only sublimates, it does not melt). From their model, they calculated, including chemical sputtering effects, the amount of material lost per disruption. The results of their study will be examined in Chapter 3.

2.6 ITER Divertor Design - Engineering Concept

The TAC-4 divertor design has taken into account space constraints, neutron shielding requirements and remote handling compatibility. Additional problems that the divertor is expected to handle are excessive heat loads especially on the target plates during giant ELMs and disruptions. It must also be able to withstand a large steady state heat load onto the divertor baffle, the divertor structure and the energy dump targets. The engineering design can be seen in Figures 2.5 - 2.7. The physics requirements discussed above have led to this conceptual engineering design.[1] A design that consists of 96 removable cassettes is shown in Figure 2.6. The engineering design concept can be divided into 4 major areas: the divertor baffle/toroidal limiter, the divertor dome, the power exhaust/momentum loss region, and the energy dump targets. The area of interest in this study is the dome and energy dump targets. (Figure 2.2)

In the design of the divertor, the main idea is to have large recycling of a neutral gas in the divertor region that will intercept the incoming power - the dynamic divertor concept. The TAC-4 design incorporates this through a slotted divertor design. The interaction between the plasma and the neutrals causes the charged particle power to be extinguished by radiative and charge-exchange processes before reaching the back plate of the divertor.[11] Therefore, the scrape-off layer (SOL) power is expected to be spread over a much larger area resulting in a lower peak steady state heat load of 5 MW/m^2.

The energy dump targets are designed both to receive a steady state power load of <10% of the 240 MW conducted into the SOL (assuming that 90% is lost by radiation and neutral collisions) and to absorb heat pulses from edge localized modes (ELMs) and disruptions.[12] The peak heat flux on the energy dump target is approximately 2 MW/m^2. Under a disruption or a giant ELM the heat load is much higher. The value of the heat load is dependent not only on the energy deposited (<1.5 GJ), but more importantly, on the time duration of the pulse. At times greater than several μs, the evaporated materials will form a dense, expanding vapor shield in front of the dump targets.[12] The armor/energy dump targets should of a thickness such as to maximize their lifetime while allowing a steady state heat removal of 5 MW/m^2. In this design described in [12]the energy dump plates are a castellated (6 to 8 mm squares) 10 mm thick Be, W or 40 mm thick for C cladding bonded to Cu hypervapotrons. (Figure 2.7) Some of these hypervapotrons are machined from a Cu-SS sandwich plate forming a water cooled target ~ 300 mm wide by ~ 600 mm long. Four of these target plates are mounted onto the cassettes (two by two poloidally and toroidally) to form a V-shaped energy dump target. (Figure 2.5) A similar concept is followed for the dome. The dump target plates should be aligned to a precision to better than 2 mm to reduce shadowing.[12] The general materials qualities which are important for the armor material are high thermal conductivity, low erosion rate, low atomic number, and good mechanical properties such as high elastic modulus.

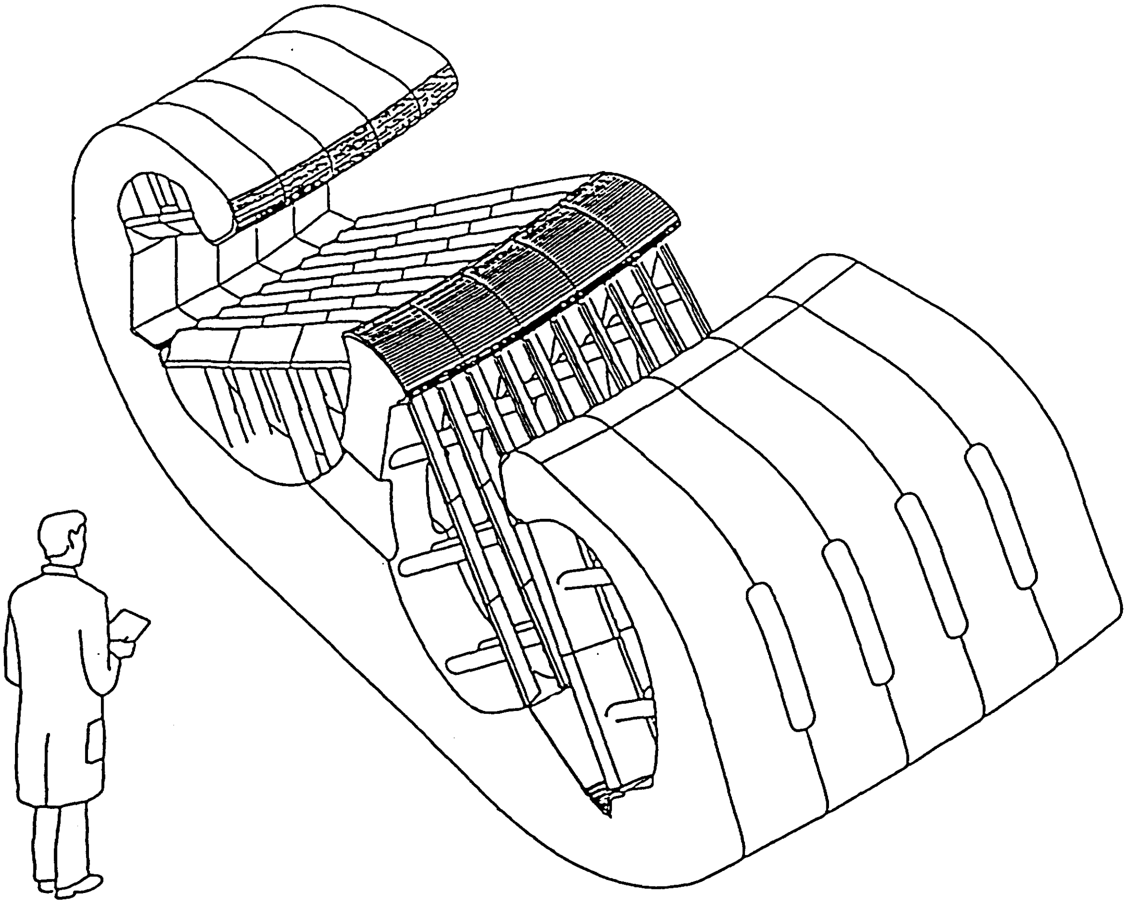

Figure 2.5 : Isometric view of the divertor cassettes. [1] Note the scale of the component.

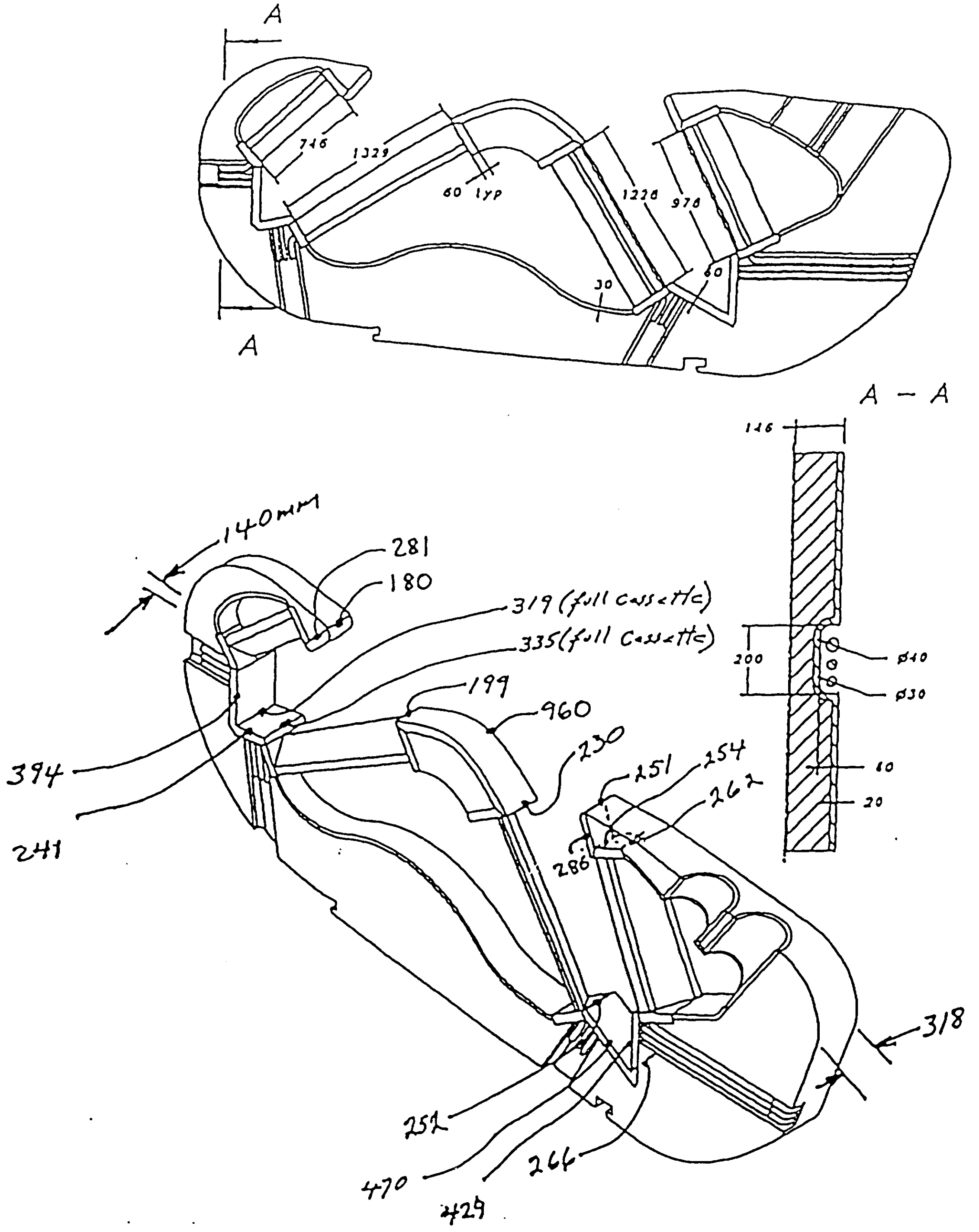

Figure 2.6: Dimension of the half divertor cassette. Width dimensions (in millimeters) are for the half cassette unless otherwise noted.[13]

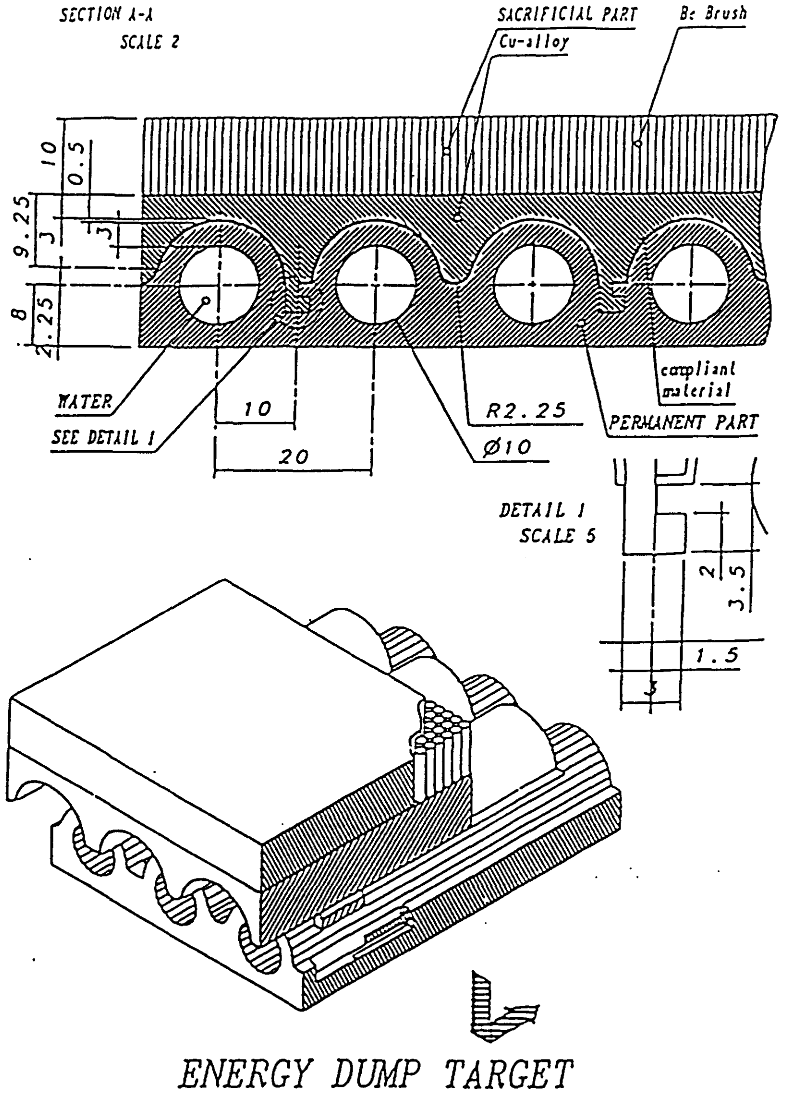

Figure 2.7: Diagram of the energy dump target. All dimensions are in millimeters.[1]

2.7 Component Lifetime

Since one of the main purposes of the divertor is to intercept the plasma, the erosion of the dump target due to the incident plasma is of great concern. In a dynamic gas target with typical ITER upstream parameters the ion flux onto the target will be ~ 10^{23} ions/m^2s [12]and the plasma temperature will be less than 5 eV. Therefore, under steady state operation, there should be little erosion. However, small ELMs can burn through the gas cushion. When the curtain is passed through, the ion flux on the dump targets will exceed ~10^{24}ions/m^2s and the leading edge temperature should be > 20 eV. If the plasma remains attached during ELMs for 10% of the discharge, the average power loading would be 20 MW/m^2.[12] The lifetime of the dump targets is also determined by the number of disruptions and giant ELMs and the energy that they deposit. A comparison of the three materials and how they are affected by these conditions will be discussed in Chapter 3.

2.8 Summary

In order for ITER divertor target plates to have an acceptable heat load of less than 5 MW/m^2, it is necessary to investigate solutions such as the dynamic gas target divertor. Experiments are underway at ASDEX, DIII-D and Alcator C-Mod to measure the effects of neutral gas puffing in front of the divertor target plates. Experiments have shown promising results with the impurity gases neon and argon. Therefore, the divertor design for ITER is a slotted design to promote circulation in the divertor region. The components of the divertor which are of interest to this study are the dump target and the dome. The object of this study is to determine the performance of the C, Be and W armor.

CHAPTER 3

The woods are lovely, dark and deep,
But I have promises to keep,
And miles to go before I sleep,
And miles to go before I sleep.
Robert Frost

Materials Issues for the ITER Divertor

Materials used in a divertor are in a unique environment. The materials are subjected to high energy neutron radiation, high particle flux, and cyclic strains. In this chapter each of the phenomena will be discussed and they affect a material. The first topic to be discussed is the general mechanical and thermophysical properties of each of the potential armor materials. Appendix B contains the materials data supplied by the manufacturers of the candidate materials.

3.1 General Properties of Beryllium, Tungsten and Carbon

3.1.1 Beryllium

Beryllium is considered as a candidate armor material because of some of its materials properties. Qualities of Be that can be considered advantageous are: low weight, a high stiffness, and specific mechanical properties such as an precise elastic limit. Beryllium also has a high melting point, the highest specific heat among metals, and a high melt viscosity. It has a hexagonal close packed crystal structure. Through powder processing it can achieve a fine grain size (1 to 10 μm). Using HIPping[2] densities of 99.5% of the theoretical can be achieved. Another important characteristic is that pure Be can be easily joined to copper by brazing. This ability to be brazed is crucial to the heat transfer properties for the divertor. It can also be plasma-sprayed; this is important for in-situ repairs. Beryllium can be machined to extremely close tolerances - and it has excellent dimensional stability. Beryllium is usually produced through powder metallurgy (P/M). The reference material selected for this study is S-65 manufactured by Brush Wellman.[14]

---

[2] HIPping: Hot Isostatic Pressing

The operating temperature of beryllium is between 200°C and 600°C [1] due to a ductility requirement. Under neutron irradiation, beryllium is degraded through displacement damage and transmutation. The displacement damage leads to point defects, irradiation hardening and embrittlement. Transmutation leads to the production of helium in the beryllium which causes the material to swell, lose thermal conductivity and become embrittled. In Table 3.1, general unirradiated properties of S-65 grade beryllium are listed.

Table 3.1: Properties of S-65 Beryllium

Elastic Modulus (E)	303 GPa [15]
Density (ρ)	$1.85\ kg/m^3$ [15]
Thermal Conductivity (k)	210 W/mK [15]
Thermal Expansion Coefficient (α)	$11.5 \times 10^{-6}/K$ [15]
Specific Heat (300K) (C_p)	2.17 kJ/kgK [15]
Melting Point	1283°C [15]
Ultimate Tensile Stress	290 MPa [14]
Yield Stress	207 MPa [14]
% Elongation (% in 4 diameters)	3.0 [14]
Boiling Point	2970 °C [16]

3.1.2 Tungsten

Advantages to using tungsten are that it has a very high melting point, a high elastic modulus, a high tensile strength and good creep resistance. However, disadvantages to using tungsten are its high density, high atomic number, poor low-temperature ductility and strong reactivity in air. Tungsten also has a body centered cubic (BCC) crystal structure so there are few slip planes and a propensity for brittle fracture. Tungsten forms can be produced through cold pressing and sintering. Hot pressing can also be used but these components are usually more brittle and lower in strength. Also a carburized layer may form on the surface of the blank that is difficult to remove in machining. Tungsten begins to oxidize readily at 500°C; at 1000°C tungsten reacts with many gases, including water vapor and carbon monoxide. The ductile to brittle temperature transition (DBTT) is above 205°C which is a serious problem for ITER working conditions. Only by heavy or warm cold working is the DBTT lowered to below room temperature. However, annealing (such as caused by high temperatures possibly reached during transients) raises the DBTT again. The DBTT is influenced by grain size, strain rate, and impurity levels. To clarify, DBTT decreases with grain size, drops with increases in strain rate, but climbs rapidly as impurity levels increase. This increase in the DBTT with increased impurity levels can be a problem due to transmutation in the tungsten. Through doping with rhenium, it is possible to decrease the DBTT. W-Rh alloys are under consideration for ITER armor, but this study will focus on pure tungsten. The reference material is pure tungsten plate, Climax WP-1, produced by Climax Specialty Metals. [17] Important characteristics of tungsten are listed in Table 3.2.

Table 3.2: Properties of Tungsten [18]

Melting Point	3410°C ±20°C
Thermal Expansion (25°C to 2500°C) T in Celsius	$\frac{L-L_{25^\circ C}}{L_{25^\circ C}} \times 100 = -4.58\times10^{-3} + 3.65\times10^{-4}T + 9.81\times10^{-8}T^2$ (powder metallurgy sheet)
Specific Heat (0 to 3000°C) T in Kelvin C_p in J/kgK	$C_p = 135.76(1-\frac{4805}{T^2} + 9.1159\times10^{-3}T + 2.3134\times10^{-9}T^3)$
Enthalpy (935°C to 2975°C) T in Kelvin H in J/kg (Derived from C_p)	$H_T - H_{298} = 135.76(T + \frac{26.14}{T}) - 4.266\times10^3 + 4.5569\times10^{-3}T^2 + 5.78205\times10^{-10}T^4$
Latent Heat of Fusion	220±36kJ/kg
Latent Heat of Sublimation	4680 ±25 kJ/kg
Vickers Hardness at 1000°C (annealed)	75 HV
DBTT when annealed 1000°C	100°C
Tensile Stress at 1000°C	225 MPa
Percent Elongation at 1000°C	55%
Thermal Conductivity at 1000°C	125 W/mK
Stable Isotopes in atomic percent	0.14% W-180, 26.41% W-182, 14.40% W-184, 30.64% W-186

3.1.3 Carbon

The third option for armor material is to use a ceramic instead of a metal. Due to its availability, extensive use in fission environments, and low Z, carbon is being considered. The differences between the metals and the ceramic must be examined on a molecular scale. While beryllium and tungsten consist of metallic bonds - which influence the thermophysical and mechanical properties of these metals, carbon has a more complicated molecular structure.

A single crystal of graphite has a layered structure of parallel sheets of carbon that are covalently bonded in hexagonal arrays. Since the bonds in sheets are covalent and the bonds between sheets are π bonds, the materials properties are highly anisotropic. Pyrolytic carbon is of primary interest for use in a fusion reactor. Pyrolytic graphite is produced by decomposing a gaseous hydrocarbon at the near surface of a substrate in order to produce a carbonaceous deposit. This deposit can be relatively isotropic by careful production. The type of carbon selected for this study is IG-11 grade produced by Toyo Tanso. [19] The type of graphite is a high density, fine grain, isotroopic grade. A summary of IG-11 properties can be found in Table 3.3.

Table 3.3: Properties of IG-11 Graphite[19]

Elastic Modulus	9.8 GPa
Density	1.77 kg/m^3
Thermal Conductivity	116 W/m-K
Flexural Strength	39.2 MPa
Compressive Strength	78.5 MPa
Tensile Strength	24.5 MPa
Coefficient of Thermal Expansion (350-450°C)	$4.5 \times 10^{-6}/K$
Porosity	15%

3.2 Radiation Damage in Materials

The armor material for the divertor operates in a strong radiation environment. The armor is exposed to high energy neutrons, ions and electrons - all of which can lead to material property changes. Radiation has been shown to change structural and mechanical properties, electronic and physical properties and thermal and rate processes. This work will concentrate only on the structural/mechanical and the thermal changes. Some general changes in the former are: crystal structure defects, density decreases, hardness increases, yield strength increases, the ultimate tensile strength increases and the ductile to brittle transition temperature increases. The thermal changes include: a decrease in the thermal conductivity, increase in diffusion, impurity concentration increases and nuclear transmutations.[20]

Radiation causes changes in the materials properties due to the introduction of defects. These defects are point, line or plane dislocations which are generated through collisions of the lattice atoms with high energy incoming particles. The theory can be explained as follows. A high energy particle strikes a solid surface. The atom that is struck is known as the primary knock-on atom, or PKA. The PKA dissipates its energy either through electronic excitation or through nearly elastic collisions with other atoms in the target. If the PKA has an energy greater than the displacement energy and it can go on to strike other atoms and displace them from their equilibrium positions. When the incident particle has an energy much greater than the displacement energy - a cascade effect can result. (Figure 3.1) This branching tree-like structure of collisions causes the PKA to lose its energy in ~ 100 fs which produces a number of atoms moving with near thermal velocities, and also some electronic excitation.[21] In metals, this electronic excitation will lead only to heating. Since most of the atoms are not displaced a large distance from their equilibrium position, many if not most return to their equilibrium positions and only a finite number of defects remain. Those defects which remain recombine or agglomerate into clusters over a time interval that depends on the defect concentrations and on the target temperature. [21]

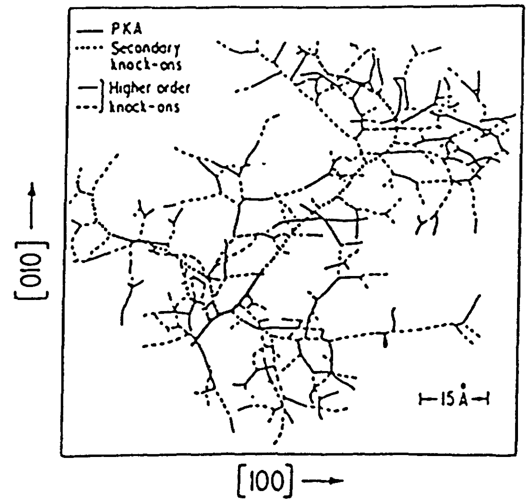

FIG. 6. Proposed structure of displacement cascade caused by a 5 keV PKA in iron. Out-of-plane damage has been projected onto the (001) plane shown in the figure. (After Beeler, 1966.)

Figure 3.1 Branching dislocations produced by PKA.[22]

Typical time scales for the rearrangement are from ~ 1 ps to 1 s or more and this produces the microstructure responsible for the macroscopic effects of radiation. [21] Phase changes can also occur from transmutation of atoms in the lattice. Specifically, the appearance of He in the lattice from (n, α) reactions is of particular concern because the helium stabilizes voids and leads to swelling of the material.

In addition to producing structural changes in material, irradiation can also lead to a change in the composition of the materials - either by ion implantation or by transmutation.[21] Enhanced diffusion can also lead to changes in the material composition. Radiation damaged materials also may store energy. One example of a the effect of the release of the energy stored can be seen by examining the accident at Windscale. In the 1950's it became the practice to anneal some graphite containing reactors in a controlled manner to release the energy stored in graphite due to neutron irradiation. This was done to avoid an unexpected catastrophic release. However, on October 10, 1957, at Windscale in northwest England control was lost of the annealing process and the reactor seriously overheated. The result was a large release of radioactive fission products over a wide area, including the Irish Sea. Therefore, radiation damage plays a role in the safety of reactors - both fission and fusion.

One difficulty in determining how a material will be affected by operation of a fusion reactor is that no testing facility exists for fusion materials. That is, there exists no large volume source of 14.1 MeV neutrons. Most irradiation data are from fission reactors which have different particle energies and fluences than those expected in a fusion reactor. Therefore, in order to determine how to correlate fission data to a relevant fusion regime, methods of extrapolation must be determined. For this study, it was decided to normalize all data to displacements per atom (dpa). This method is explained below.

Under neutron irradiation the figure of merit is the total number of displaced atoms per unit volume. This calculation can be described as follows.[20] The average number of displaced atoms per incoming particle, $\overline{\upsilon}_d$, can be calculated by the following formula.

$$\overline{\upsilon}_d \cong \frac{E_{av}}{2E_d} = \frac{MM_oE}{(M+M_o)^2 E_d} \tag{3-1}$$

M is the mass number of the incoming particle, M_o is the mass number of the target, E is the energy of the incoming particle, and E_d is the displacement energy of the lattice atom which is approximately 25 eV. For general understanding of the trends for our candidate materials, we can calculate the average number of displaced neutrons generated from a 14.1 MeV neutron. Using formula (3-1) the results are shown in Table 3.4.

Table 3.4: The averaged number of displaced atoms $\overline{\upsilon}_d$, over , primary knock-on, E=14.1 MeV.

Element	Be	C	W
M_o (mass number)	9	12	184
$\overline{\upsilon}_d$	50,760	40,047	3,032

It can clearly be seen from the results in Table 3.4, that beryllium and carbon will be more affected by radiation displacement damage than tungsten. Clearly, the more massive an atom, the harder it is for a neutron to displace it.

The displacement cross section, σ_d, is defined by the following equation [20]:

$$\overline{\sigma}_d = \frac{16\pi a^2 Z^2 Z_o^2 M^2}{(M+M_o)^2 E_m^2} E_r\left(\frac{E_m}{E_d} - 1\right) \tag{3-2}$$

where E_r is the Rydberg energy, E_m is the maximum energy transferred to the nucleus, M_o, in a head-on collision, a is the Bohr radius of the hydrogen atom, Z is the atomic number of the incoming particle and Z_0 is the atomic number of the target. In order to obtain the quantity of interest, dpa, the following equations from[3] can be used.

$$dpa = \Phi \int_{E_d}^{\Lambda E_i} \sigma_d(E_i, E)\upsilon(E)dE \tag{3-3}$$

with

$$\Lambda = \frac{4A}{(1+A)^2} \tag{3-4}$$

where Φ is the neutron flux, σ_d is the displacement cross section,υ is the number of displaced atoms for each collision that produces a PKA of energy E, and Λ is the energy transfer parameter with A being the atomic mass on the lattice atom. This is actually a very difficult calculation, so in this work the dpa's will be determined using cross sections from the ENDF/B-V data. The calculation of the dpa's gives an indication of the radiation damage to the material as the irradiation time increases. These displaced atoms change many of the fundamental characteristics of a material through changes on the atomic level. Table 3.5 lists some of the changes that may occur due to irradiation.

Table 3.5: Basic Radiation Effects on Changes in Nuclear Materials Properties
(Based on Table 4.7 Ma)[20]

Structural and Mechanical	Thermal and Rate Processes
Crystal structure defects	Thermal conductivity decreases
Density changes	Particle diffusion increases
Ductility decreases	Nuclear transmutation occurs
Hardness increases	Phase change shifts
Yield strength increases	Impurity increases
Ultimate strength increases	Chemical reactions affected
Elastic constants increase	
Ductile-brittle transition temperature increases	

3.3 Microstructural Changes in Material under Irradiation

3.3.1 Voids

When a material is irradiated by high energy neutrons, the characteristic defect that is generated in the material is a Frenkel defect, i.e. a vacancy interstitial pair. Also, the incoming neutron can generate a displacement cascade which is rich in vacancies. The interstitials that are generated through irradiation are transported away through athermal processes along close packed directions.[23] The remaining vacancies can form dislocation loops or aggregate to form voids. These voids can increase the volume of the material by several

---

[3] Olander, Donald R., *Fundamental Aspects of Nuclear Reactor Fuel Elements*, Technical Information Center, 1976.

percent. Voids appear in an irradiated material if it is held at temperatures 1/3 to 1/2 the melting point. At temperatures lower than 1/3 the melting point, the vacancies are rapidly annihilated by diffusing interstitials. At temperatures greater than 1/2 the melting point, the thermal equilibrium concentration of vacancies is approximately equal to the irradiated concentration of vacancies; therefore, the voids shrink. If helium is formed in the material it can stabilize the voids.

3.3.2 Bubbles

In a fusion reactor, there are also high energy hydrogen, deuterium and helium ions implanted into the surface of the first wall. Also, helium and hydrogen are generated in the material through transmutation. Since gases have a limited solubility, they tend to precipitate out and form bubbles. The ions implanted on the surface of the material will also precipitate out and form blisters on the surface of the material. Not only do blisters and bubbles alter the properties of a material, but the blisters can burst send in a puff of gas that will contaminate the plasma.

3.4 Mechanical Properties

3.4.1 Tensile

Theory suggests that strain-hardening and irradiation-hardening share a common mechanism. Based on a discussion in Gittus [23], if the distribution of dislocations and their signs are random in a lattice, then the external stress which one dislocation feels based on a sum of the forces on it by neighboring dislocations is:

$$\frac{Gb}{2\pi r} = \sigma \tag{3-5}$$

where G is the shear modulus, b is the value of the Burgers vector and r the distance between neighboring dislocations. Since,

$$r = \rho^{-0.5} \tag{3-6}$$

where ρ is the dislocation density (dimensions L^{-2}). Under strain, a source (such as the Frank-Read source) generate new dislocations which move a distance L, before being frozen in the lattice. Therefore,

$$d\varepsilon = d\rho \cdot bL \tag{3-7}$$

where dε is the plastic strain increment due to the glide, through a distance L, of the new dislocation, dρ. Combine these three equations and integrate:

$$\sigma = \frac{Gb}{2\pi}\sqrt{\frac{2\varepsilon}{bL}} \tag{3-8}$$

Since, neutron dose leads to dislocations, the argument above can be used to explain irradiation hardening as well as strain hardening.[23]

3.4.2 Yield Stress

Neutron irradiation also has a profound effect on the yield stress of materials. Through the introduction of defects, the yield stress increases and the ultimate tensile stress also increases, i.e. the material is hardened. However, the strain until failure is greatly decreased, therefore, the toughness (the energy absorbed in fracture) is decreased. In general, it can be said that the mechanical strength of a material is increased under irradiation, but the ductility is lost; therefore, the material in embrittled.

3.5 Sputtering

Sputtering is defined as the removal of surface atoms from a solid due to atoms or ions impinging on the surface. Sputtering leads to two major problems in tokamak design. First, sputtered atoms are impurities in the plasma which, depending on their Z_{eff}, can radiate away large amounts of power thus making plasma ignition very difficult. Also, sputtering leads to the erosion of plasma facing components, thus diminishing their useful lifetime in the tokamak.

In the divertor region, high energy ions and neutral atoms impinge on the surface of the dome and the dump targets.(Figure 2.2) If this incident particle transfers enough energy such that the surface atom receives energy in excess of its binding energy, the atom will be removed from the lattice.

There exists a threshold energy, E_T, of the incident particle below which sputtering will not occur [24] The theoretical value is:

$$E_T = \frac{E_s}{\gamma_{sp}(1-\gamma_{sp})} \tag{3-9}$$

where E_s is the sublimation energy of the solid, and $\gamma_{sp}= 4m_1m_2/(m_1+m_2)^2$, where m_1 and m_2 are the masses of the incident and target atoms.

One major ITER task was to determine the sputtering of the armor materials in the divertor location. [7-9] The results can be summarized as follows. The power load was assumed to be 5 MW/m^2 for 90% of the time and 20 MW/m^2 for 10% of the time. The incident ions are D, T and He (20%). Assuming that the temperature is ~10 eV (lowest temperature used), the lifetime in number of pulses for a 10 mm armor of Be is ~ 5000 and for a 10 mm armor of C is ~ 15000. The W armor had no sputtering limit.

Another study conducted by a NET team[25] calculated the sputtering rates due to low energy particles, which are of interest in a dissipative gas divertor. For a plasma temperature of 5eV, the erosion of carbon, not including chemical sputtering, was found to be ~ 10 to 100 less than that of beryllium. With chemical sputtering[4] accounted for, the carbon erosion is approximately the same as the beryllium erosion. The sputtering rate of carbon (not including chemical sputtering) was determined to be 1.97×10^{-7}mm/s. The chemical sputtering of carbon and sputtering of beryllium was found to be ~ 6.1×10^{-6} mm/s. The sputtering rate of tungsten was determined to be 2.84×10^{-18} mm/s. These rates are very comparable to those mentioned previously.

3.6 Effect of Neutron Irradiation on Each Candidate Material

3.6.1 Beryllium

The most important effects of neutron irradiation on beryllium are swelling, embrittlement and tritium retention. [26] Under neutron irradiation, beryllium undergoes the following transmutation reaction:

$$^{9}Be + n \rightarrow 2\,^{4}He + 2n \tag{3-10}$$

This reaction has a neutron energy threshold of 1.7 MeV.[24] As discussed earlier in this chapter, production of helium leads to swelling of the material. The amount of helium produced can be directly correlated to the swelling produced in the material. A comprehensive study [27] has led to two equations that relate the helium content to the swelling percentage.

$$(\Delta V/V_o) \times 100 = (1.19 \pm 0.07) \times 10^{-4}\, C_{He} + (1.20 \pm 0.03) \times 10^{-19}\, C_{He}{}^{2} T^{4} \tag{3-11}$$

$$(\Delta V/V_o) \times 100 = (1.19 \pm 0.07) \times 10^{-4}\, C_{He} + (1.56 \pm 0.04) \times 10^{-19}\, C_{He}{}^{2} T^{4} \tag{3-12}$$

---

[4] Chemical sputtering is the removal of surface atoms through a chemical reaction e.g. formation of CH_2.

The first and second equation correspond to 1h and 24h annealing periods. $\Delta V/V_0 x100$ is the percentage swelling, C_{He} is the concentration of helium and T is the temperature in degrees Celsius. The concentration of helium can be linearly related to the fast neutron fluence, Φ, by $C_{He} = (4880 \pm 90) \times 10^{-22} \Phi$ [27]

The best reference for the changes in the mechanical properties of beryllium under neutron irradiation is a review paper by Gelles et al. [28] In this paper, the authors summarize most of the experimental results of neutron irradiation effects on beryllium. In general, the response of the material is highly dependent on the irradiation temperature. For example, at low temperatures, the strength increases due to irradiation. At higher temperatures (~ 650°C), irradiation embrittlement can increase, without a corresponding significant strength increase.[28] Under low temperature irradiation, when the yield strength is plotted versus the fluence, a bell shaped curve is seen.[28] The increase in hardness of beryllium at low temperatures is linear with fluence. At higher temperatures, 280 - 650°C, the trend is also approximately linear, except that the increase in hardening is not as high. The yield strength also depends on fluence; however, the dependence seems to be proportional to fluence to the 1/3 power. With the increase in the strength, the ductility decreases and embrittlement occurs. For example, for nuclear grade hot-pressed beryllium irradiated to fluences of 3.5×10^{21} to 5.0×10^{21} n/cm^2 (E>1 MeV) at 66°C, the unirradiated fracture toughness of 12 MPa $m^{1/2}$ was reduced by 60%.

Microstructural investigations of irradiated beryllium have given insight into the strong temperature dependence of materials properties changes. At low temperatures (<400°C), the damage consists of loop damage. At higher temperatures, helium bubbles are the main characteristic. At temperatures 325-400°C, helium bubbles are present on the grain boundaries and at 450-500°C helium is also present on dislocations. At an irradiation temperature above 600°C, the bubbles are mainly restricted to grain boundaries.

Two characteristics can be modified to optimize beryllium performance — purity and grain size. Swelling decreases with decreasing oxygen content and increasing grain size. In order to minimize swelling at high temperatures, the choice would be to adopt extruded grades with the oxygen level on the order of 3% and grain diameters ~ 10 to 20 µm. Also, for operation at low temperatures, modern fine-grained materials are more resistant to swelling than older grades.

In summary, most existing data is for older grades of beryllium. Also, since all the data are generated from a fission spectrum, they are not exactly relevant. Since the production of helium has a high (1.7 MeV) threshold, the helium production should be underestimated in a fission spectrum. It is necessary for more tests to be done on modern grades of beryllium. Irradiation tests have been conducted of S-200E grade beryllium (which is similar to S-65) at EBR-II in Idaho and FFTF in Hanford, WA; however, "in each case, the capsules have been removed from the reactor..., but there has been no funding available to remove the samples from the canisters." [29] Hopefully, money will become available to test these samples for they would provide invaluable data from the performance of beryllium.

Under neutron irradiation, beryllium can undergo many transmutation reactions, for example helium production as shown earlier. However, all the reactions may not be as radiologically benign as this reaction. Depending on the neutron energy spectrum , many other reactions can also be undergone. While S-65 grade beryllium is highly purified, it still contains minute amounts of other elements.(See Appendix B) It is very possible that transmutation products from the beryllium or the impurities can lead to high levels of activity. This activation will be investigated in Chapter 5.

3.6.2 Carbon

The most important effects of neutron irradiation on carbon are large dimensional changes, helium production, tritium retention, degraded material properties and degraded thermophysical properties. As previously mentioned, the grade of carbon that was selected for this study is Toyo Tanso IG-11. The primary reason for this selection is that there exists a large data base [30] on radiation damage to this material since it is used in the JAERI HTGR (Japanese Atomic Energy Research Institute High Temperature Gas Cooled Reactor). Therefore, no extrapolation has to be done from data collected on other grades of graphite which is very valuable considering the extremely wide variation in properties and radiation response of graphites. The report in which the IG-11 data is tabulated [30] studied the response of graphite to a neutron fluence. The irradiations were made to a maximum of about 2.5 x 10^{21} n/cm^2 (EDN) at temperatures from 1050°C to 1150°C. The properties studied of interest to this work were: dimensional change, Young's modulus, open porosity, thermal conductivity, and ring compressive strength.

Carbon also reacts with a neutron to produce helium as follows:

$$^{12}C + n \rightarrow n' + 3\,^{4}He \tag{3-13}$$

This reaction has a neutron energy threshold of about 10 MeV.[31] Since the threshold energy is so high, helium production should not be a severe problem in graphite because high energy neutrons rapidly lose energy in graphite. However, one issue is that carbon co-deposits with tritium. This can cause several problems. First, this chemical binding provides a sink for the tritium fuel. Second, this makes the divertor much more radioactive when it is removed from the reactor for maintenance.

As discussed for beryllium, IG-11 graphite also undergoes nuclear transmutation that generates radioactive products. Also, while it is highly purified, it does contain trace amounts of other elements.(Appendix B) Therefore, activation is of concern.

3.6.3 Tungsten

The primary concern in using tungsten as an armor material for the divertor is the fact that it has a BCC crystal structure and its mechanical properties can be greatly affected by neutron irradiation. Under the auspices of ITER R&D a Russian team studied the effects of neutron irradiation on several refractory materials, including tungsten.[32] The irradiation was performed in the SM-2 reactor to doses of $1\text{x}10^{21}$ n/cm^2 and $5\text{x}10^{21}$ n/cm^2 at T_{irr} ~ 100°C and ~ 300-500°C and also in the BOR-60 reactor to doses of $8\text{x}10^{21}$ n/cm^2, $1.6\text{x}10^{21}$ n/cm^2 and $2\text{x}10^{22}$ n/cm^2 at T_{irr} ~ 350, 500 and 800°C. Results on two samples in this study are relevant to this thesis work - a deformed sample of tungsten and a sample of tungsten annealed at 1200°C for 1 hour. When these sample were irradiated to a dose of ~ 1 dpa at 330-370°C, the following changes occurred in their properties. In the deformed specimen, the yield strength decreased from an unirradiated value of 800 MPa to a value of 100 MPa. The total elongation in this sample changed from an unirradiated elongation of ~2% to 0% (brittle fracture). In the annealed sample, the yield strength decreased from an unirradiated value of 760 MPa to a value of 500 MPa. The total elongation of the sample decreased from 8% to 0% (brittle fracture). No information could be found from any source on the shift of the DBTT due to irradiation.

As discussed earlier, the DBTT of tungsten depends on the purity of the material. Under neutron radiation, tungsten readily transmutes to other elements. Also, although this grade is highly purified, it still contains measurable amounts of approximately 15 other elements - all of which transmute under neutron irradation. Therefore, it is to be expected that the DBTT will shift to higher temperatures under neutron irradiation due to the presence of impurities. While the shift in DBTT from transmutation is an area of concern, another area is the increase in activity. This area will be investigated in Chapter 5.

3.7 Summary

From the discussion in this chapter it is clear that each candidate material is affected by the operating environment; however, each material is affected in a unique manner. Beryllium can have severe void swelling due to helium production from transmutation reactions. This void swelling may lead to thermal stresses and decreased density. The decreased density will cause the heat transfer capability of the beryllium to be diminished. Carbon also has its unique response to this environment. Of primary concern is the drastic loss in thermal conductivity due to neutron irradiation. Carbon will also sputter easily - which will cause a rapid diminution in the armor thickness; hence, a decreased lifetime. Also, another area of concern is the fact that carbon co-deposits with tritium. Carbon that has been aputtered off the surface can react with tritium and re-deposit on the surface of the targets and dome. This reaction causes a sink for the tritium fuel as well as a safety hazard since inventories can build up to dangerous levels in the armor. Tungsten has a very different area for concern. Under neutron irradiation the DBTT will shift to higher temperatures. This increased brittle regime would diminish the structural properties of the tungsten. While the increase in impurities will lead to an increased DBTT, it will also be a problem for activation. Tungsten is a heavy metal and its transmutation products can be quite active. This topic is investigated more in Chapter 5. In Table 3.6, the relevant areas of concern for each of the candidate armor materials is summarized.

Table 3.6 Primary Issues for Candidate Materials

Beryllium	Tungsten	Carbon
Void Swelling from He production	DBTT increase	Decrease in thermal conductivity
Thermal Stresses	Activation	Sputtering yield
		Tritium co-deposition

CHAPTER 4

"You can't always get what you want,
but if you try sometimes
you just might find
you get what you need"
Rolling Stones

Radiation Damage of the ITER Divertor

4.1 Displacement Damage in the Armor Material

As discussed in Chapter 3, a method for quantifying the amount of damage produced in a material by particle irradiation is to determine the displacements per atom (dpa) that are created. Once the number of dpa's is known, prediction as to how the material properties will change under this irradiation can be made. The neutron damage in displacements per atom (dpa) for the dome and dump targets in the ITER divertor region has been determined using the Monte Carlo N-Particle Transport Code System MCNP4A.[33] The platform used for this study was a Silicon Graphics IRIS Indigo workstation. Two operational modes, deuterium-deuterium (DD) plasma and deuterium-tritium (DT) plasma have been studied. While ITER is not designed to run with DD fuel in that it is not the correct geometry for ignition, it was decided to investigate the effects DD operation in a similar reactor would have upon materials. All results are scaled for the Basic Performance Phase (BPP) operation (1.5 GW).

The basic input file for the TAC-4 geometry was supplied by M.E. Sawan [34] and modified for this study. One of the input files (beryllium armor under DT operation) can be found in Appendix A. Two input files were generated for each of the three candidate armor materials—one for DD operation and the other for DT operation. A vertical cross section of the model is shown in Appendix A, Figure A.3. The input file supplied was designed to model half a toroidal field coil, it was modified to model half a divertor cassette instead. In the TAC-4 design, there are 96 cassettes, therefore, a half cassette corresponds to a section of 1.875°. Reflective boundary conditions are used on either side of the half cassette so that the 1.875° section models the entire reactor.

For the DD model, a neutron source of a flat energy spectrum of 100% 2.4 - 2.5 MeV was used. For the DT model, source neutrons of a flat energy spectrum of 99% 13.8 - 14.1 MeV and 1% 2.4-2.5 MeV was used. An isotropic toroidal source of 1 meter in diameter is located at the magnetic axis which is located at a radius of 8.633 m and is 1.622 m above the reactor midplane.[34]

Source particles travel through the plasma void until they strike the first wall of the reactor. (Figure A.3) As can be seen from the geometry, the dome directly faces the incoming neutrons. For the dump targets, however, the baffles and divertor support structure are located in between the targets and the plasma; therefore, attenuation and a broadening of the neutron spectrum is expected.

Two type of tallies were taken to find the neutron flux in the plates. First, a type 2 tally was calculated which corresponds to the *total* number of neutron that are crossing a surface, i.e. it is not a current which would be a vector. The type 2 tally was calculated to determine the neutron flux across the surface of the plates. Also, a type 4 tally, the cell averaged flux, was taken. The type 4 tally was taken to determine the displacements per atom. A more complete description of type 2 and type 4 tallies can be found in Appendix A.

The area of interest in this model is the top 1 cm (Be, W) or 4 cm (C) of the plasma facing components. The original input file was modified to create cells that fit these specifications. The cell names and locations are:

Cell	1216	Upper inner dump plate (UID)
Cell	1226	Lower inner dump plate (LID)
Cell	1204	Dome (D)
Cell	1213	Lower outer dump plate (LOD)
Cell	1223	Upper outer dump plate (UOD)

The MCNP plot of these cells can be found in Appendix A, Figures A.3-A.7. Using the blueprints that can be found in Chapter 2, Figure 2.6, the armor surface areas and volumes were calculated. In Table 4.1, the surface area of the plates and the volumes of the plates for the one half divertor cassette are shown. In order to determine the total plate volumes for the reactor, it is necessary to multiply the values in Table 4.1 by 96 x 2 (=192). For all candidate materials, the surface area is the same; however, since the C armor is 4 times as thick, its volume is 4 times greater. The units of area and volume in Table 4.1 are in the non-standard units of centimeters because MCNP and DKR-PULSAR require input in these units.

Table 4.1: Surface Area and Volumes of Divertor Plates for Half Cassette

Cell Number	Surface Area [cm^2]	Plate Volume for Be and W [cm^3]	Plate Volume for C [cm^3]
1216 (UID)	628	628	2514
1226 (LID)	394	394	1576
1204 (D)	2059	2059	8236
1213 (LOD)	1217	1217	4869
1223 (UOD)	1141	1141	4565

In Tables 4.2 and 4.3, the total neutron flux across the surfaces of the armor is shown. While the cell number is listed, it is the plasma facing surface of the cell for which the flux is tabulated. The data in Table 4.2 is relevant for a reactor operating with DD fuel at a nominal fusion power of 1.5 GW. The data in Table 4.3 is relevant for a reactor operating with DT fuel at a nominal fusion power of 1.5 GW.

Table 4.2: Neutron Flux on Surface DD Operation: Type 2:n tally

Cell Number	Neutron Flux (Be) [neutrons/cm^{2}s]	Neutron Flux (W) [neutrons/cm^{2}s]	Neutron Flux (C) [neutrons/cm^{2}s]
1216 (UID)	$6.67\text{x}10^{14}$	$6.19\text{x}10^{14}$	$6.68\text{x}10^{14}$
1226 (LID)	$6.76\text{x}10^{14}$	$6.44\text{x}10^{14}$	$7.01\text{x}10^{14}$
1204 (D)	$1.11\text{x}10^{15}$	$1.05\text{x}10^{15}$	$1.1\text{x}10^{15}$
1213 (LOD)	$6.04\text{x}10^{14}$	$5.49\text{x}10^{14}$	$6.42\text{x}10^{14}$
1223 (UOD)	$5.59\text{x}10^{14}$	$5.1\text{x}10^{14}$	$5.88\text{x}10^{14}$

Table 4.3: Neutron Flux on Surface DT Operation: Type 2:n tally

Cell Number	Neutron Flux (Be) [neutrons/cm^{2}s]	Neutron Flux (W) [neutrons/cm^{2}s]	Neutron Flux (C) [neutrons/cm^{2}s]
1216 (UID)	$3.09\text{x}10^{14}$	$2.82\text{x}10^{14}$	$3.16\text{x}10^{14}$
1226 (LID)	$3.17\text{x}10^{14}$	$3.01\text{x}10^{14}$	$3.12\text{x}10^{14}$
1204 (D)	$5.33\text{x}10^{14}$	$1.18\text{x}10^{15}$	$5.07\text{x}10^{15}$
1213 (LOD)	$2.8\text{x}10^{14}$	$2.57\text{x}10^{14}$	$2.88\text{x}10^{14}$
1223 (UOD)	$2.48\text{x}10^{14}$	$2.30\text{x}10^{14}$	$2.69\text{x}10^{14}$

A type 4 tally was also tabulated for each of the divertor plates. This tally is relevant because in order to determine the dpa's in a cell, it is necessary to know how many neutrons are passing through the cell. Therefore, a cell averaged flux, which is normalized to the volume of the cell, determine all those neutrons which pass through any part of the cell. The data for the type 4 tally can be found in Tables 4.4 and 4.5. As before, the data in Table 4.4 is for a reactor running with DD fuel with a nominal fusion power of 1.5 GW. The data in Table 4.5 is for a reactor running with DT fuel with a nominal fusion power of 1.5 GW.

Table 4.4: Cell Averaged Neutron Flux DD Operation: Type 4:n tally

Cell Number	Neutron Flux (Be) [neutrons/cm^{2}s]	Neutron Flux (W) [neutrons/cm^{2}s]	Neutron Flux (C) [neutrons/cm^{2}s]
1216 (UID)	5.60×10^{14}	4.74×10^{14}	5.30×10^{14}
1226 (LID)	4.10×10^{14}	3.50×10^{14}	4.28×10^{14}
1204 (D)	1.08×10^{15}	9.36×10^{14}	1.01×10^{15}
1213 (LOD)	4.28×10^{14}	3.67×10^{14}	4.88×10^{14}
1223 (UOD)	4.24×10^{14}	3.66×10^{14}	4.54×10^{14}

Table 4.5: Cell Averaged Neutron Flux DT Operation: Type 4:n tally

Cell Number	Neutron Flux (Be) [neutrons/cm^{2}s]	Neutron Flux (W) [neutrons/cm^{2}s]	Neutron Flux (C) [neutrons/cm^{2}s]
1216 (UID)	2.62×10^{14}	2.21×10^{14}	2.43×10^{14}
1226 (LID)	1.92×10^{14}	1.63×10^{14}	2.02×10^{14}
1204 (D)	5.32×10^{14}	4.38×10^{14}	4.71×10^{14}
1213 (LOD)	1.98×10^{14}	1.74×10^{14}	2.22×10^{14}
1223 (UOD)	1.92×10^{14}	1.67×10^{14}	2.11×10^{14}

It can clearly be seen that the neutron flux across the two inner dump plates (1216, 1226) is approximately the same and is greater than the outer dump plates (1213, 1223), as would be expected if one looks at the neutron trajectories from the source.(Figure A.1) The neutron flux across the dome is considerably higher. Considering that the dome is closest to the neutron source and is directly in line to the source (minimal shielding from baffles and other components) this result is to be expected. This trend holds for all the tallies. There is a difference between the type 2 tally and the type 4 tally in that the fluxes calculated using the type 2 tally are slightly higher than the fluxes calculated using the type 4 tallies.

The data for the type 4 tally was collected into 46 energy bins, based on the ENDF/B-V group data. The boundaries for these 46 energy bins can be found in Table A.5. The tallies were modified by a multiplier card which were the displacement cross sections. The plot of displacement cross sections for the candidate materials as a function of energy is shown in Figure 4.1. This method was selected because displacement cross sections are not built into MCNP. The microscopic displacement cross sections were generated from the ENDF/B-V group data [35] for ONEDANT and ANISN by M.E. Sawan.

In order to generate displacements per atom per full power year (dpa/FPY) from the data, the type 4 tally results (which have already been multiplied by the cross sections) are multiplied by 10^{-24} to convert the flux to barns from cm^{-2}, by the number of neutrons generated per second, and finally, the number of seconds in a year ($3.1x10^7$). This year of operation is a full power year (FPY) as opposed to a calendar year, a standard method for presenting data. Therefore, the results can easily be scaled to any dpa/time by simply multiplying the results in Table 4.6 and Table 4.7 by the ratio time/$3.1x10^7$. The calculation of dpa/FPY can described by the following equation:

$$dpa/FPY = \phi \cdot 10^{-24} \cdot \sigma_d \cdot S \cdot 3.1 \times 10^7 \qquad (4\text{-}1)$$

where ϕ in the cell averaged flux in cm^{-2}, σ_d is the displacement cross section in barns, S is the neutron source in neutrons/sec, and $3.1x10^7$ is the number of seconds in a year. The value for S is changed depending on whether the reactor was operating with DD as opposed to DT fuel. In both operational modes, the nominal fusion power generated is assumed to be 1.5 GW. [1] Under DD operation the reactions that are occurring are:

$$D + D \rightarrow He^3 + n + 3.27 MeV \qquad (4\text{-}2)$$

$$D + D \rightarrow T + p + 4.03 MeV \qquad (4\text{-}3)$$

As each reaction has a 50% chance of occurring the average energy value of 3.65 MeV was used as shown below. Side reactions of DT and D-He^3 were not considered.

$$\frac{(1.5 \times 10^9 J/\sec) \times neutron/2reactions}{3.65 MeV/reaction \times (1.602 \times 10^{-13} J/MeV)} = 1.28 \times 10^{21} neutrons/\sec \qquad (4\text{-}4)$$

Under DT operation the following reaction is occurring:

$$D + T \rightarrow n + He^4 + 17.6 MeV \qquad (4\text{-}5)$$

Again, using that the power generated is 1.5 GW, the neutron generation rate is:

$$\frac{(1.5 \times 10^9 J/\sec) \times 1neutron/reaction}{17.6 MeV/reaction \times 1.602 \times 10^{-13} J/MeV} = 5.28 \times 10^{20} neutrons/\sec \qquad (4\text{-}6)$$

Figure 4.1 Displacement Cross Sections

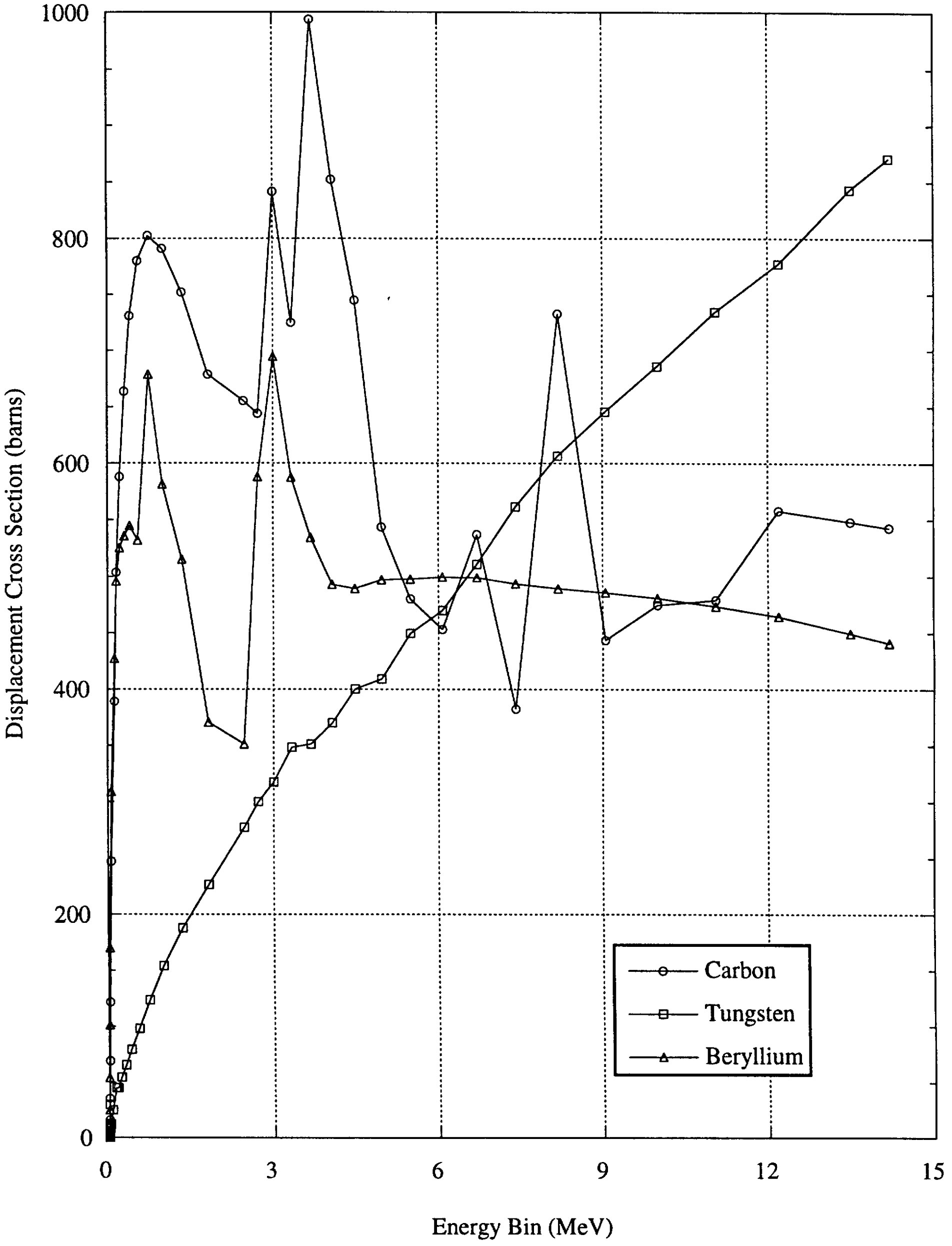

Table 4.6: dpa/FPY for Armor Materials under DD

Cell Number	dpa/FPY (Be)	dpa/FPY (W)	dpa/FPY (C)
1216 (UID)	4.3	0.77	3.9
1226 (LID)	3.3	0.59	3.6
1204 (D)	8.3	2.29	11.1
1213 (LOD)	3.4	0.67	3.8
1223 (UOD)	3.4	0.68	3.6

Table 4.7: dpa/FPY for Armor Materials under DT

Cell Number	dpa/FPY (Be)	dpa/FPY (W)	dpa/FPY (C)
1216 (UID)	2.0	0.32	1.7
1226 (LID)	1.5	0.24	1.5
1204 (D)	3.8	0.95	4.6
1213 (LOD)	1.5	0.28	1.6
1223 (UOD)	1.4	0.28	1.5

4.2 Helium Generation in Beryllium Armor

Another figure of interest is the amount of helium generated in the beryllium armor. As described in Chapter 3, beryllium swells due to internal production of helium if the concentration of helium is known, the amount of swelling $\Delta V/V_0$ can be calculated using Equation 3-11, repeated here for convenience.

$$(\Delta V/V_o)\times 100 = (1.19\pm 0.07)\times 10^{-4} C_{He} + (1.20\pm 0.03)\times 10^{-19} C_{He}{}^2 T^4 \tag{3-11}$$

The reaction for helium production in beryllium is energy dependent. Figure 4.2 shows the helium production cross sections plotted versus neutron energy. Like the displacement cross sections, this data was taken from the ENDF/B-V data file and supplied by M.E. Sawan. The appm of helium can be calculated by:

$$appm = \phi \cdot \sigma_{He} \cdot S \cdot 10^{-24} \cdot 10^{-6} \cdot 3.1\times 10^{7} \tag{4-7}$$

where ϕ is the cell averaged flux, σ_{He} is the helium generation cross section, S is the neutrons incoming per second, 10^{-24} is to convert the flux into barns, 10^{-6} is to convert to appm, and 3.1×10^{7} is number of seconds in a year.

Table 4.8: appm He/FPY for Be Armor Materials under DD and DT

Cell Number	appm He/FPY (DD)	appm He/FPY (DT)
1216 (UID)	2.9×10^{-11}	1.1×10^{-10}
1226 (LID)	2.2×10^{-11}	1.03×10^{-10}
1204 (D)	2.61×10^{-10}	1.421×10^{-9}
1213 (LOD)	5.3×10^{-11}	2.67×10^{-10}
1223 (UOD)	5.3×10^{-11}	2.74×10^{-10}

It can clearly been seen that helium production is larger under DT operation. This is to be expected if one examines Figure 4.2, the cross section for helium production. The cross section is of course dependent on energy and there exists a threshold energy of ~ 1.7 MeV. Since the neutrons produced from the DD reactions are of lower energy, it unlikely that a large amount of helium should be produced under DD operation. However, in either case, the amount of helium produced is negligible and will not lead to swelling.

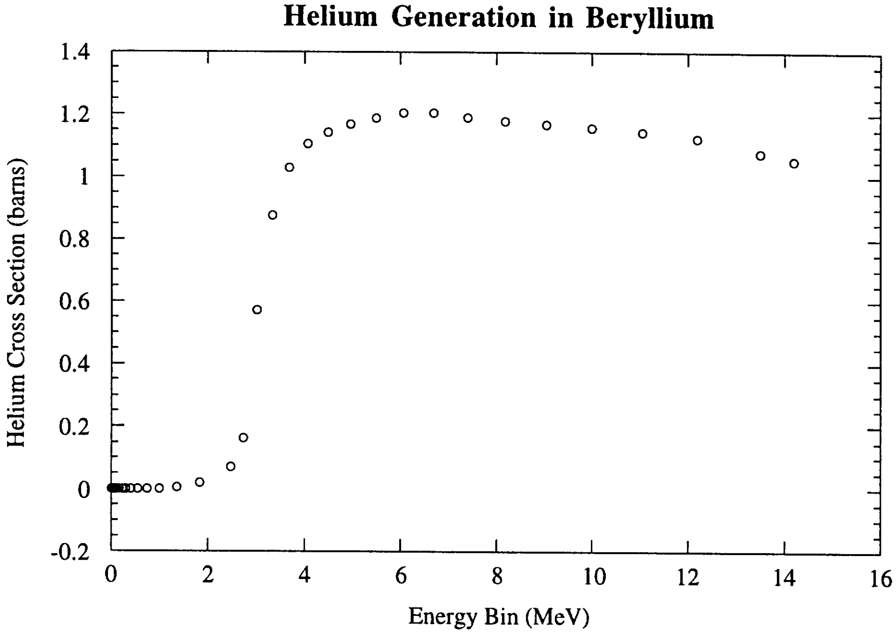

Figure 4.2: Helium generation cross section for beryllium. Threshold value is 1.7 MeV.

4.3 Materials Changes due to Defect Production by Neutron Irradiation

4.3.1 Carbon

For the graphite armor material the crucial material properties to examine are, in decreasing order of importance: the thermal conductivity, the thermal expansion coefficient, the Young's modulus and dimensional changes.[36] As previously mentioned, the grade of carbon selected for this study is Toyo Tanso IG-11. This grade was selected because of its highly isotropic properties and its use in the Japanese HFR reactor. Extensive neutron irradiation studies have been conducted by JAERI on this grade of carbon and changes in the materials properties have been delineated.[30] This study will be the source for many of the material changes for this current work. In this study, irradiation was made to a maximum of approximately 2.5 x 10^{21}n/cm^2 (EDN) {~ 3.9 x 10^{21} n/cm^2 (E > 0.1 MeV)} at temperatures from 1050°C to 1150°C. In order to convert these fission data to the dpa relevant for fusion, the following relationship is used[36]:

$$1 \times 10^{21} n / cm^2 (E > 0.1 MeV) \equiv 1 dpa \tag{4-8}$$

Since $2.5\text{x}10^{21}\text{n/cm}^2$(EDN) is ~ $3.9\text{x}10^{21}\text{n/cm}^2$(E>0.1 MeV) the following relationship can be used to convert to dpa from fluence given for EDN.

$$2.5 \times 10^{21} n / cm^2 (EDN) \equiv 4 dpa \tag{4-9}$$

The results from the JAERI report are shown in Figures 4.3-4.5. The displacements per atom have been added to the plots for clarification. It can been seen from the plots that the irradiation of the samples was in the range of 1.6 to 4.8 dpa. This range overlaps with that predicted by this study. Therefore, these results can be used to give an accurate view of the material properties that the graphite armor would undergo in a full power year. One exception, however, is the dome under DD operation which has a damage of 11 dpa. The JAERI report would underestimate the changes that this plate is undergoing. In Table 4.9, the changes in materials properties for IG-11 graphite for 2 dpa and 4 dpa are illustrated.

Table 4.9 Property changes in IG-11 irradiated graphite

Property	~ 2 dpa	~ 4 dpa
Thermal conductivity (κ/κ_0)	0.72	0.65
Young's Modulus	~ +33%	~+36%
Dimensional Change	-0.25%	-0.70%

The thermal conductivity is greatly changed by the damage induced by the neutron irradiation. This decrease in thermal conductivity will have implications as to whether there can be effective heat removal from graphite armor. The effect of neutron irradiation on the heat transfer properties of graphite armor is investigated in section 4.4. The increase in the Young's Modulus is also quite significant; the graphite is getting stronger and thus, more brittle. This has implications as to the structural integrity of the component. However, as this armor is a high heat flux component, its structural requirements are unclear. In fact, at this time there are no structural requirements specified for the high heat flux components: "*ad hoc* criteria applicable to such components have to be developed, which will be mainly based on a Design by Experiment procedure." [2]

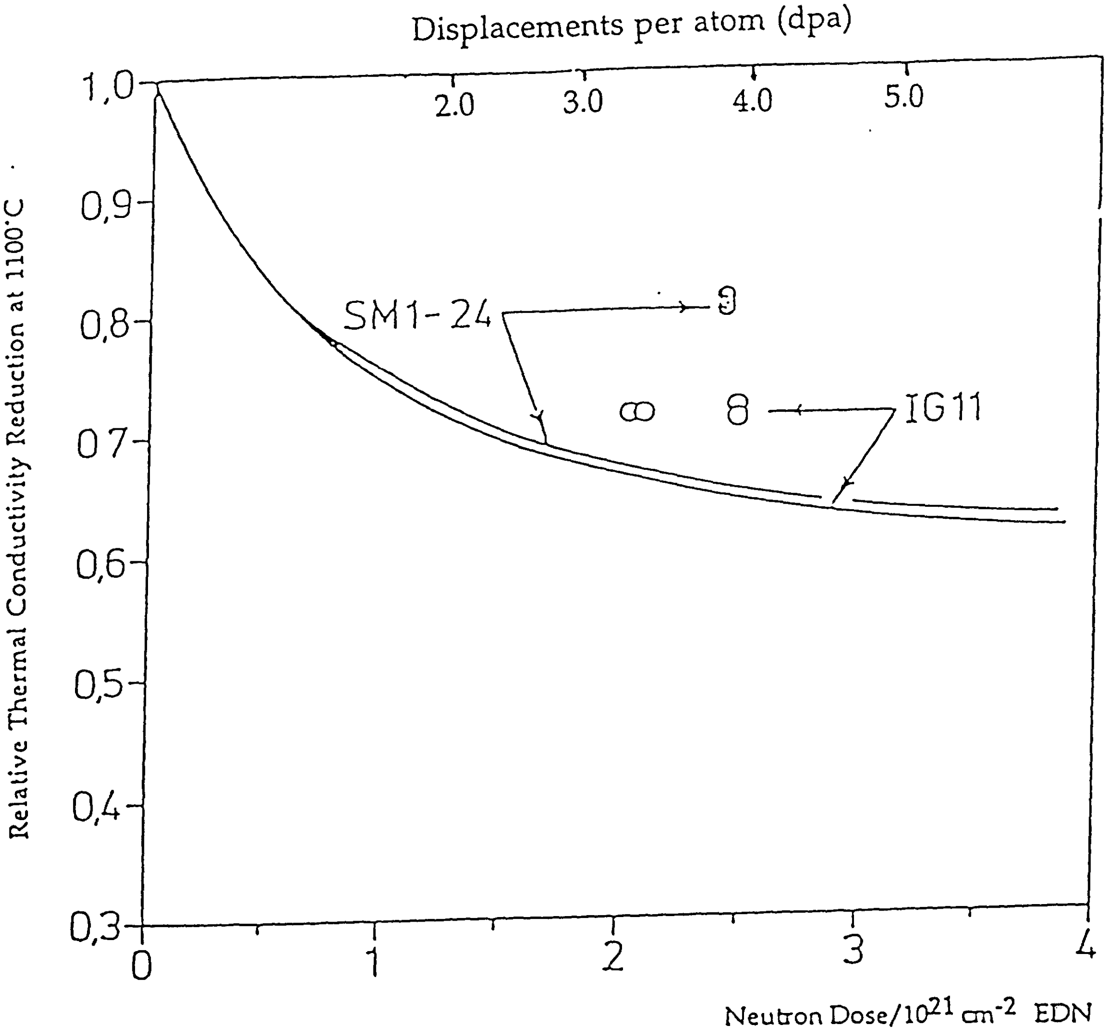

Comparison of Calculated and Measured Reduction in Thermal Conductivity at an Irradiation Temperature of 1100°C

Figure 4.3: Reduction in thermal conductivity of IG-11 graphite under irradiation. Note that the displacements per atom have been added to the plot to clarify the data.[30]

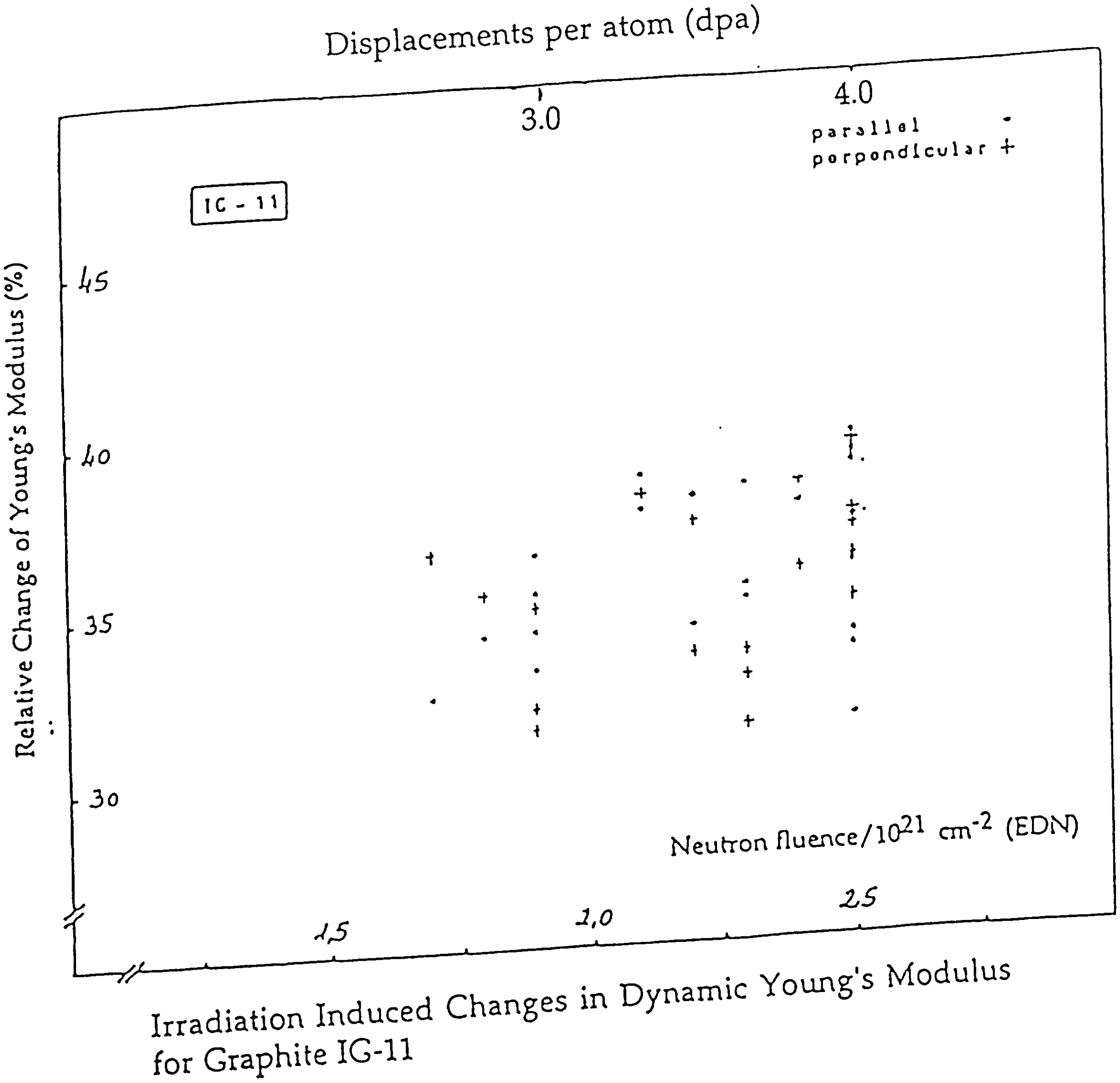

Figure 4.4 : Relative change in the Young's Modulus for IG-11 graphite under neutron irradiation. Note that the displacements per atom have been added to clarify the data.[30]

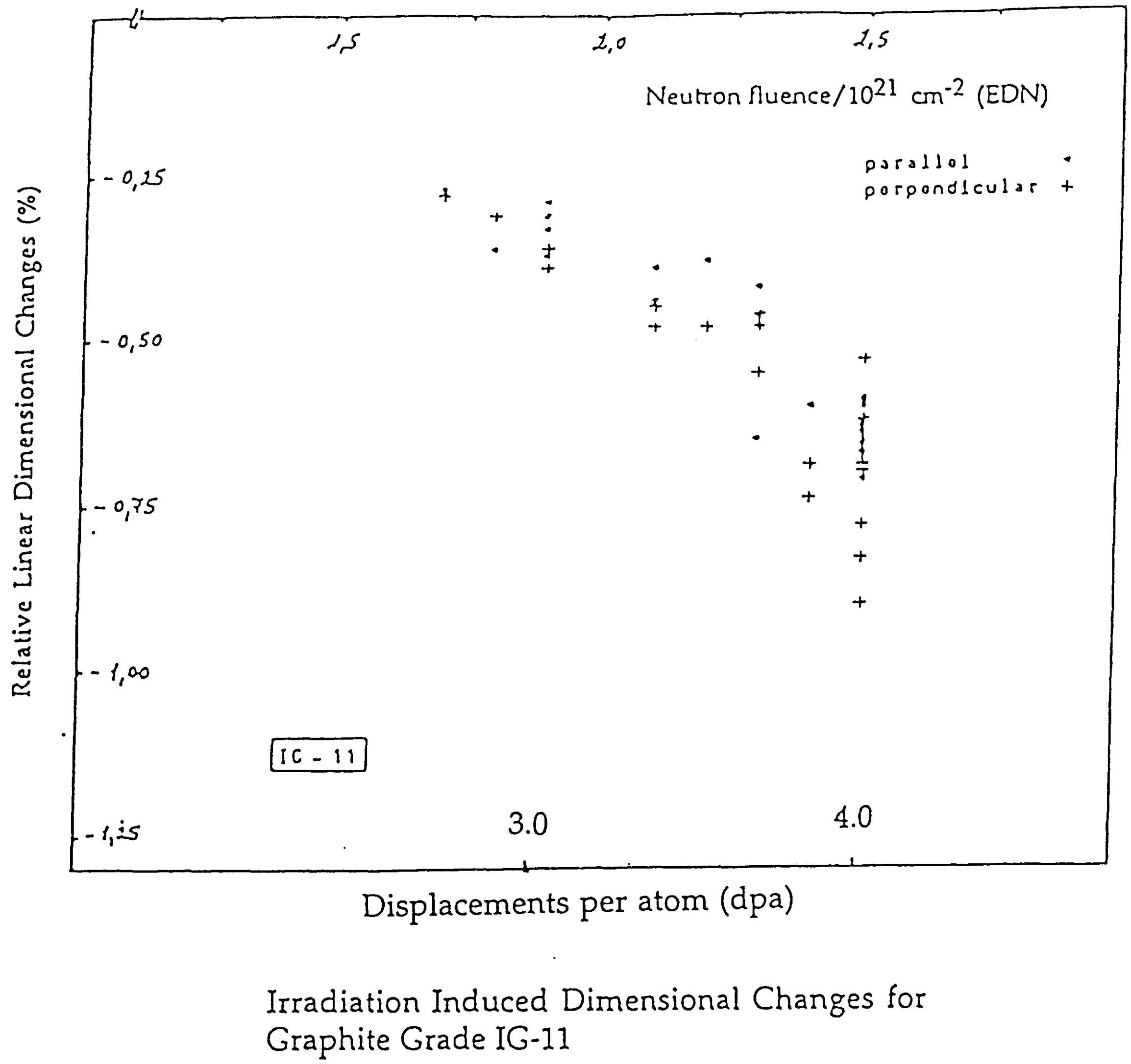

Figure 4.5: Relative linear dimensional change for IG-11 graphite under neutron irradiation. Displacements per atom have been added.[30]

4.3.2 Beryllium

Using the correlation listed in Equation 4-8, the data from the paper by Gelles et al.[28] can be correlated to the dpa calculated earlier. It can be seen that beryllium which receives ~ 1 dpa at a T_{irr} of 600°C, should increase its yield strength. The sample described in [28] increased its yield strength from an unirradiated value of 300 MPa to a value of 450 MPa. Also, a sample of beryllium that was irradiated at 650°C to ~ 1 dpa, showed an elongation of 15% and an irradiated value of the compressive yield strength of 480 MPa. These increases in yield strength could have an important effect of the toughness of the material. For example, a sample that was irradiated to 3.5 dpa showed a 60% reduction in its fracture toughness. This level of damage corresponds to the dome under DT operation (3.8 dpa). Therefore, the beryllium is becoming embrittled in this environment. Hopefully data on more modern grades of beryllium will become available in the near future. Finally, it was clearly shown that the quantity of helium produced in beryllium under both DT and DD operation is negligible.

4.3.3 Tungsten

Due to the immense mass of the tungsten nucleus, the displacement damage for the armor plating is relatively small. The only potentially relevant data found were for a ~ 1 dpa dose. No data were found that would give any indication to changes in material properties from the lower levels of neutron damage. From the data at 1 dpa with T_{irr} ~ 350°C, it appears that some of the armor (i.e. the dome under DT operation) may become brittle under this level of irradiation; however, it must be understood that the operational temperature of tungsten is ~ 1000°C and there should be some recovery of the mechanical properties. Therefore, it is difficult to predict exactly but it seems safe to say that tungsten in the area should be marginally affected by displacement damage. However, the activation and impurity production must still be investigated.

4.4 Effect of Neutron Irradiation on Heat Transfer

The focus of this section is the study of the effect that neutron irradiation will have on the heat transfer properties of a graphite divertor. It was shown previously that the thermal conductivity of graphite is severely degraded under neutron irradiation. Specifically, a graphite tile that accumulates 4 dpa of damage will have a thermal conductivity of 65% of its unirradiated value. Also, the graphite will shrink by 0.7%. (See Table 4.9) Since the thermal conductivity is degraded, it follows that the heat transfer capabilities are also degraded — due to their dependence on the thermal conductivity. In this section, using a simple one dimensional model, the effect of the decrease in thermal conductivity due to neutron irradiation on the surface temperature of the graphite divertor tile is investigated. This study is restricted to steady state operation.

The surface temperature is a parameter of interest in the armor since it is the hottest part of the divertor, and materials limits such as melting point or sublimation temperature will be reached there first. Thus, it is important to limit the surface temperature in order to avoid melting (in the case of Be and W) or sublimation (in the case of C). Also, other thermally activated properties can become a problem, e.g. swelling, if high enough temperatures are reached. For graphite, a generally accepted surface temperature limit is 1100°C (1373K). [37] This temperature limit is to minimize radiation enhanced sublimation (RES) of the carbon.

As discussed earlier in this thesis, the thickness of the graphite armor is expected to be 4 cm. For the divertor geometry, a monoblock configuration as shown in Figure 4.6 is assumed.

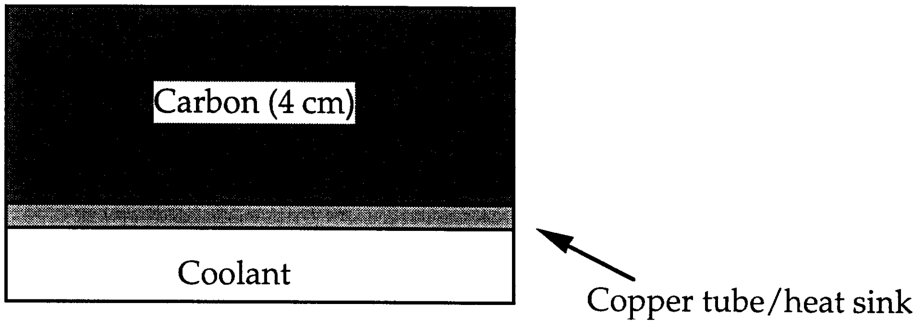

Figure 4.6: One dimensional monoblock design of a graphite divertor

In order to calculate the surface temperature of the graphite armor, the following equations can be used. Equation 4-10 takes into account that there is a tube/heat sink through which the coolant flows. If it can be shown that the major temperature change is in the graphite so ignore the second and third term (letting the thickness of the tube/heat sink go to zero and the heat transfer coefficient go to infinity), then Equation 4-11 can be used instead:

$$T_{Surface} = q \times \left(\frac{d_C}{\kappa_C} + \frac{d_{Cu}}{\kappa_{Cu}} + \frac{1}{h} \right) + T_{Coolant} \tag{4-10}$$

$$T_{Surface} = q \times \left(\frac{d_C}{\kappa_C} \right) + T_{Coolant} \tag{4-11}$$

where q is the surface heat flux (5 MW/m^2), d_C is the thickness of the graphite armor (4 cm), κ_C is the average thermal conductivity of carbon and $T_{Coolant}$ is the temperature of the water coolant (50°C).

The thermal conductivity of graphite is a strong function of temperature as shown in Figure 4.7, for IG-11 graphite. A more accurate plot can be found in Appendix B.1. Since the average temperature of graphite is ~ 500°C, the value of 80 W/mK will be used as an initial value.

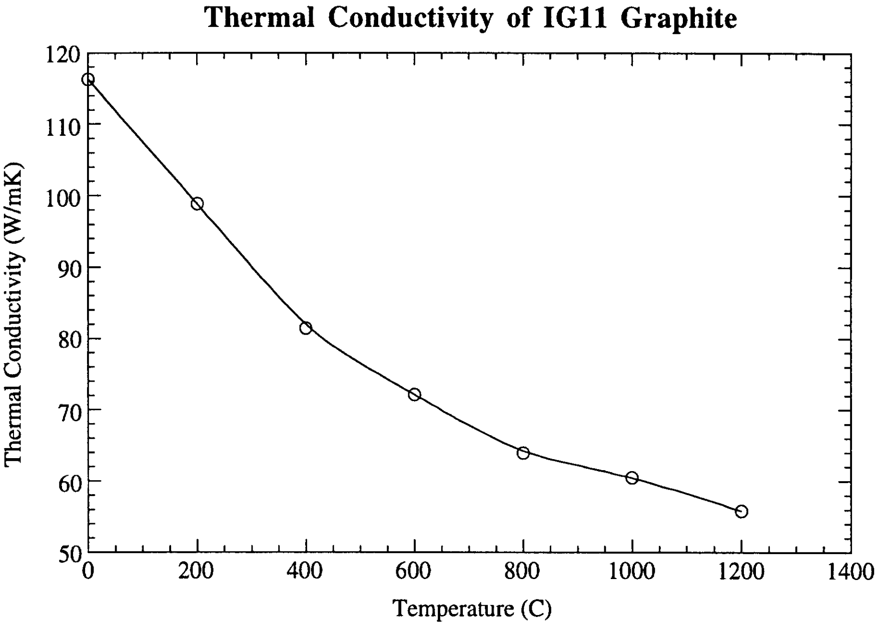

Figure 4.7: The dependence of the thermal conductivity of IG-11 graphite on temperature. [19]

In Figure 4.8, the dependence of thermal conductivity versus irradiation at 500°C is plotted. Since it is known that the thermal conductivity is decreased to 65% after one full power year (assuming 4 dpa of damage), a linear decrease is assumed and plotted. The equation for this decrease is Equation 4-12. It is fundamental to this assumption that the operational temperature of the divertor is constant - which is not.

$$\kappa(t) = \kappa_o - \kappa_o \cdot 1.2 \times 10^{-8} \cdot t \tag{4-12}$$

As shown by Equations 4-10 and 4-11, the plasma facing surface temperature of the graphite is dependent on the thermal conductivity of the graphite. Since the plate is being irradiated the thermal conductivity is decreasing and the surface temperature is increasing; however, at the higher temperature, the amount of damage generated by incident neutrons is lessened. This lessening is due to the fact that at higher temperatures defects are annealed out and thus the thermal conductivity is partially recovered. It is nearly impossible to determine how this annealing affects the thermal conductivity; therefore, it will be ignored and the following calculation can be considered conservative.

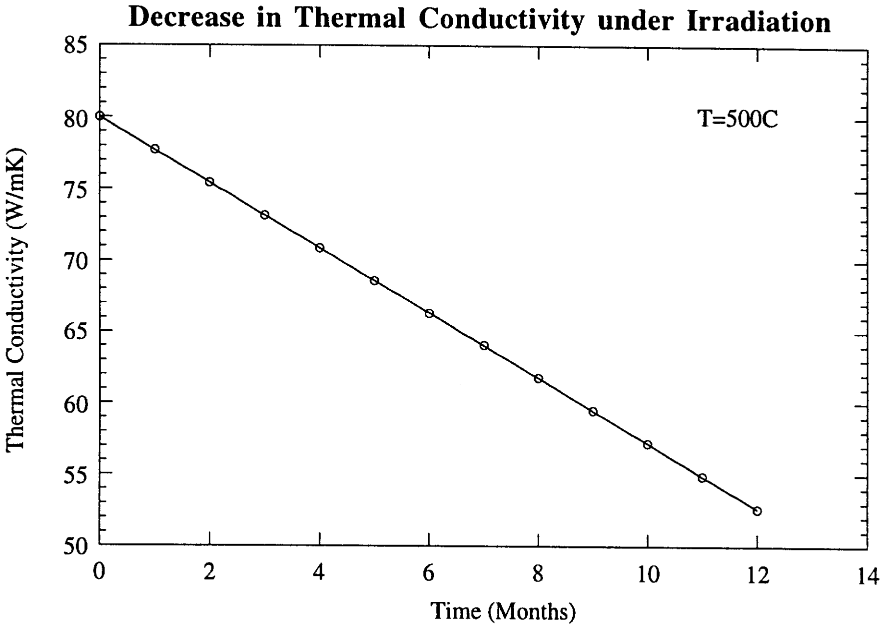

Figure 4.8: The decrease in the thermal conductivity of IG-11 graphite under neutron irradiation at 500°C as a function of time at full power.

It is now possible to calculate the surface temperature of the graphite as a function of time. This plot is shown in Figure 4.9. Note that the surface temperature has increased by 1300K in one year of operation. Also, the difference in temperature between the geometry with the tube and that without the tube is only ~ 100K. As pointed out earlier, it is the trend, not the exact numbers which are of interest. Therefore, Equation 4-11 will be used for the remainder of this study.

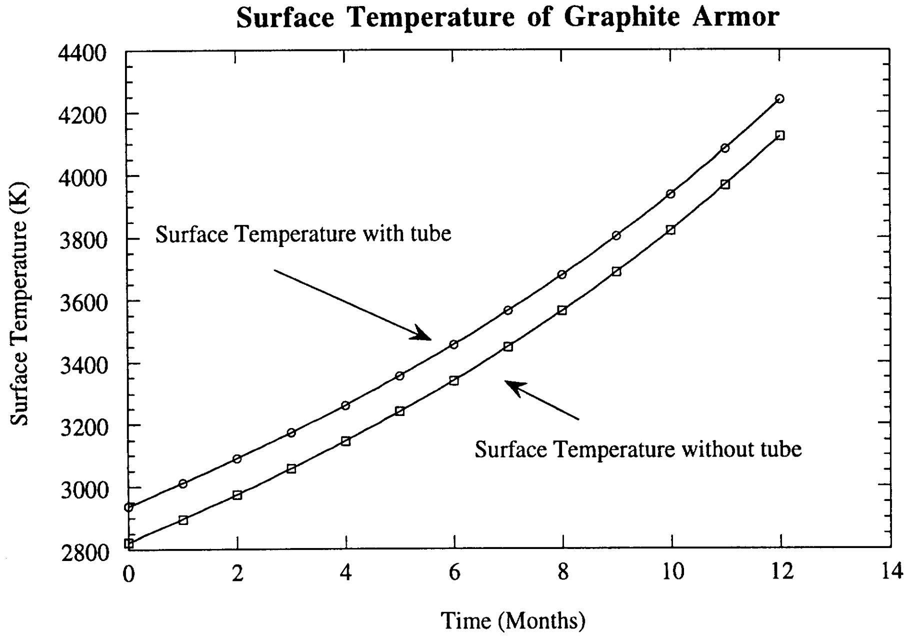

Figure 4.9: Evolution of the surface temperature as a function of time at full power.

This is a very discouraging result; however, at this point, it has not been taken into account that the plasma facing surface of the graphite is being ablated away by impinging ions and neutrals. This erosion will now be incorporated into this study. The figures for the erosion of carbon have been taken from the paper by Wu and Mszanowski [25]. In this paper, the erosion rate of carbon was calculated for divertor relevant conditions: high flux density $>10^{19}$ $cm^{-2}s^{-1}$ and low plasma temperature < 50 eV. The impinging particles were D/T neutrals and D^+/T^+ ions. The neutrals were assumed to have a Maxwellian energy distribution, and the ions were assumed to have a Maxwellian energy distribution shifted by sheath potentials. The erosion rate for carbon including physical sputtering for a plasma temperature of 5 eV was determined to be 1.97×10^{-10}m/s.[25] If chemical sputtering were accounted for, the sputtering rate would increase to 6.3×10^{-9}m/s which would decrease the lifetime by an order of magnitude. In this part, it is necessary to assume that the chemical sputtering has been suppressed (possible by doping with boron). Therefore, the change in thickness as a function of time can be calculated by:

$$thickness(t) = d_C - 1.97\times10^{-10}\cdot t \qquad (4\text{-}12)$$

The change in thickness as a function of time is shown in Figure 4.10.

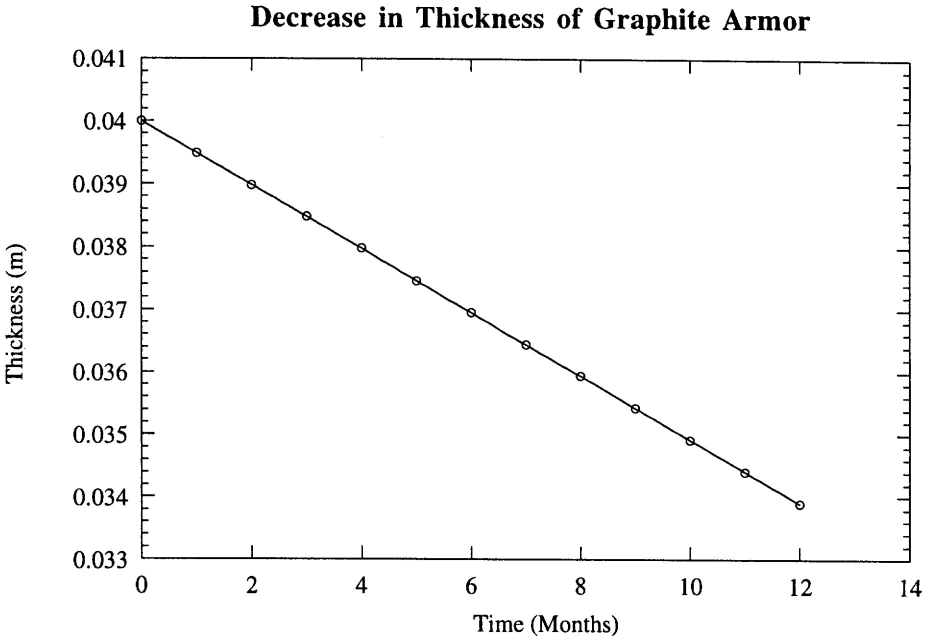

Figure 4.10 : Decrease in the armor thickness due to sputtering by plasma particles as a function of time at full power.

If the surface temperature is now calculated taking into account both the decrease in the thermal conductivity and the thickness, it is found that the increase in temperature is lessened.

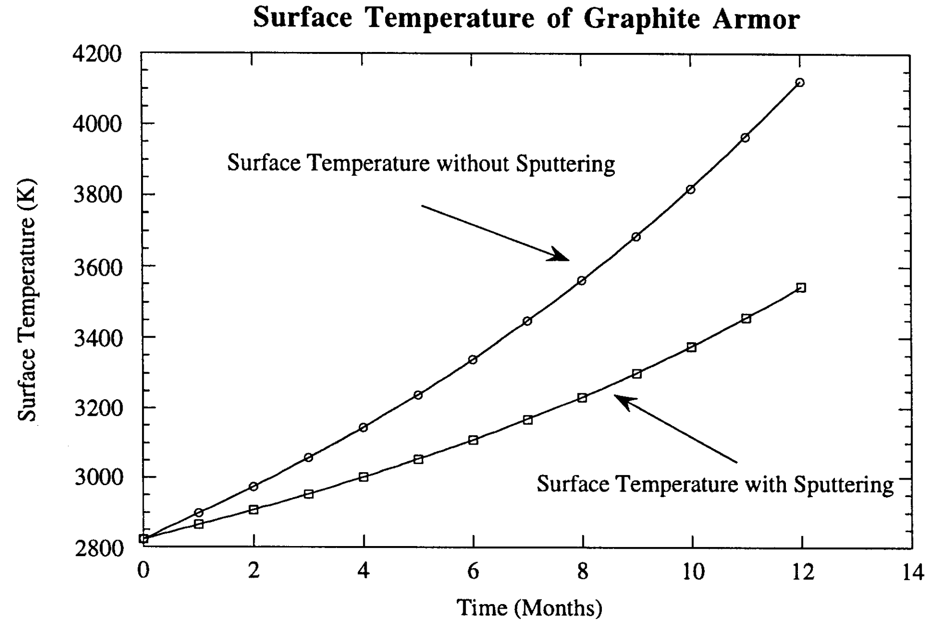

Figure 4.11 Comparison of the increase in the surface temperature using different models as a function of time at full power.

In Figure 4.11, it can be seen that the increase in temperature has decreased from 1300K to 575K. However, if one examines the magnitude of temperature, it is immediately apparent that there is something wrong with this model. The lowest surface temperature achieved is 2800K. This is significantly greater than the recommended maximum of 1373K. Also, the sublimation temperature for graphite in a vacuum is 2473K.[19] Therefore, it can be concluded that this in an invalid design condition. In order to correct this problem, only two options are open: either the thermal conductivity has to be increased or the thickness must be decreased. Since IG-11 is the focus of this study, and it thermal conductivity is fixed, the thickness will be altered. The maximum thickness of armor that allows steady state heat removal of 5 MW/m^2 as a function of thermal conductivity is calculated using Equation (4-9). The results are shown in Figure 4.12. In order to maintain a surface temperature of 1373K with a thermal conductivity of 80W/mK, it is found that the maximum thickness that can be tolerated is 16.8 mm. This is significantly smaller than the suggested value of 40 mm. In order to sustain a thickness of 40 mm it is necessary to use carbon based materials of very high thermal conductivity. In that case, pure pyrolytic graphite is not an option. Other carbon based materials must be investigated, such as carbon fiber reinforced composites (CFC's). However, while CFC's have remarkable high thermal conductivities, they generally exhibit poor resistance to neutron irradiation.

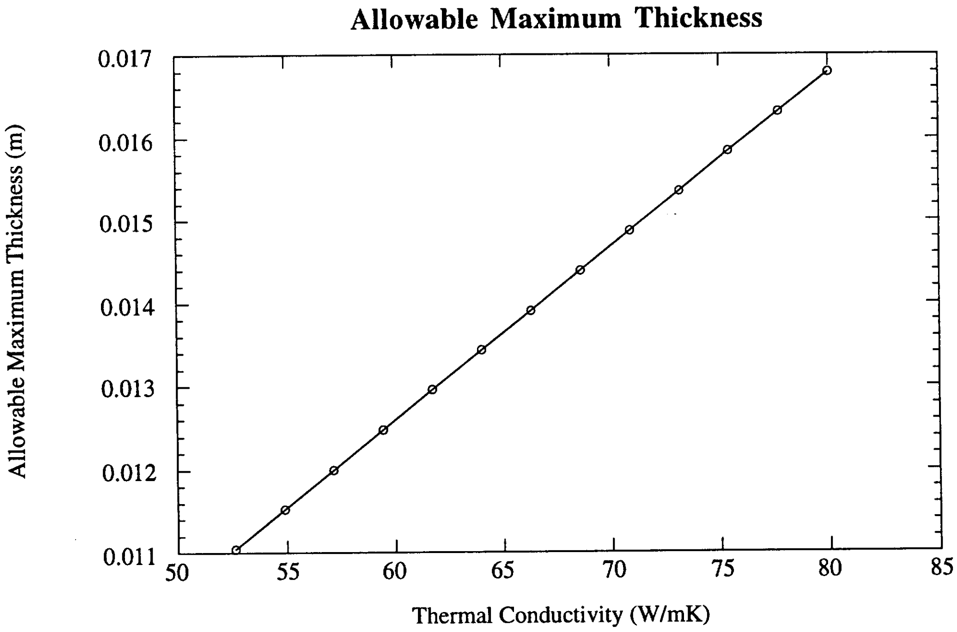

Figure 4.12: Maximum thickness of armor that maintains surface temperature of 1100°C.

The evolution of the surface temperature including the decrease in thermal conductivity and sputtering can be calculated using 16.8 mm as the maximum thickness. The evolution of the surface temperature as a function of time is plotted in Figure 4.13. It can be seen that the increase in the surface temperature has been reduced to 14K. This is an insignificant increase in temperature.

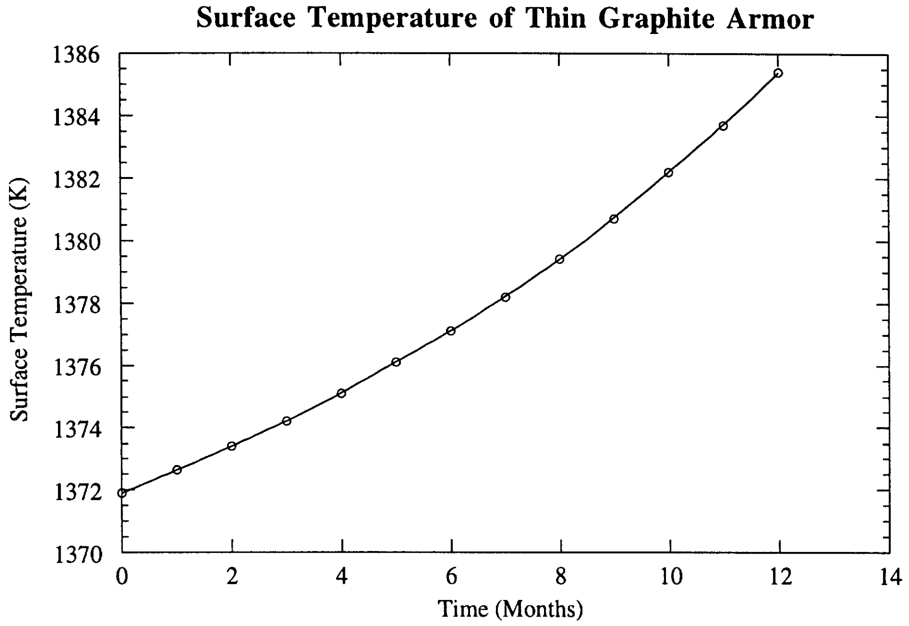

Figure 4.13: Evolution of Surface Temperature including sputtering as a function of time

4.4.1 Limitations of this Model

Steady State Assumption

In this heat transfer model, it has been assumed that the reactor is operating in a steady state mode. Now, if one accounts for disruptions, the picture changes. It has been calculated that in a disruption 30 μm will be lost from the surface of carbon.[2] Therefore, this thin plating could sustain only ~ 400 disruptions before being completely ablated away. This also does not take into account any giant ELMs. A giant ELM should ablate away about 1/4 as much as a disruption.[2] Therefore, the component may have to be replaced more often than once a full power year. However, once the actual lifetime is determined it is simple to extrapolate these results.

1D Model

By utilizing a simple one dimensional model, some information is lost. In effect, if a two dimensional model were used, the change could be up to a factor of 2.

Redeposition

In this model it has been assumed that there is uniform erosion of the armor; however, this is a gross simplification of what is actually occurring . Even though the plasma temperature in from the divertor in a dynamic gas target regime should be < 5 eV, the particle energies may vary significantly around the average over the region. Those particles which have originated closer to the plasma (i.e. on the plasma side of the scrape-off layer (SOL)) should have a much higher temperature than those that originate in that part of the SOL that is closer to the first wall. As sputtering is dependent on the energy of the incoming particle (Equation 3-8), the ablation is not spatially uniform. The region that is being struck by the higher energy particles is being eroded more than the part that is being struck by the lower energy particles. Another consideration is that some of the ablated material is being redeposited. Assumptions could be made as to the sticking coefficient of the redeposited material, but it is not clear what the density or structure of the redeposited material would be. Hence, it is impossible to assume anything physical about the thermal conductivity of the redeposited material. J.N. Brooks [38] has modeled the sputtering erosion for the candidate materials as a function of distance along the divertor channel, including redeposition. In Figure 4.14 a plot of the spatial dependence of the net erosion is shown. It can clearly be seen that for a carbon coated divertor plate, the net erosion varies spatially along the distance from the separatrix to the divertor point.

4.4.2 Summary of Heat Transfer Study

In this section, it has been shown the relationship between the surface temperature of the graphite divertor tiles, the thermal conductivity and the ablation. Using a simple one dimensional model, it has been shown that the decrease in thermal conductivity due to neutron irradiation is balanced by physical sputtering. Therefore, in this model the decrease in thermal conductivity is not a problem. However, it was also shown that a pyrolytic graphite is not capable of operating as 4 cm thick armor. Due to limits on the surface temperature, the maximum thickness for a IG-11 armor at an average temperature of 500°C is 1.68 cm. This reduction in thickness severely compromises the lifetime of the armor. In fact, in this study it was necessary to neglect chemical sputtering in order to obtain a reasonable lifetime for the thin armor. This is not necessarily a valid assumption.

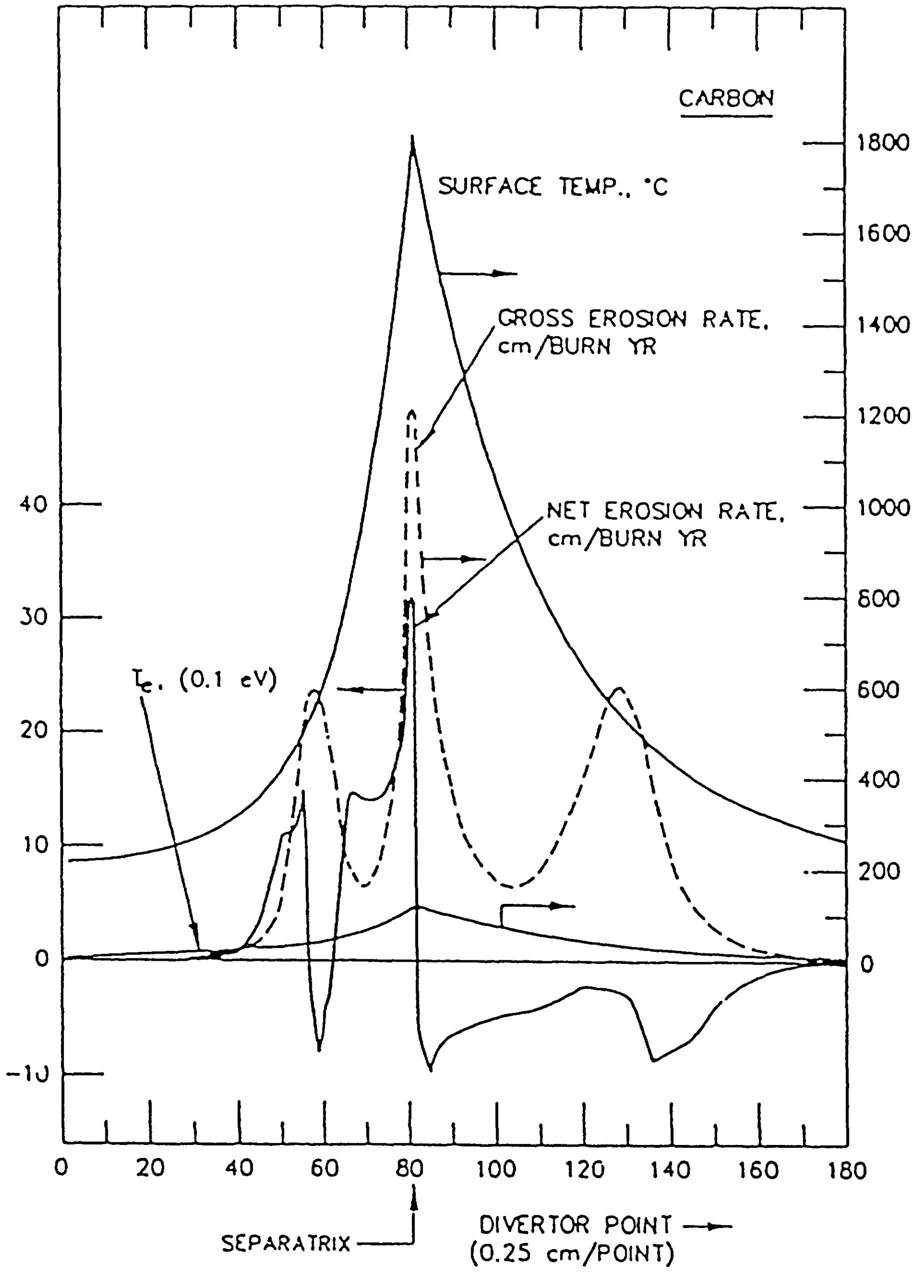

Erosion of a carbon coated divertor plate, for peak surface temperature, T_{s_0} = 1800°C, peak plasma electron temperature, T_{e_0} = 12 eV.

Figure 4.13: Spatial dependence of the erosion of a carbon coated divertor plate. [38]

4.5 Summary

In this chapter the neutron flux across the surface of the divertor plates (type 2:n tally) and through the divertor plates (type 4:n tally) was determined. In addition, the number of displacements per atom (dpa) created by the neutrons passing through the divertor dump targets and dome was determined. These data were used to correlate the fusion neutron flux to fission data.

Under neutron irradiation for one full power year, IG-11 graphite will show a severe drop in thermal conductivity and a strong increase in the Young's modulus. As there exist no structural requirements for the high heat flux components, it is difficult to understand the ramifications of this increase in the Young's Modulus on the operation of the divertor armor. The effects of the degradation in thermal conductivity on carbon was studied. It was found that a IG-11 graphite armor is limited to a 0.0168 m thickness, and that sputtering helps to compensate for the degradation in thermal conductivity.

Beryllium is also affected by neutron irradiation. The beryllium armor was determined to receive several dpa's under DT operation. Correlating these results to published data, it can be seen that the beryllium in this environment should become embrittled. However, it was shown that swelling due to helium production should not be a problem.

Since tungsten is such a massive atom, even high energy neutrons have a small chance of displacing the atoms from their equilibrium lattice positions. The amount of dpa's calculated in this study is very low, and the data found overlapped only part of the results. However, with the data that were found, it seems that there may be a possible loss of ductility in parts of the armor, but the fact that the armor is at a high temperature may allow for the recovery of the displacement damage. It is not possible to extrapolate from high levels of neutron damage to low levels and predict accurately the commensurate material changes. It still remains to be seen to what extent the tungsten is activated by high energy neutrons.

CHAPTER 5

By the pricking of my thumbs,
Something wicked this way comes.
William Shakespeare

Activation of Armor Materials

5.1 Introduction

Activation of the armor material is an important consideration since one potential advantage of fusion is a reduced amount of radioactive waste generation compared to fission. Since the divertor is a component that is often replaced, and is active when replaced, the amount of activation is an issue if the volume of waste is a consideration. Also, even though this component is remotely handled, for safety reasons it is important to know how much activity is generated. In this study, the code DKR-PULSAR is used to determine the activation of the divertor armor after being in operation for 1000 pulses.

5.2 DKR-PULSAR Code

DKR-PULSAR Ver. 1.0 is a new version of the DKR-ICF [39] code which implements methods for the exact treatment of pulsed history irradiation. It is being developed by D.L. Henderson, J.E. Sisolak and S.E. Spangler at the Fusion Technology Institute at the University of Wisconsin-Madison. The code was made available by Professor Paul Henderson for use on the University of Wisconsin HP-735/99. The main advantages of this code are that it has a straightforward user interface, and more importantly, it has the ability to model pulsed operation. In the input file, one enters the cell averaged flux divided into 46 energy bins, the pulsing scheme and the material constituents. The material constituents are obtained from data supplied by the manufacturers and are shown in Table 5.1 for the three materials of interest. The required input is the atom density, so that was determined for all the components. The code then determined the atomic percent of all the isotopes, i.e. there are four stable naturally occurring isotopes of tungsten and the code calculated the appropriate atom percent for each isotope based on the user input. The modified atom density for each isotope that was generated by the code is shown in Table 5.2.

The pulsing scheme is also to be specified as an input. For this model, the pulsing scheme is 1000 pulses of 1000s burn time and 2200 seconds between pulses. This 1000 pulse model was decided upon due to the lifetime limitation described in Chapter 3. Due to sputtering, beryllium is limited to approximately 1000 pulses; 1000 pulses is also the minimum acceptable lifetime for the component[2]; therefore, it was deemed an appropriate operating scheme. This is much less than 12 full power months (~0.4 full power months), but as previously discussed when the actual operating parameters are known, the results can be easily scaled.

The data generated from the code is given for twelve time steps after shutdown. If necessary the user can input their own choice of time steps after shutdown, but in this case the built-in option was utilized. The input files for the three materials can be found in Appendix C. The output data are the total activity and the afterheat as a function of time. The definition of the terms and their values will be discussed in section 5.4.

5.3 Components of Candidate Materials

While the selected materials grades are of very high quality, it would be very costly to employ materials that were 100% pure. The IG-11 graphite is the most highly purified, followed by the beryllium and finally the tungsten. This grade of tungsten is nominally 99.95% pure which is a high purity for tungsten; however, due to its high melting point and high atomic mass it is difficult to reach higher levels of purity. As seen in Table 5.1, there are many more impurities in tungsten than in the carbon and beryllium. This may have important effects on the activation properties. However, it is interesting to note that all three candidates have impurities of iron, aluminum, magnesium, and silicon. Therefore, if any of these impurities become highly activated, it will be a problem for all three materials.

Table 5.1 Impurity Levels in Candidate Materials

Carbon		Beryllium		Tungsten	
IG-11 Grade by Toyo Tanso High Purity		Brush Wellman S-65 Grade (weight percent)		Tungsten Plate: WP-1 by Climax Specialty Metals	
C	Balance	Be	99.0% (Min)	W	99.95% (w/o)
Al	0.3ppm (Max)	BeO	1% (Max)	Al	0.002% (Max)
Fe	1.0ppm (Max)	Al	0.06%	Ca	0.003%
Mg	0.1ppm (Max)	C	0.1%	Cr	0.002%
Si	0.1ppm (Max)	Fe	0.08%	Cu	0.002%
		Mg	0.06%	Fe	0.003%
		Si	0.06%	Pb	0.002%
		Other	0.04%	Mg	0.002%
				Mn	0.002%
				Ni	0.003%
				Si	0.002%
				Sn	0.002%
				Ti	0.002%
				C	0.005%

The information in Table 5.1 is in the same form as it was supplied by the manufacturers. These numbers in Table 5.1 must be converted into atom density. This calculation was done as follows. The atom density in atoms/cm^3 of a majority species can be easily calculated as follows:

$$N_{majority} = \frac{\rho}{A} N_A \tag{5-1}$$

where ρ density of the majority species in g/cm^3, A is the atomic mass in g/mole and N_A is Avagadro's number, 6.02x10^{23}atoms/mole. To convert the impurities for IG-11 which are in ppm (parts per million by weight), the ppm's were first converted to weight fraction. To convert the impurities to atomic density when given in weight fraction, the following relation was used:

$$w = \frac{x \cdot A_{impurity}}{x \cdot A_{impurity} + (1-x) \cdot A_{majority}} \tag{5-2}$$

where w is the weight fraction, x is the atomic fraction, $A_{impurity}$ and $A_{majority}$ are the atomic masses of the impurity and majority species, respectively. To calculate the number density of the impurities, Equation 5-2 is solved for x and multiplied by $N_{majority}$. It is assumed that the $N_{impurity} << N_{majority}$. This resulting equation is Equation 5-3.

$$N_{impurity} = N_{majority} \cdot w \cdot \left(\frac{A_{majority}}{A_{impurity} + w \cdot A_{majority} - w \cdot A_{impurity}} \right) \tag{5-3}$$

where $N_{majority}$ is defined in Equation (5-1), w is the weight fraction of the impurity (Table 5.1), and $A_{impurity}$ is the atomic mass of the impurity and $A_{majority}$ is the atomic mass of the majority species.

The code then calculated the appropriate atom density for all naturally occurring stable isotopes. For example carbon contains of both Carbon-12 and Carbon-13. These revised data are shown in Table 5.2. The isotopes are listed in ascending Z order. The number on the right hand side of the columns is the number density of that isotope.

Table 5.2: Atom Densities for all Constituent Isotopes

Beryllium		Carbon		Tungsten	
Isotope	**Atoms/cm^3**	**Isotope**	**Atoms/cm^3**	**Isotope**	**Atoms/cm^3**
Be-9	1.24x10^{23}	C-12	8.7816x10^{22}	C-12	4.7844x10^{19}
C-12	9.1801x10^{19}	C-13	9.839x10^{20}	C-13	5.3605x10^{17}
C-13	1.0286x10^{18}	Mg-24	3.4598x10^{15}	Mg-24	7.583x10^{18}
O-16	5.5745x10^{20}	Mg-25	4.38x10^{14}	Mg-25	9.60x10^{17}
O-17	2.0676x10^{17}	Mg-26	4.8224x10^{14}	Mg-26	1.057x10^{18}
O-18	1.14x10^{18}	Al-27	1.184x10^{16}	Al-27	8.605x10^{18}
Mg-24	2.1722x10^{19}	Si-28	3.4955x10^{15}	Si-28	7.6302x10^{18}
Mg-25	2.75x10^{18}	Si-29	1.7699x10^{14}	Si-29	3.8635x10^{17}
Mg-26	3.0277x10^{18}	Si-30	1.1749x10^{14}	Si-30	2.5646x1017
Al-27	2.476x10^{19}	Fe-54	1.121x10^{15}	Ca-40	8.4465x10^{18}
Si-28	2.1951x10^{19}	Fe-56	1.7427x10^{16}	Ca-42	5.6373x10^{16}
Si-29	1.1115x10^{18}	Fe-57	3.99x10^{14}	Ca-43	1.1763x10^{16}
Si-30	7.378x10^{17}	Fe-58	5.32x10^{13}	Ca-44	1.8175x10^{17}
Fe-54	9.3928x10^{17}			Ca-43	1.1763x10^{16}
Fe-56	1.14602x10^{19}			Ca-44	1.8175x10^{17}
Fe-57	3.3432x10^{17}			Ca-46	3.4852x10^{14}
Fe-58	4.4576x10^{16}			Ca-48	1.6293x10^{16}
				Ti-46	3.8808x10^{17}
				Ti-47	3.5412x10^{17}
				Ti-48	3.58x10^{18}
				Ti-49	2.6681x10^{17}
				Ti-50	2.6195x10^{17}
				Cr-50	1.9413x10^{17}
				Cr-52	3.7437x10^{18}
				Cr-53	4.2446x10^{17}
				Cr-54	1.0567x10^{17}
				Mn-55	4.225x10^{18}
				Fe-54	3.6722x10^{17}
				Fe-56	5.7087x10^{18}
				Fe-57	1.307x10^{17}
				Fe-58	1.7427x10^{16}
				Ni-58	4.0539x10^{18}
				Ni-60	1.5498x10^{18}
				Ni-61	6.7099x10^{16}
				Ni-62	2.1317x10^{17}
				Ni-64	5.4036x10^{16}
				Cu-63	2.5309x10^{18}
				Cu-65	1.1281x10^{18}
				Sn-112	1.8993x10^{16}
				Sn-114	1.2727x10^{16}
				Sn-115	7.0488x10^{15}
				Sn-116	2.845x10^{17}

				Sn-117	1.5037x10^{17}
				Sn-118	4.7423x10^{17}
				Sn-119	1.68x10^{17}
				Sn-120	6.3811x10^{17}
				Sn-122	9.0655x10^{16}
				Sn-124	1.1337x10^{17}
				W-180	7.5720x10^{19}
				W-182	1.6595x10^{22}
				W-183	9.0107x10^{21}
				W-184	1.9372x10^{22}
				W-186	18047x10^{22}
				Pb-204	1.568x10^{16}
				Pb-206	2.6992x10^{17}
				Pb-207	2.4752x10^{17}
				Pb-208	5.8688x10^{17}

5.4 Activation of Armor Materials

The data generated by DKR-PULSAR is the total activity for the entire component. Therefore, the data were divided by 96 to get the activity per cassette. This is considered to be an important parameter since if one cassette has to be removed, its activity should be known.

Even though the divertors are going to be removed by use of a remote handling system, it may be prudent to delay removal so that short-lived radioactive products can decay, thus diminishing the hazard potential to the surroundings. As previously mentioned, the data generated was for 12 time steps after shutdown. For removal from the reactor, the time period of concern is shutdown to at least one week. The time steps in this range are 0.0 seconds, 1 minute, 10 minutes, 1 hours, 6 hours, 1 day and 1 week. The values of activity per cassette from shutdown to one week are plotted and shown in Figures 5.1 to 5.3. Only three of the time steps are labeled due to space limitations; however, the other data points correspond the aforementioned time steps.

5.4.1 Short-Lived Isotopes

There are several characteristics of interest in Figures 5.1 to 5.3. Note that there is a rapid decrease in radioactivity in the time period of a few hours. Note that the x-axis is linear. For each material, short-lived nuclides are generated. It is a general rule of thumb that the shorter the lifetime of an element, the higher is its activity level. In the case of the carbon, the rapid drop-off in activity is due to the disappearance of Boron-12 and Boron-13 which have half-lives of 20.20 ms and 17.3 ms respectively.[5] These boron isotopes are generated from the Carbon-12 and Carbon-13. Therefore, the base material is the source of short-lived activity, so increased purity will not affect the levels. For beryllium, the short-lived activity is due to the presence of Helium-6 which has a half-life of 805 ms. The Helium-6 is generated from the beryllium. In tungsten, the short-lived activity is generated from Tungsten-183m, Tungsten-185m and Tungsten-187. Their half-lives are 5.15 s, 1.65 m and 23.9 h respectively and all are produced from reactions with the base material.

It is clear by the above discussion that the important short-lived isotopes are generated through reactions with the base material. Therefore, increasing the purity will not affect these levels. The only option to decreasing this activity is through material selection.

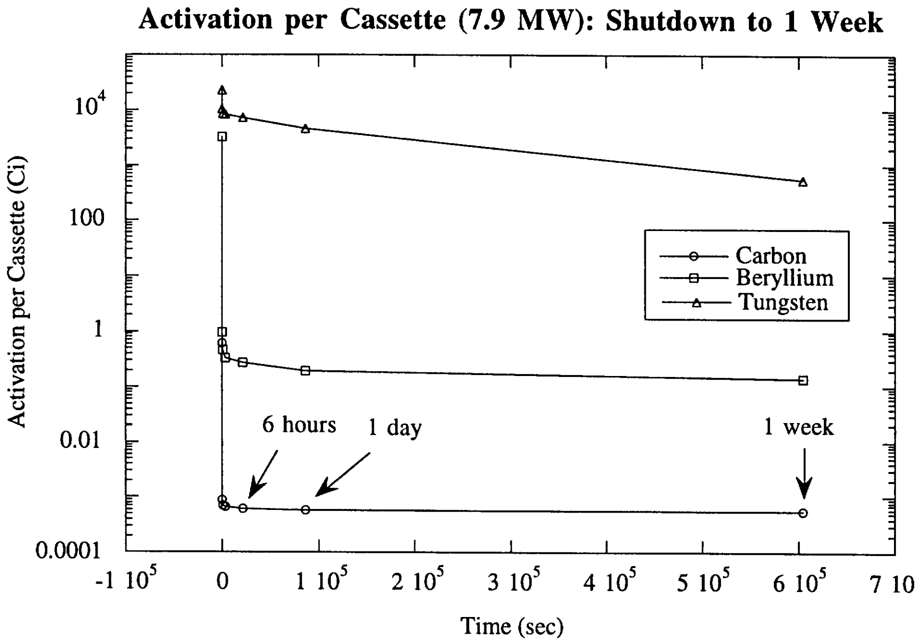

Figure 5.1: Activity per Cassette under ohmic operation from shutdown to one week.

---

[5] **NB**: All values for half-lives come from [38].

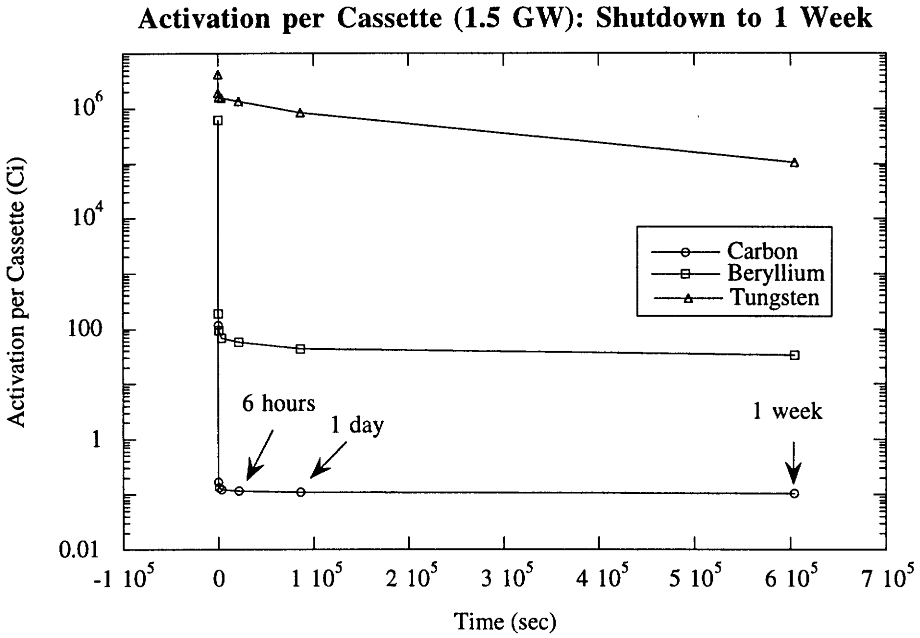

Figure 5.2: Activity per cassette under BPP operation from shutdown to one week.

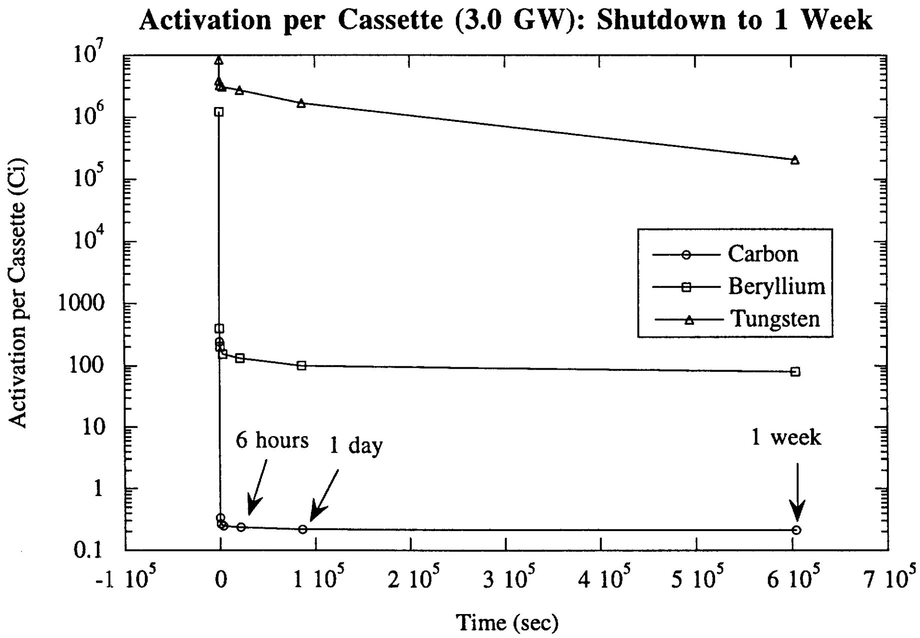

Figure 5.3: Activity per cassette under EPP operation from shutdown to one week.

5.4.2 Long Term Activity

For long term storage, it is also important to know the activity over extended periods of time. The activity per cassette has been calculated to a maximum of 1000 years. Note that the x-axis is now logarithmic due to the large time scale. These results are shown in Figures 5.4 to 5.6. It can been seen by the sudden change in slope that there are certain isotopes which have finally decayed away. Note that in the carbon there is a sudden change in slope after ~10 years. This is due to decay of Fe-55 which has a half-life of 2.68 years. In beryllium, there is also a change after 10 years, i.e. the activity drops by over two orders of magnitude between 10 years and 100 years. This sudden change is due primarily to the decay of tritium , which has a half-life of 12.9 years, and Fe-55. There is a lesser contribution from Mn-54 which has a half-life of 312.2 days. Its activity drops three orders of magnitude from 1 year to 10 years; however, this artifact is concealed by the tritium and Fe-55. What is of interest is that the manganese is generated from the iron impurity; therefore, removal of the iron may significantly affect the long term activity in beryllium. In tungsten, there is an order of magnitude drop between 1 month and year. The main contributor at 1 month is W-185 which has two isomeric states, one of which has a half-life of 1.65 minutes and the other 74.8 days. The disappearance of one of these states is the reason for the rapid decrease after 1 month. Between 1 year and ten years there is an even bigger drop in activity; this is due to the disappearance of W-185 and to a lesser extent W-181 which has a half-life of 121.0 days.

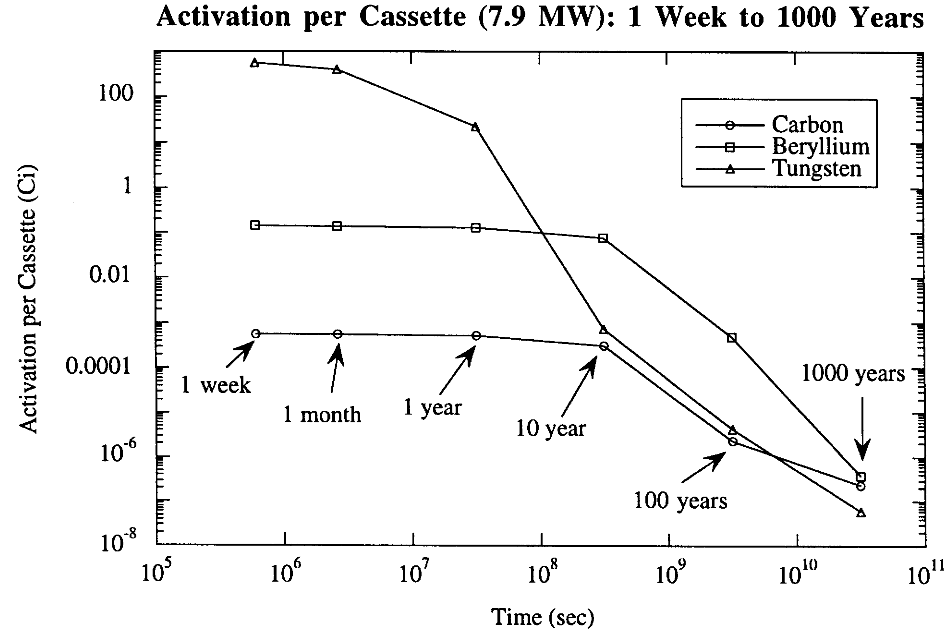

Figure 5.4: Activity per cassette under ohmic operation from one week to 1000 years.

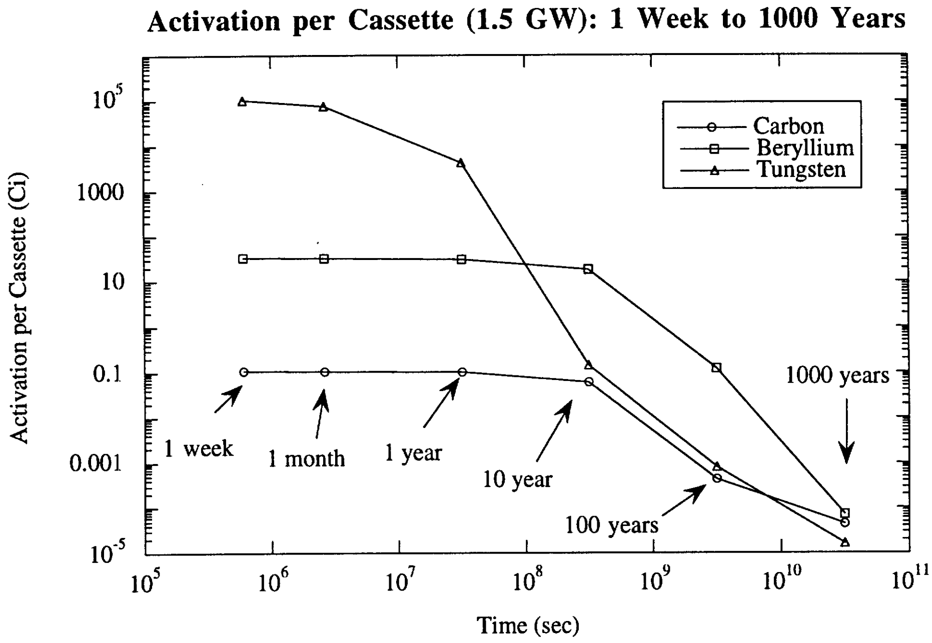

Figure 5.5: Activity per cassette under BPP operation from one week to 1000 years.

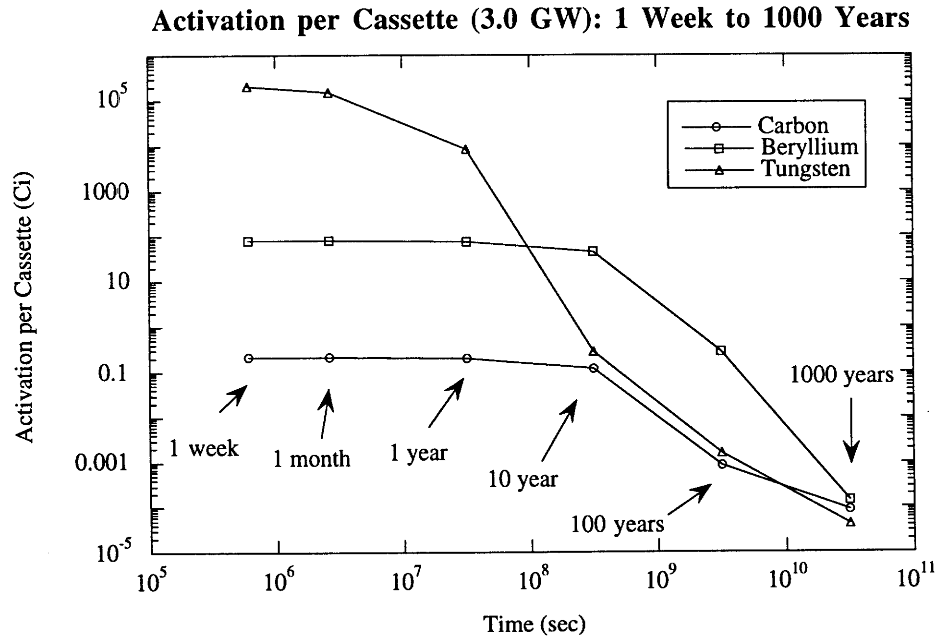

Figure 5.6: Activity per cassette under EPP operation from one week to 1000 years.

5.4 Afterheat

Since the armor material is activated, it will also have internal energy generation. This generation of energy is due to the fact that when the unstable isotopes decay through the emission of energetic particles and photons, the majority of the energetic particles deposit their heat into the armor. (Those particles generated on the surface or those whose mean free path is greater than the depth at which they are produced do not contribute to the energy generation). This energy deposition is what leads to the internal power generation. The levels of afterheat depend on the level of activation. In Figures 5.7 to 5.12, the afterheat[6] is plotted versus the time after shutdown. It can be clearly seen that the tungsten will have the most internal heat generation which is commensurate to the fact that it is the most highly activated. Again, beryllium has an afterheat that is several orders of magnitude less than that of tungsten and graphite has an afterheat several orders of magnitude less than that of beryllium. It is also interesting to note that while beryllium and graphite appear to undergo an exponential decrease in afterheat, the tungsten afterheat level decreases linearly.

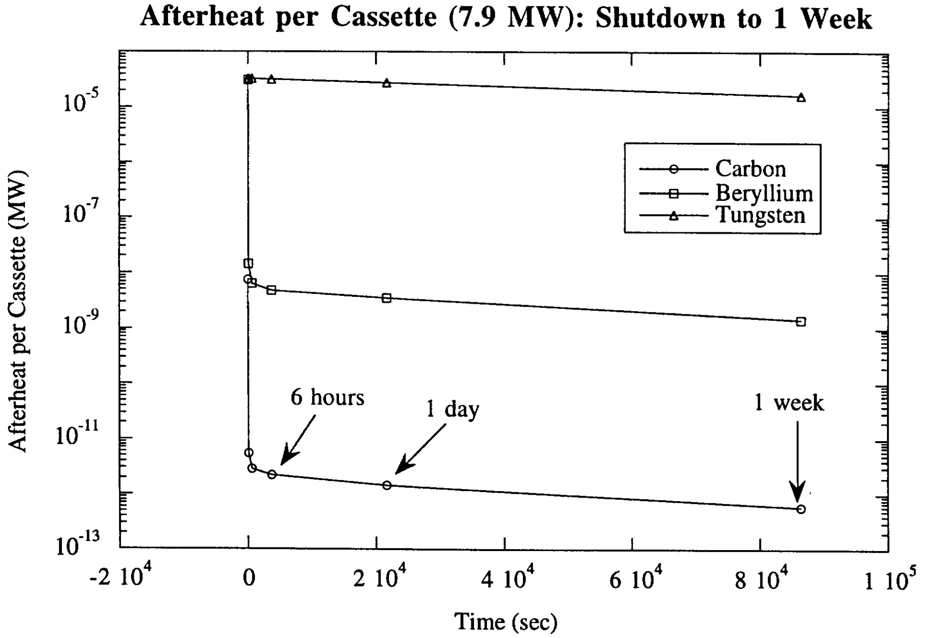

Figure 5.7: Afterheat per cassette under ohmic operation from shutdown to 1 week.

---

[6] The afterheat part of the code does need updating so the numbers are order of magnitude studies only.

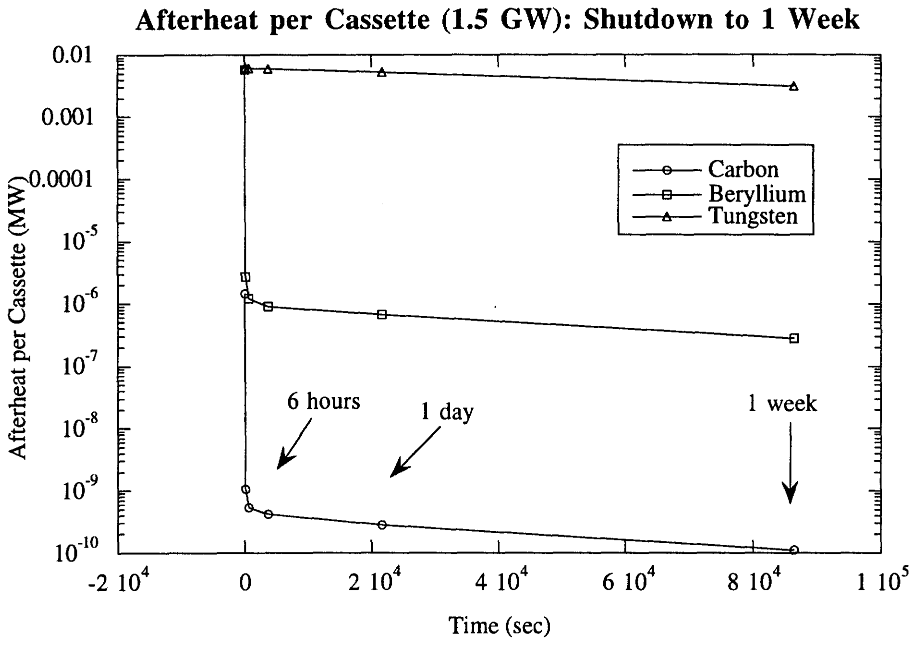

Figure 5.8: Afterheat per cassette under BPP operation from shutdown to 1 week.

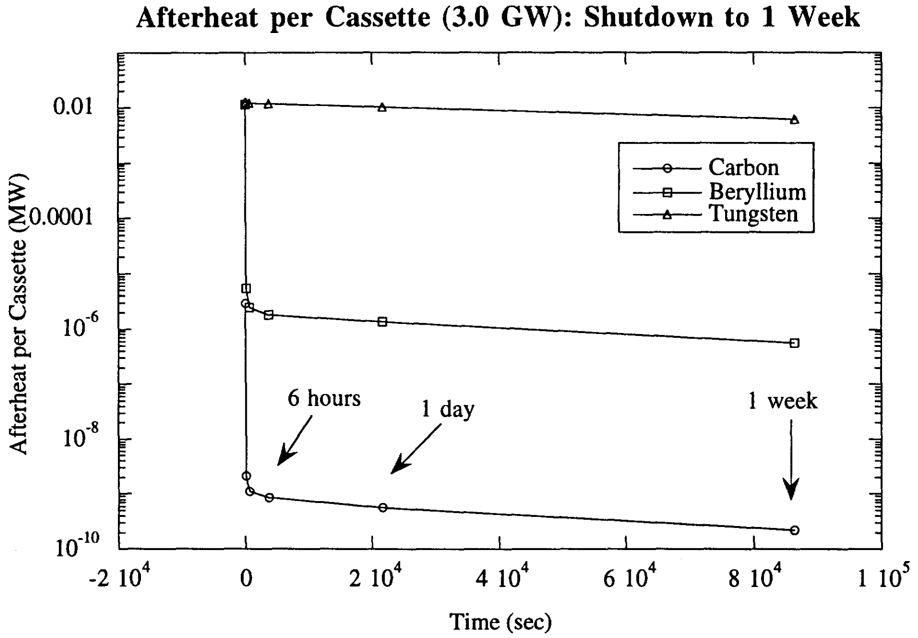

Figure 5.9: Afterheat of cassette under EPP operation from shutdown to 1 week.

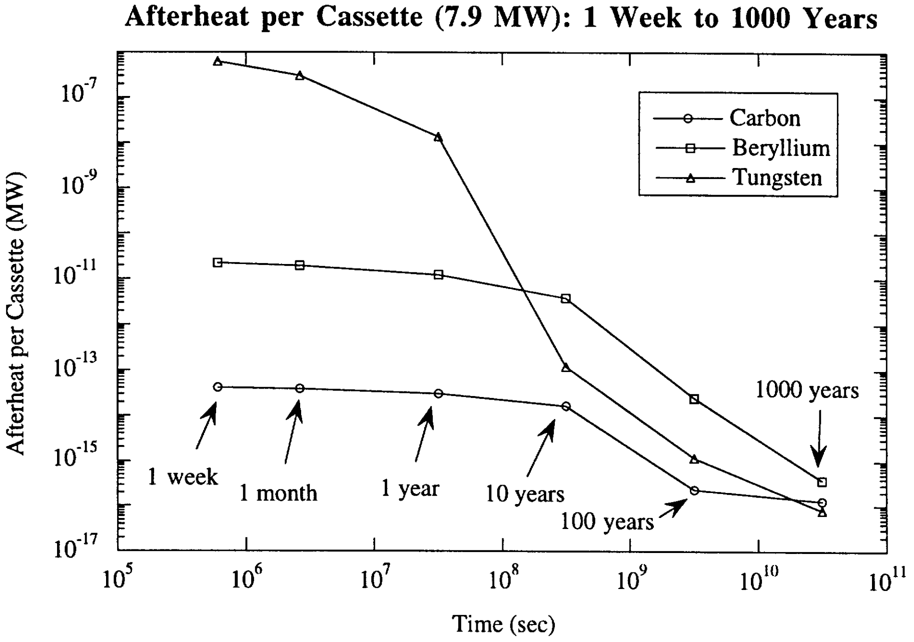

Figure 5.10: Afterheat per cassette under ohmic operation from 1 week to 1000 years.

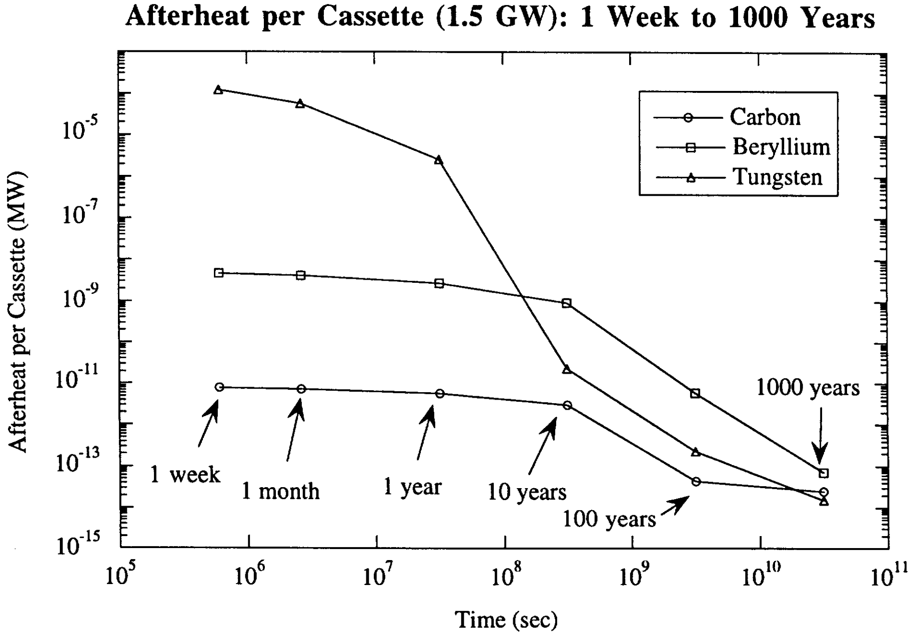

Figure 5.11: Afterheat of cassette under BPP operation from 1 week to 1000 years.

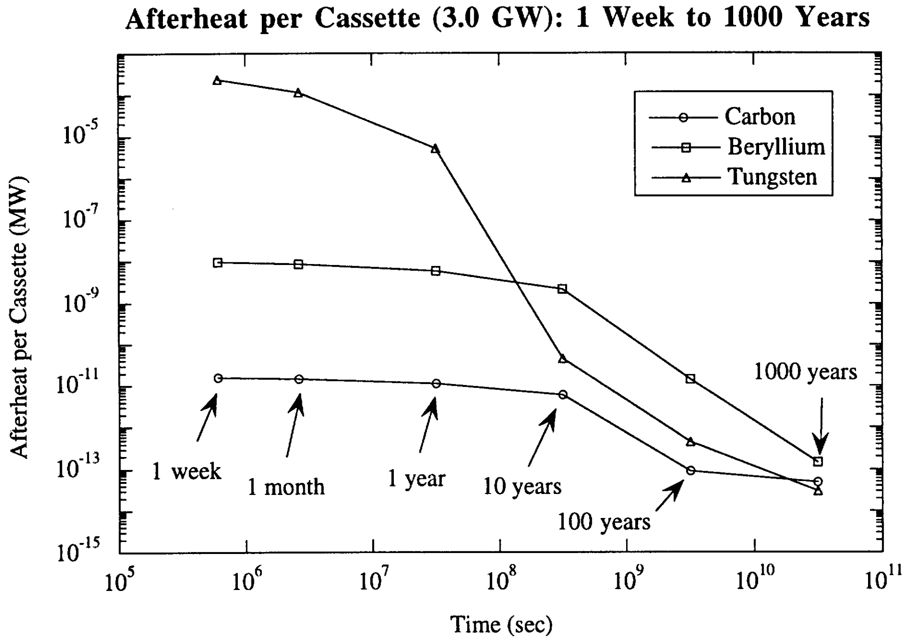

Figure 5.12: Afterheat of cassette under EPP operation from 1 week to 1000 years.

5.5 Heat Removal From Activated Cassettes

It can be seen from Figures 5.7 to 5.12 that considerable amounts of heat are expected to be internally generated due to activated products. Therefore, an area of concern is the temperature that can be reached by the armor due to the internal generation in the absence of active cooling. In this section the evolution of armor temperature as a function of time after shutdown will be investigated.

It is important to know what temperature is reached due to the internally generated heat so as avoid melting or sublimation which can be easily avoided through active cooling. Since it is prudent to leave the divertor cassette in the reactor for at least one week to decay down its activity, it can easily be cooled. Therefore, it would be interesting to know if it is necessary to use active cooling. The plates are in an interesting geometric configuration (Figure 2.6). Some of the plates are in contact with material on several sides, all have at least one surface open to vacuum. The evolution is the temperature of the armor due to internally generated heat can be modeled considering that the plates are insulated on 5 sides with only the "top" surface exposed to air. The equation that will give the evolution of the temperature is Equation (5-4).

This equation states that the energy storage (left hand side), is equal to the internally generated heat minus the loss of heat from radiation (right hand side).

$$\sum_i \left[\left(m_{b_i} c_{p_b} + m_{s_i} c_{p_s} \right) \frac{\partial T}{\partial t} = Q_{in}(t) - \varepsilon_n \sigma A \left(T^4(t) - T_\infty^4 \right) \right] \tag{5-4}$$

T is the temperature of interest and $m_b c_{pb}$ is the mass of the armor material multiplied by its specific heat, $m_s c_{ps}$ is the mass of the surrounding material multiplied by its specific heat, ε_n is the emissivity of the armor material, σ is the Stefan-Boltzmann constant, A is the area of the armor that is facing the vacuum, T is the temperature of the armor, and T_∞ is the temperature in the vacuum vessel.

However, in reality this is an extremely complicated problem. First, the sides are not truly insulated. The stainless steel support structure is also highly activated and there would be a second Q_{in} term. Also, many of the quantities in Equation 5-4 are temperature dependent, i.e. the specific heat and the emissivity. The evolution of the temperature in the vacuum vessel (T_∞) as a function of time is also not known. An accurate calculation will be complicated while based on many assumptions; therefore, a simple, highly conservative calculation will be done instead.

This calculation was done as follows. First, an average Q_{in} was calculated for the time period 1 day to 1 week from the curves in Figures 5.7 to 5.9. Now, Q_{in} is really a function of time but since it drops by several orders of magnitude in a matter of a few hours, it can be expected that it would be judicious to continue cooling the cassettes for this time period. Therefore, the average Q_{in} values for the time period 1 day to 1 week will be focused on. These values can be found in Table 5.3.

Table 5.3: Average Q_{in} (1 day to 1 week) for Armor

Carbon		Beryllium		Tungsten	
Operation	$\langle Q_{in} \rangle$ [MW]	Operation	$\langle Q_{in} \rangle$ [MW]	Operation	$\langle Q_{in} \rangle$ [MW]
7.9 MW	1×10^{-12}	7.9 MW	3×10^{-9}	7.9 MW	2×10^{-5}
1.5 GW	2×10^{-10}	1.5 GW	5×10^{-7}	1.5 GW	4×10^{-3}
3.0 GW	4×10^{-10}	3.0 GW	1×10^{-6}	3.0 GW	8×10^{-3}

The assumed geometry is a block of material, that is insulated on all sides, with internal heat generation. Therefore, the radiation loss term has been neglected. Using Equation (5-5), which is a modified version of Equation (5-4), where mc_p is the mass of the armor material multiplied by its specific heat, the temperature of the armor reached with a Q_{in} listed in Table 5.3 was determined.

$$mc_p \frac{\partial T}{\partial t} = Q_{in} \tag{5-5}$$

The values shown in Table 5.4 are for the *increase* in temperature, not the final temperature after a week. The final temperature requires knowledge of the initial values which are not determined here.

Table 5.4: Average Temperature Increase in Armor

Carbon		**Beryllium**		**Tungsten**	
Operation	ΔT (K)	Operation	ΔT (K)	Operation	ΔT (K)
7.9 MW	1.5×10^{-8}	7.9 MW	0.04	7.9 MW	22
1.5 GW (BPP)	3×10^{-6}	1.5 GW (BPP)	7	1.5 GW (BPP)	4400
3.0 GW (EPP)	5×10^{-6}	3.0 GW (EPP)	14	3.0 GW (EPP)	8700

It can clearly be seen that the increase in temperature for the carbon and beryllium is negligible. Therefore, since this is a very conservative calculation, it appears that the active cooling may not be necessary. However, the heat generation and the heat capacity of activated support structures has been neglected. This additional heat generation can be very large, and should be evaluated.

For tungsten, however, it can be clearly seen that there is a potential problem with the levels of internal heat generation. Evaluating the radiation term in Equation (5-4) at 1300K, it is found:

$$Power\_Radiated = \varepsilon\sigma T^4 A = 1.4 \times 10^{-2}\, MW \tag{5-6}$$

which is an order of magnitude greater than the Q_{in} for the BPP and EPP operation. The value for T_∞ is not clear, however, if T_∞ is ~ 300K, $\varepsilon\sigma T_\infty^4 A$ is negligible. Also, the dump targets actually face each other at an angle so view factors will have to be taken into account.

For the ohmic operation, the increase in temperature is negligible, however, this cannot be said of the BPP and EPP operation. Clearly active cooling will be needed, for it does not appear that the radiation would compensate for these increases in temperature. The surrounding structure will also be activated but steel should be activated to approximately the same order of magnitude as the tungsten.

5.6 Conclusions

In this chapter the neutron activation properties of the candidate materials were investigated. The three materials exhibited noticeably different behavior under the same neutron irradiation environment. Tungsten was shown to activate several orders of magnitude greater than the beryllium and carbon due to the neutron flux. From an activation standpoint, carbon clearly has the advantage. By increasing the purity of carbon (removing the iron) the long-term activity can be greatly reduced. There is a higher purity grade of IG-11 which is produced by Toyo Tanso, the IG-110 grade, so it is a feasible option. In the beryllium case, increasing the purity would help somewhat by the loss of the iron contribution; however, tritium is of greater concern for short terms. Since tritium is generated from the beryllium, it is not possible to decrease its concentration levels. In tungsten, it is the tungsten itself which is highly activated. Increasing the purity is of no great advantage. Therefore, since the very high purity grades of tungsten are very expensive, it may be possible to use less pure grades and save money without raising the level of concerns in the activation and afterheat area.

One point to note is that the volume of waste generated by the carbon is greater than that generated by the tungsten and beryllium, since the armor is much thicker. The levels of activation are a greater concern in the tungsten and beryllium, since these cassettes must be stored once they have been removed. However, it is interesting to note that in the very long term (1000 years) the tungsten has the lowest activity.

Tungsten also has a disadvantage of having to be actively cooled. The recommended turn-around time for the changing of a divertor cassette is < 8 weeks; therefore, any time delays incurred due to high activity levels may be unacceptable. Beryllium and carbon do not have this problem.

In conclusion, due to high activation levels, it appears that tungsten's use in a fusion reactor should be minimized. If activation were the sole basis for material selection, carbon would be the clear winner; however, the method for material selection is based on many criteria. Activation is one attribute of many that be weighed in engineering design decisions.

CHAPTER 6

It ain't over, 'til it's over.
Yogi Berra

Summary and Future Work

6.1 Displacement Damage

In this study it was shown that carbon and beryllium incur high levels of displacements damage under Basic Performance Phase (BPP) operation of ITER. Due to its large nuclear mass, tungsten does not suffer significantly from displacement damage. IG-11 graphite was shown to have a sharp loss of its thermal conductivity which affects its usefulness as a thick armor material. In fact, it was shown that an average temperature of 500°C, IG-11 armor would be limited to a thickness of 16.8 mm which leads to a shortened lifetime. The dpa's were calculated for the beryllium armor. However, due to the lack of data on modern grades of beryllium, it was nearly impossible to extrapolate the results. However, when data on the effect of neutron irradiation on modern grades are available, these results can be used to predict the changes in the material properties. Helium generation, and hence related stresses, were found to be insignificant.

6.2 Activation

The activity per cassette for each of the candidate materials under ohmic, BPP and Enhanced Performance Phase (EPP) operation were calculated using DKR-PULSAR. It was shown that tungsten is highly activated under all operation scenarios. At shutdown, the activity under BPP operation was found to be ~4 x 10^6 Ci. This is an extremely high level of activity. Even after 1 week, the activity has only decreased to 10^5 Ci. A sharp decrease in activity is seen after one month past shutdown. In fact it takes several years for the activity in tungsten to reach the activity of beryllium at one week.

For beryllium the internal generation of tritium is of large concern for the long-term activity. Since a BeO oxide layer is formed on the surface of the beryllium, most of the tritium will be trapped internally. If there existed some method of removing this layer and forcing the tritium to diffuse out, the activity would be much reduced.

Carbon is the least activated of the materials. Since the majority of the long-term activity is due to the iron impurities, purer grades of IG-11, namely IG-110, may perform better as far as activation is concerned.

6.3 Recommendation for Armor Materials

From the study in Chapter 4, it is clear that tungsten is the least affected by neutron damage and sputtering. However, it is clearly shown in Chapter 5 that the tungsten is the most highly activated material out of the three candidate materials. Therefore, its use as an armor should be minimized from a safety viewpoint. Tungsten's use should be restricted to the dome under BPP and EPP operation. This recommendation is based on the fact that tungsten withstands sputtering much better than beryllium and graphite and if it is restricted to the dome only, the volume of radioactive waste is reduced. This would decrease the volume of activated tungsten generated by 61% if used on the dome only as opposed to being used on the dome and the dump targets. While the atomic number of tungsten is high, its lack of sputtering should keep tungsten impurities in the plasma at a minimum. If carbon and beryllium were used, the plasma would contain many more impurities, albeit those with lower Z. Under ohmic operation, there is no need to utilize tungsten since the particle fluxes will be much lower; sputtering should not be severe for the carbon and beryllium.

While graphite loses thermal conductivity under neutron irradiation, it still has better sputtering resistance than beryllium due to its higher atomic mass. Also, it is more abundant, and it activates much less. Therefore, it is recommended that under ohmic operation, graphite be used for the dome and the dump targets. The only concern is the loss of tritium through co-deposition. However, it may be possible to still use graphite as the dump targets in BPP operation.

Beryllium utilization has been shown to be extremely limited by sputtering; however, a 1 cm plate can still last the 1000 pulses which is the minimum lifetime requirement for the divertor. It is unclear how the beryllium is mechanically affected by neutron irradiation due to the lack of experimental data on modern grades of beryllium. However, there will hopefully be results at some point on S-200E grade which is quite similar to the S-65 grade which has been the focus of this study. There may also be problems with swelling due to helium and hydrogenic atom formation in beryllium. However, tritium is not lost through co-deposition as with graphite. Still, beryllium is not too abundant and needs to be used in other places in the reactor.

Therefore, it is recommended that beryllium be used as dump target material in the EPP operation, and if necessary, BPP operation.

Table 6.1: Recommendations for Material Selection

Operation	Dome	Energy Dump Targets
Ohmic	carbon	carbon
BPP	tungsten	carbon or beryllium
EPP	tungsten	beryllium

6.4 Future Work

There are several issues which were only alluded to in this work which merit study. One area that should be investigated is the amount of tritium co-deposited with the graphite. While the graphite is not highly activated itself, if large amounts of tritium are co-deposited, the activity of the cassette could actually be much higher (approaching beryllium levels). Another issue that could be investigated is the correlation of the beryllium dpa's with the modern grades (S-200E) of irradiated beryllium assuming the samples are characterized. Also, the heat transfer calculations could be made more realistic. It would interesting to do a two-dimensional analysis of the effects of neutron irradiation of thermal conductivity and heat removal. Finally, it would be of interest to run a code that gives final composition of materials. This is specifically of interest for the tungsten, since the DBTT is composition dependent. If the final composition is known; it may be possible to predict the shift in the DBTT.

APPENDIX A

MCNP Model

A.1 Introduction

The basic input file of the TAC-4 geometry was created by M.E. Sawan at the University of Wisconsin - Madison [34] and modified by the author for this study. The input file a sample of which is included in the appendix, consists of the following components: a cell card, and surface card and data cards. The cell cards define the geometry and the material density of the component in question. The surface cards define the boundaries of the cells. The data cards specify the material specify the material composition for the cell, the source particles, and the desired output data.

The structure of the MCNP data file consists of one blank line between each card[33]. A one line title card is used in the beginning to identify to input file. Therefore the structure is as follows:

Title Card
Cell Cards
Blank Line Delimiter
Surface Cards
Blank Line Delimiter
Data Cards
Blank Line Delimiter (optional)

Figure A.1: Outline of MCNP input file

A.2 Cell Card

The specific format of a cell card is as indicated by the general form:

n **m** ρ **geom** **params**

where

n = unique cell number, in column 1-5, integer between 1 and 99999

m = material number, zero if cell is a void, integer between 1 and 99999

ρ = cell material density

No entry for void cell

positive entry = atom density (at/b-cm)

negative entry = mass density (gm/cm^3)

geom = list of surface numbers with appropriate sense and boolean operators specifying the cell

params = optional cell parameters

Cell parameters that can be specified in the params section are cell importance, temperature or volume.

A.3 Surface Card

The specific format of a surface card is as follows:

i **a** **list**

where

i = unique surface number, in columns 1-5, integer between 1 and 99999

a = surface mnemonic

list = parameters that describe the surface **a** (dimensions, center, radius, etc.); all units in centimeters

For example, if a surface is a general plane (P) the following equation is used:

$$Ax + By + Cz - D = 0 \tag{A-1}$$

The input line if this were surface 1 would then consist of :

1 P ABCD

For more complicated geometries, the item under list vary. See the MCNP manual for more explanation.

A.4 Data Card

A.4.1 Material Definition

The data card is of very different form than the other two cards. The general format is as follows:

m# **ZAID$_1$** **fraction$_1$** **ZAID$_2$** **fraction$_2$** **......**

where

m# = material card (m), # is material number, start in columns 1-5, integer between 1 and 99999

ZAID = cross section identifier from XSDIR file

fraction = nuclide fraction

if positive, the atom fraction
if negative, then weight fraction

In the definition of the material cards for the input file, the following materials were used (along with their ZAID identifier).

Material 1 is natural beryllium (4009.50c)
Material 2 is natural tungsten (74000.55c)
Material 3 is natural carbon (6000.50c)
Material 4 is natural copper (29000.50c)
Material 5 is natural lead (82000.50c)
Material 6 is 316LN stainless steel. The composition of which was taken from [41] The composition is:

Table A.1: Composition of 316-LN

Element	Fe	Cr	Ni	Mo	Mn
Weight %	66.9%	17%	12%	2.5%	1.6%
ZAID	26000.55c	24000.50c	28000.50c	42000.50c	25055.50c

Material 7 is Inconel 600. The composition was taken from[42]. The composition is:

Table A.2: Composition of Inconel 600

Element	Ni	Cr	Fe
Weight %	76%	16%	8%
ZAID	28000.50c	24000.50c	26000.55c

Material 9 is copper stabilized Nb3Sn. The ratio selected was 50:50 Cu:Nb3Sn. The composition is:

Table A.3: Composition of Copper Stabilized Nb3Sn

Element	Nb	Sn	Cu
Weight %	37.5%	12.5%	50%
ZAID	41093.50c	50120.35c	29000.50c

A.4.2 Source Definition

The generation of a source was a bit difficult for this geometry since MCNP does not have a toroidal source option. Therefore, the following definition was done to approximate a toroidal source. A cell 10000 was defined as a void torus 1 m in diameter. This cell is the plasma. A cylindrical source was placed such that it completely encompassed the plasma. (Figure A.2) An isotropic source was defined in the cylinder, but it was restricted to cell 10000. Therefore, only the histories of neutrons that are born in the cylinder *which are also in cell 10000* are followed - all others are killed. Therefore, a toroidal source has been approximated. The reactor was modeled under both DT and DD operation; therefore, two input files were created for each of the materials. The purpose was to model both DT and DD operation. Under DT operation, the neutron spectrum was assumed to be 99% neutrons of energy 13.8 to 14.2 MeV and 1% neutrons of energy 2.4 to 2.5 MeV. The lower energy neutrons are there to account for any DD reactions. The source for the DD operation is simply 100% neutron of energy 2.4 to 2.5 MeV.

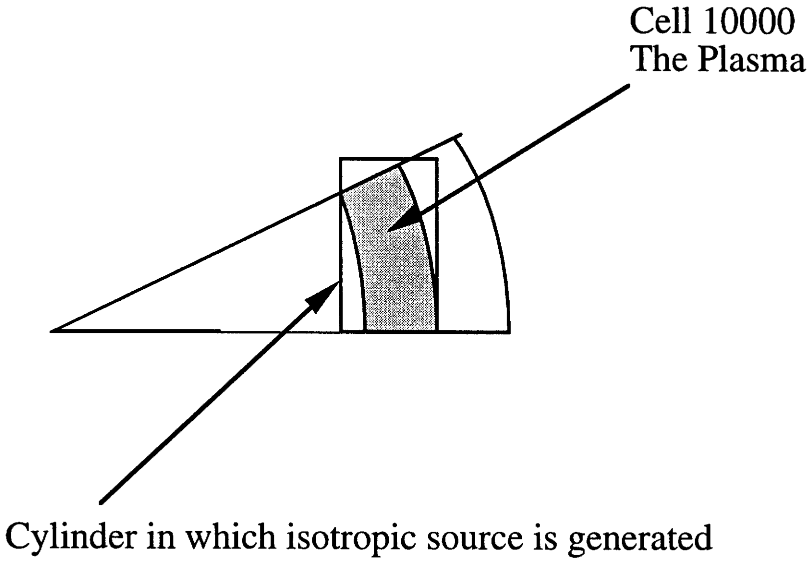

Figure A.2: Source definition for the input file.

A.4.3 Tallies

The particles launched in this model were all neutrons and MCNP provides seven standard neutron tallies. Only two types of neutron tallies were used in this study.

Table A.4: Tallies

Tally Mnemonic	Description	Fn units
F2:n	Flux averaged over a surface	particles/cm^2
F4:n	Flux averaged over a cell	particles/cm^2

The tallies that were used in this study are the type 2 and type 4 tallies (see Table A.4). A type 2 tally which has the mnemonic F2:n is the neutron flux averaged over a surface in units of particles/cm^2. The type 4 tally which has the mnemonic F4:n is the neutron flux averaged over a cell in units of particles/cm^2. The F2:n tally requires a surface area. The F4:n tally requires the volume. In this geometry, the surface areas and volumes were calculated from blueprints which can be found in Chapter 2. The neutron flux was also divided into 46 energy bins. This was done since the displacement and helium generation cross sections that were supplied were separated into 46 bins, since they were from the ENDF/B-V data files. Also, the required input data for the DKR-PULSAR runs were a 46 energy bin format. The 46 energy bins in units of MeV are as follows.(Table A.5) The numbers listed are the higher end energies for each bin.

Table A.5: Energy bins for ENDF/B-V Cross Sections (MeV)

4.14e-7	8.76e-7	1.86e-6	3.93e-6	8.32e-6	1.76e-5	3.73e-5
7.89e-5	1.67e-4	3.54e-4	7.48e-4	1.58e-3	3.35e-3	7.1e-3
1.5e-2	3.18e-2	6.74e-2	1.23e-1	0.166	0.224	0.302
0.408	0.55	0.743	1.0	1.35	1.83	2.47
2.73	3.01	3.33	3.68	4.07	4.49	4.97
5.49	6.07	6.7	7.41	8.19	9.05	10
11.05	12.2	13.5	14.2			

The type 2 tallies were unmodified and were used to determine the neutron wall loading on the armor. Also, this tally generated the input data for the DKR-PULSAR code. The type 4 tally was modified by energy multiplier cards. In all cases, the type four tallies were divided into 46 energy bins and multiplied by the corresponding displacement cross section for that energy bin. The plot of the displacement cross sections can be found in Chapter 4, Figure 4.1. In the case of beryllium, and second type 4 tally was taken and modified by a energy multiplier card that is the total helium generation. The plot of the helium generation cross section versus energy can also be found in Chapter 4, Figure 4.2.

A.4.5 Temperature

The temperature of the reactor components was also entered into the input file. As exact numbers were not known, a best guess was made. The inboard blanket segment, the outboard blanket segment, and the vacuum vessel were assumed to be at 400°C. All voids are automatically set to room temperature. The copper heat sinks for the divertor armor was assumed to be at 300°C. The carbon and tungsten armor was assumed to be at 1000°C, the beryllium armor was assumed to be at 600°C. The toroidal field coil structure was assumed to be at 100°C. The outside world was assumed to room temperature.

A.5 MCNP Geometry

In MCNP, geometric cells are volume elements bounded by first-, second- and fourth-order surfaces. These correspond to planes, the nine quadratic surfaces, and elliptical tori. Due to the ITER geometry the tori are used extensively in the input file generation. In general, the geometry of this input file is that a full 3 dimensional model of ITER is entered. A slice is then taken on the torus and reflecting boundary conditions are put in so as to model a periodic structure. The slice in the model for this work is 1.875°. The corresponds to one half a divertor cassette. In the TAC-4 design there are 96 divertor cassettes. Figure A.3 shows a vertical cross section of the MCNP model. Figure A.4 to A.7 show close-ups of the divertor region with the armor for the dome and dump targets shown. The numbers in the figures refer to the cell numbers. In Figure A.5, cells 1216 and 1226 are the upper inner dump target and the lower inner dump target respectively. Cell 206 is the copper heat sink. In Figure A.6, cell 1204 is the dome armor and cell 204 is the copper heat sink. In Figure A.7, cells 1213 and 1223 are the lower outer dump plate and the upper outer dump plate respectively. Cells 203, 1206 and 1203 are the copper dump targets.

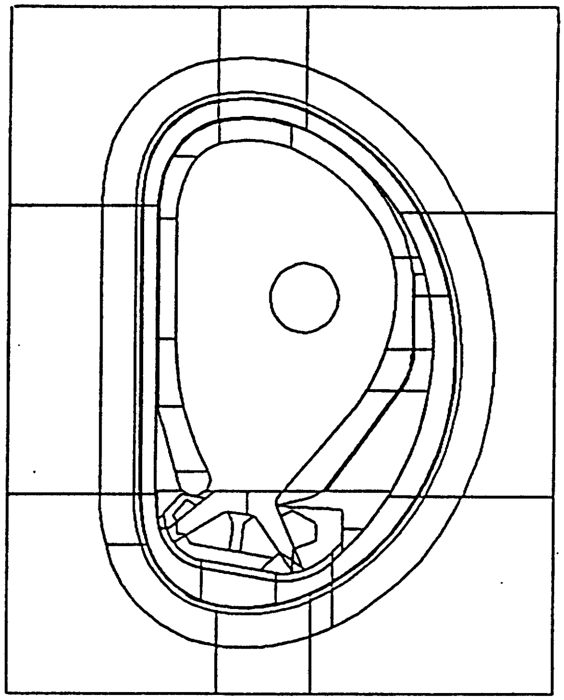

Figure A.3 Vertical Cross Section of the Reactor

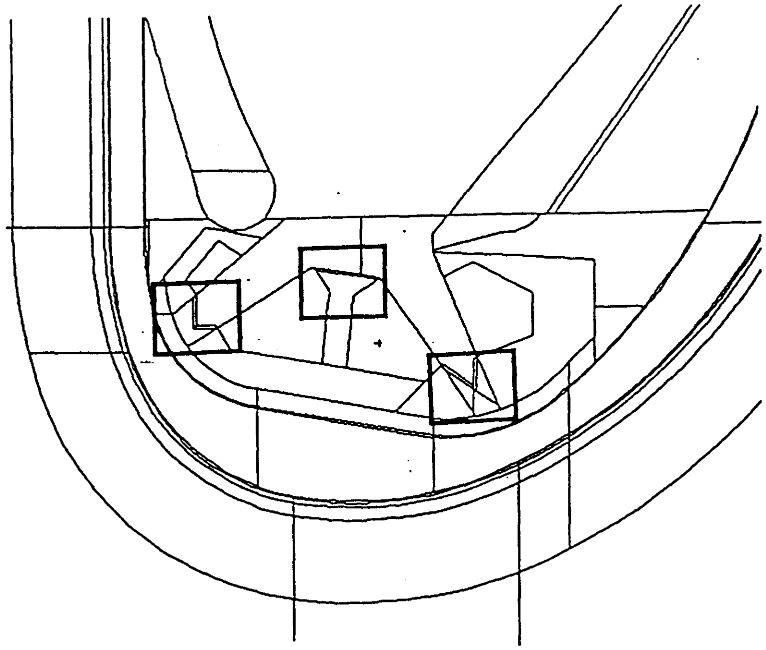

Figure A.4 Close up of Divertor Region

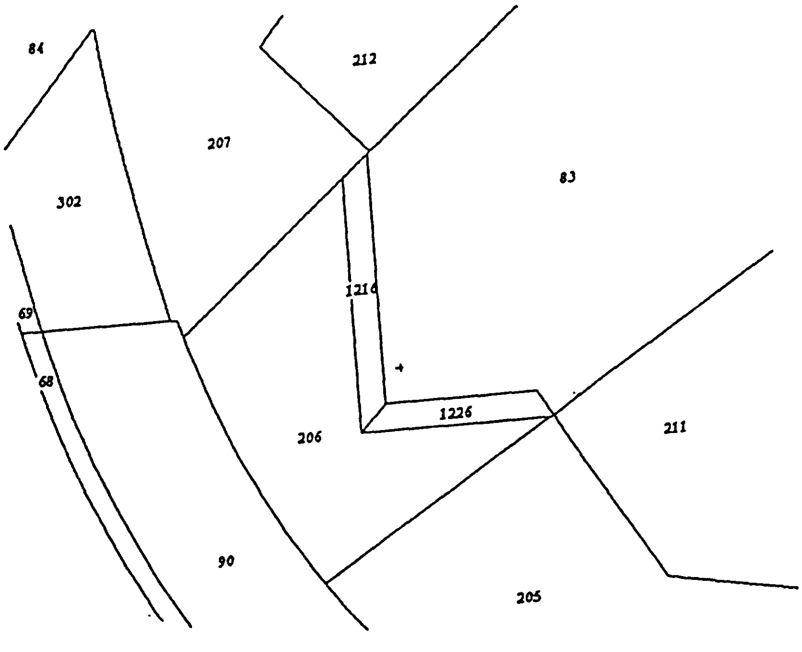

Figure A.5 Inner Dump Target

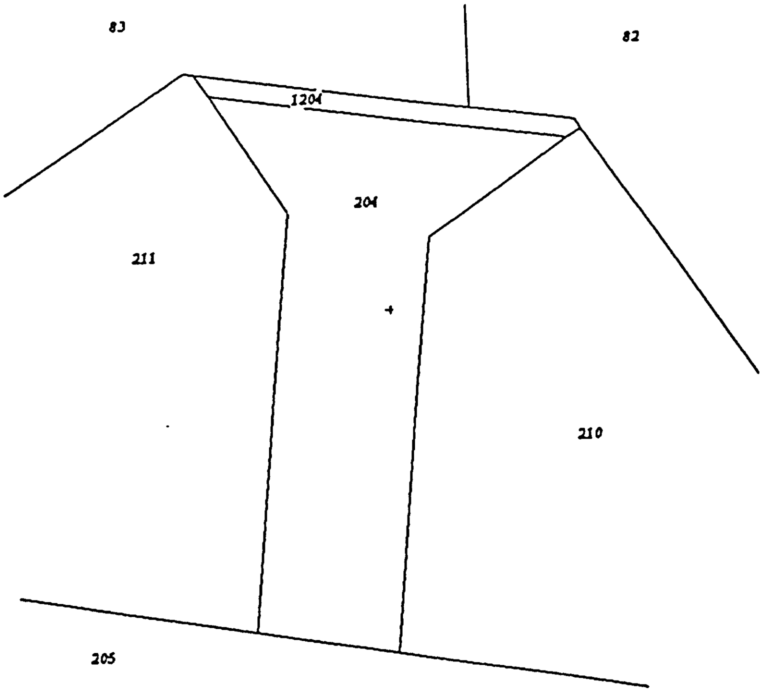

Figure A.6 Dome Armor

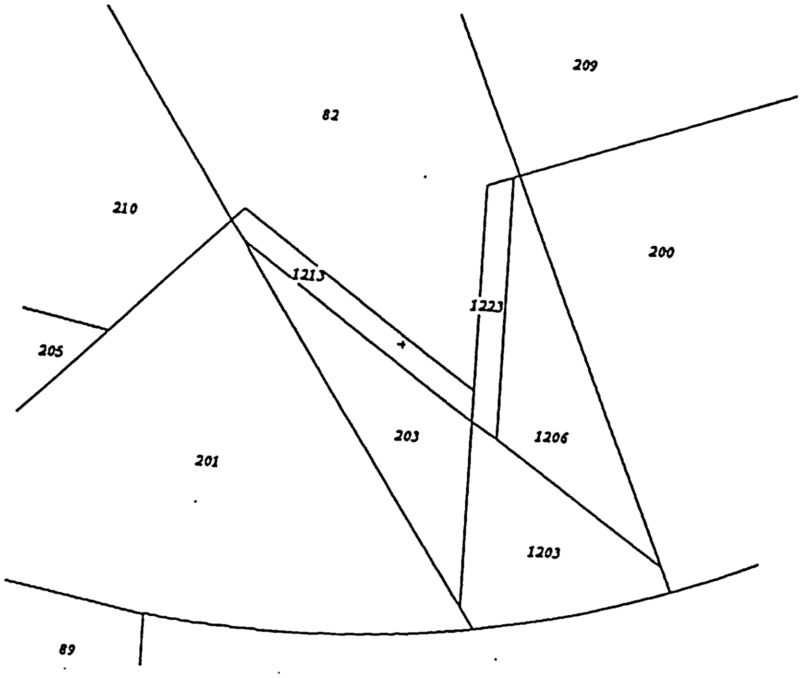

Figure A.7 Outer Dump Target

A.6 Sample Input File

Included in this section is a sample input file - one of the six used in this study. This specific input file is for beryllium armor plating under DT operation. It includes both the displacement and the helium generation tallies.

```
 iter 3d global model with half divertor cassette design as of Nov 1994
c       toroidal sector (1.875 degrees)
c  armor plating is made of Beryllium (1 cm)
c      ----------------------------------------------------------------
c      |    -------->         cell definitions      <------------    |
c      ----------------------------------------------------------------
c                ---------------------
c                |   plasma chamber  |
c                ---------------------
    1  0     (360  321  -43   1  -302 : -2   -43  302   -306   :
                     3  -43  306 -307 : -4   -43  307   -309   :
                    -5       309  -41 : -6   -43   41    309   :
                    -6   43  309  -45 : -7    45  309          :
                    -7   43  314 -309 : -8    43  315   -314   :
                    -9   43  399 -315 : -10   43  320   -399   :
                   -11   43  321 -320) 400 420 10000
c
c         --------------------------
c         |      plasma            |
c         --------------------------
    10000 0 -10000 400 420 $inside plasma
c          ------------------------------
c          |   inboard blanket segment   |
c          ------------------------------
c     ---> bottom part
    2  6 -7.86    (-1  -301 :  (51  -360  : -1  360) 301 -302) 400 420
c      be-coating
    3  1 -1.85 2 -22    302    -306  -43 400 420
c      cu-layer
    4  4 -8.96            22 -842    302   -306   -43 400 420
c      shielding blanket
    5  6 -7.86          (842  51 302  -303  :
                  842   -305  303   -52) -43 400 420
    6  6 -7.86  54      842  305  -306  -43 400 420
c     ---> central part
c      be-coating
    7  1 -1.85  -3   23   306  -307 400 420
c      cu-layer
    8  4 -8.96           -23  843   306  -307 400 420
c      shielding blanket
    9  6 -7.86         -843  54   306  -307 400 420
c     ---> upper part
c      be-coating
   10  1 -1.85 4  -24   307  -309  -43 400 420
   11  1 -1.85 5  -25   309   -41  -43 400 420
c      cu-layer
   12  4 -8.96      24  -844   307  -309  -43 400 420
   13  4 -8.96      25  -845   309   -41  -43 400 420
c      shielding blanket
   14  6 -7.86    (844  54  307  -308 :
                    844 -55  308  -309 : 845  -55  309  -310) -43
                 400 420
   15  6 -7.86   845  -56  310   -41 400 420
c      be-coating
   16  1 -1.85      6  -26   41   -45 310 400 420
c      cu-layer
   17  4 -8.96    26  -846   41   -45 310 400 420
c      shielding blanket
   18  6 -7.86   846  -57   41   -45 310 400 420
c     -------------------------------
```

```
c    |   outboard blanket segment    |
c    --------------------------------
c    ---> upper part
c      be-coating
   19  1 -1.85       7  -27   45   314  43 400 420
   20  1 -1.85       8  -28  315  -314  43 400 420
   21  1 -1.85       9  -29  316  -315  43 400 420
c      cu-layer
   22  4 -8.96      27  -847   45   314  43 400 420
   23  4 -8.96      28  -848  315  -314  43 400 420
   24  4 -8.96      29  -849  316  -315  43 400 420
c      shielding blanket
   25  6 -7.86    (847  -58   45   312  : 847  -59  314  -312  :
                      848  -59  315  -314  :
                      849  -59  316  -315) 43 400 420
c    ---> bottom part
c      be-coating
   26  1 -1.85      9  -29  399  -316                    43 400 420
   27  1 -1.85     10  -30  320  -399                    43 400 420
   28  1 -1.85     11  -31  321  -320                    43 400 420
c      cu-layer
   29  4 -8.96     29  -849  399  -316                   43 400 420
   30  4 -8.96     30  -850  320  -399                   43 400 420
   31  4 -8.96     31  -871  321  -320                   43 400 420
c      shielding blanket
   32  6 -7.86   (849  -60  317  -316  : 849  -61  399  -317  :
                     850  -61  318  -399)  43 400 420
   33  6 -7.86   850  -63  319  -318       43 400 420
   34  6 -7.86  (850  -65  320  -319 :  871 -65  321  -320)  43
            400 420
   35  6 -7.86   (-67 47  : -47 355 11 -323) -321   43 400 420
c    ---> back plate lower ob-segment
   36  6 -7.86    61  -62  318  -317 400 420
   37  6 -7.86    63  -64  319  -318  50 400 420
   38  6 -7.86    65  -66  321  -319 400 420
c    ----------------------------
c    |  vacuum vessel inboard   |
c    ----------------------------
c    ---> central part
   39  7 -8.9       341  -342  -101  151 400 420
   40  7 -8.9    341  -342  -151  201 400 420
   41  7 -8.9       341  -342  -201  251 400 420
c      lead shield
   42  5 -11.4      341  -342  -251  271 400 420
c    ---> upper part
   43  7 -8.9 (342  -344   102 -152 : 344  103 -153) -351 400 420
   44  7 -8.9  351  -352   104 -154   345 400 420
   45  7 -8.9  (342  -343   152 -202    : 343  -344  152 -203   :
                     344  153 -203) -351 400 420
   46  7 -8.9   351  -352   154 -204 345 400 420
   47  7 -8.9        (342  -343   202 -252  : 343   203 -253)  -351
            400 420
   48  7 -8.9       351  -352   204 -254   345 400 420
c      lead shield
   49  5 -11.4      (342  -343   252 -272  : 343   253 -273)  -351
            400 420
   50  5 -11.4     351  -352   254 -274   345 400 420
c    ----------------------------
c    |  vacuum vessel outboard  |
c    ----------------------------
```

```
c    ---> upper  part
   51  7 -8.9    346   105 -155      352 400 420
   52  7 -8.9 346   155 -205         352 400 420
   53  7 -8.9    346   205 -255      352 400 420
c      lead shield
   54  5 -11.4   346   255 -275       352 400 420
   55  5 -11.4   -346  347  105  -155 352 400 420
   56  5 -11.4   -346 347  155  -206   352 400 420
   57  5 -11.4   -346 347  206  -256  352 400 420
c      lead shield
   58  5 -11.4   -346  347  256  -276  352 400 420
c    ---> central part
   59  7 -8.9    -347   357   106  -156 400 420
   60  7 -8.9 -347  348    156  -206      357 400 420
   61  7 -8.9    -347   348   206  -256   357 400 420
c      lead shield
   62  5 -11.4   -347   348   256  -276    357 400 420
   63  5 -11.4                 -348  156  -207   357 400 420
   64  5 -11.4                 -348  207  -257   357 400 420
c      lead shield
   65  5 -11.4                 -348  257  -277   357 400 420
c    ---> bottom part
   66  7 -8.9       -357   355   107  -157  -349 400 420
   67  7 -8.9       -355   353  -108   158 400 420
   68  7 -8.9    -353  -350   109  -159 400 420
   69  7 -8.9    350  -341   110  -160 -353 400 420
   70  7 -8.9 (-357   356   157  -207   : -356  355  157  -208) -349
          400 420
   71  7 -8.9 (-355   354  -208  -158   : 353  -354 -209  -158)
          400 420
   72  7 -8.9  (-349   159  -209  : 349  -350 -210   159   :
                     350  -341   160  -210)  -353 400 420
   73  7 -8.9   -357   356   207  -257   -349 400 420
   74  7 -8.9   -356   354   208  -258   -349 400 420
   75  7 -8.9   -354         209  -259   -349 400 420
   76  7 -8.9    349 -341    210  -260   -353 400 420
c      lead shield
   77  5 -11.4  -357   356   257  -277   -349 400 420
   78  5 -11.4  -356   354   258  -278   -349 400 420
   79  5 -11.4  -354         259  -279   -349 400 420
   80  5 -11.4   349 -341    260  -280   -353 400 420
c         -----------------------------------------------------
c         |   void between blanket segments and vacuum vessel |
c         -----------------------------------------------------
c    ---> bottom part ( divertor present)
   81  0      -321 355 621 -106 350 (622:623) ((67 47):(323 -47))
              400 420
   82  0      43 -321 (-355:-11:-621) (618:619) (-625:-620) (-627:626)
              400 420
   83  0      -321 (616:614) (628:629) -43 (618:-617) 615 400 420
   84  0      -321 54 -615 1 (613:-612) -110 400 420
   85  0       -110  -54  -341  350 400 420
   86  0       341  -321   101 -54 400 420
   87  0      -350 -106 47 623 400 420
   88  0      -357 355 -350 607 -107 400 420
   89  0       -355 353 108 -608 400 420
   90  0        -353 -350 -109 609 400 420
  301  0       357 -623 -106 606 -350 400 420
  302  0      350 612 610 -43 -110 400 420
c    ---> inboard void gap
```

```
   91  0      ( -301  321  1  101  -360 : 301  101  -51  -303  :
                303 -305  101  52 -360) 400 420
   92  0        305  -308 -54   101 400 420
   93  0        308  -342  55   101  -3 400 420
   94  0        342  -310  55  -102  -3 400 420
   95  0        310  -344  56  -102  -3 400 420
   96  0        344  -351  56  -103 400 420
c    ---> upper void gap
   97  0       (351  -41   56 -104  :   41   -45  57  -104   :
                 45 -352   58 -104  :  352        58  -105)  312
                 400 420
c    ---> outboard void gap
   98  0       -312  316   59  -105   47 400 420
   99  0       -316  317   60  -105   47 400 420
  100  0       -317  347   62  -105   47 400 420
  101  0       -347  318   62  -106   47 400 420
  102  0       -318  319   64  -106   47 400 420
  103  0       -319  321   66  -106   47 400 420
c
c      ----------------------------------------
c      !       divertor cells                 !
c      ----------------------------------------
c
c        ------> outer leg (pumping slots included)
c
  200  6 -7.86       355 -622 621 -623 ((-620(-631:632:624)):(-357 -607 620):
                 (357 -606 620)) 400 420 #213 #214
c       ------> outer dump plate
c  203  1 -1.85   619 -621 -607 ((625 620):(-625 -626 627))
c                 400 420 #213 #214 #215 #216
   203  4 -8.96  -625 -1004 619 627
                 400 420 #213 #214 #215 #216 $Cu Heat sink
   1203 4 -8.96  625 -1004 -607 -621 619
                 400 420 #213 #214 #215 #216 $Cu Heat sink
   1206 4 -8.96  1005 1004 -621 620
                 400 420 #213 #214 #215 #216 $Cu Heat sink
   1213  1 -1.85  -626 -625 1004 619 627
                 400 420 #213 #214 #215 #216  $ lower outer dump plate
   1223  1 -1.85  1004 625 -1005 620
                 400 420 #213 #214 #215 #216 $ upper outer dump plate
c       ------> middle leg
   204  1 -1.85  -1007 633 617 -619 (635:662) (-634:-661)
                    400 420 #219 #220   $ Cu Heat Sink for Dome
  1204  1 -1.85 1007 -618 -619 -661 662
                 400 420 #219 #220   $Dome Armor
  205  6 -7.86        -627 617 (-633:-629) (353 608:-353 -609)
                 400 420
                (-649:648:-640:639) (-649:648:-642:641)
                (-651:650:-640:639) (-651:650:-642:641)
                (-653:652:-640:639) (-653:652:-642:641)
                (-655:654:-640:639) (-655:654:-642:641)
  201  6 -7.86        627 -619 (608 -355:355 -607) 400 420 #215 #216
c       ------> inner dump plate
c  206  1 -1.85   -617 615 -614 -629 (-616:-628)  -609
c                 400 420 #223 #224 #225 #226
   206  4 -8.96  -617 615 (-1001:-1002) -609 -629
                 400 420 #223 #224 #225 #226  $Cu Heat sink
  1216  1 -1.85  1001 -616 -1003 615
                  400 420 #223 #224 #225 #226  $ upper inner dump plate
  1226  1 -1.85   1003 -628 1002 -617 -629
```

```
                400 420 #223 #224 #225 #226 $ lower inner dump plate
c       ------> inner leg
  207  6 -7.86   -615 612 (-610 350: -609 -350) -613 (-614:-636:637)
               400 420 #225 #226
c       ------> cells for div fins and their support structure
  209  6 -7.86        355 631 -632 -620 621 -624 400 420
  210  6 -7.86        -618 -619 633 -627 634 661 400 420
  211  6 -7.86        -618 -635 633 617 629 -662 400 420
  212  6 -7.86        -637 614 -615 636 400 420
c       -------> cells for pumping slots (2 per 7.5 degree sector)
c         at outer dump plate
  213  6 -7.86 645 -644 625 -607 -357 640 -639 400 420
  214  6 -7.86 645 -644 625 -607 -357 642 -641 400 420
  215  6 -7.86  627 -626 -607 647 -646 640 -639 400 420
  216  6 -7.86 27 -626 -607 647 -646 642 -641 400 420
c         at  middle leg
  217  6 -7.86 -633 608 649 -648 640 -639 400 420
  218  6 -7.86 -633 608 649 -648 642 -641 400 420
  219  6 -7.86 -618 608 651 -650 640 -639 400 420
  220  6 -7.86 -618 608 651 -650 642 -641 400 420
  221  6 -7.86 -633 608 653 -652 640 -639 400 420
  222  6 -7.86 -633 608 653 -652 642 -641 400 420
c         at inner dump plate
  223  6 -7.86 -628 -629 655 -609 -654 640 -639 400 420
  224  6 -7.86 -628 -629 655 -609 -654 642 -641 400 420
  225  6 -7.86 -616 656 -657 -609 640 -639 400 420
  226  6 -7.86 -616 656 -657 -609 642 -641 400 420
c    ---------------------------------------------
c    |   gap between pb back shield and TF coil   |
c    ---------------------------------------------
c    ---> inboard region
  401  0       341  -342  -271  281 400 420
  402  0       (342  -343   272 -282  : 343   273 -283)  -351
               400 420
  403  0      351  -352   274 -284   345 400 420
c    ---> outboard region
  404  0   346   275 -285       352 400 420
  405  0                  -346  348  276  -286  352 400 420
c    ---> divertor region
  406  0                  -348  277  -287   357 400 420
  407  0  -357   356   277  -287   -349 400 420
  408  0  -356   354   278  -288   -349 400 420
  409  0  -354         279  -289   -349 400 420
  410  0   349 -341    280  -290   -353 400 420
c    ----------------------------------------------------
c    !   TF coils. half a coil modeled                   !
c    ----------------------------------------------------
c    ---> inboard region
  411  8 -8.96     341  -342  -281  291 -435 400 420
  412  8 -8.96     (342  -343   282 -292  : 343   283 -293)  -351
               -435 400 420
  413  8 -8.96    351  -352   284 -294   345 -435 400 420
c    ---> outboard region
  414  8 -8.96  346   285 -295         352 -435 400 420
  415  8 -8.96       -346  348  286  -296  352 -435 400 420
c    ---> divertor region
  416  8 -8.96             -348  287  -297   357 -435 400 420
  417  8 -8.96 -357   356   287  -297   -349 -435 400 420
  418  8 -8.96 -356   354   288  -298   -349 -435 400 420
  419  8 -8.96 -354         289  -299   -349 -435 400 420
```

```
  420  8 -8.96  349 -341    290  -300   -353 -435 400 420
c    ----------------------------------------------------------
c    ! toroidal space between TF coils. half a coil modeled  !
c    ----------------------------------------------------------
c    ---> inboard region
  421  0      341  -342  -281  291 435 400 420
  422  0      (342  -343   282 -292  : 343   283 -293)  -351
              435 400 420
  423  0     351  -352   284 -294   345 435 400 420
c    ---> outboard region
  424  0   346   285 -295          352 435 400 420
  425  0        -346  348  286  -296  352 435 400 420
c    ---> divertor region
  426  0              -348  287  -297   357 435 400 420
  427  0  -357   356   287  -297   -349 435 400 420
  428  0  -356   354   288  -298   -349 435 400 420
  429  0  -354         289  -299   -349 435 400 420
  430  0   349 -341    290  -300   -353 435 400 420
c                --------------------
c               |   outside world    |
c                --------------------
  104  0         341  -342  -291 400 420
  105  0        (-341   349  300  -353 : -349  -354  299  933)
                 400 420
  106  0        -933 400 420
  107  0         (342  -343  292  -353 :  343   -351  293 -936)
                 400 420
  108  0         936 400 420
  109  0        -936   351 -352  294  345 400 420
  110  0        -936   352  295  346 -935 400 420
  111  0        -346   348  296  357 -935 400 420
  112  0        -348   356  297      -935  933 400 420
  113  0        -356   354  298 -349       933 400 420
  114  0         935  -936  933 400 420
  115  0         -400 : -420
c      -----------------------------------------------------------
c      |   -------->    end of cell definitions    <------------    |
c      -----------------------------------------------------------

c      -----------------------------------------------------------
c      |   -------->      surface definitions     <------------    |
c      -----------------------------------------------------------
c    ----------------
c    | plasma       |
c    ----------------
   10000 tz 0 0 162.2 863.3 100 100
c     ---------------------------------
c     |   first wall contour ib --> ob   |
c     ---------------------------------
     1 tz 0 0 -366.62  548.2      47.39  47.39
     2 tz 0 0   41.51  1291.05  800.   800.
     3 cz 491.05
     4 tz 0 0  391.69  791.05   300.   300.
     5 tz 0 0  473.71  652.76   139.21 139.21
     6 tz 0 0  283.7   695.5     334.  334.
     7 tz 0 0   66.89  597.66   571.86 571.86
     8 tz 0 0  214.15  826.19   300.   300.
     9 tz 0 0  181.28  731.74   400.   400.
    10 tz 0 0  202.19  542.9    590.   590.
    11 kz -1337.919  0.7345  1
```

```
c
c    ------------------------------------
c    |   first wall: be-coating 8mm      |
c    ------------------------------------
c
   22 tz 0 0   41.51  1291.05  800.8  800.8
   23 cz 490.25
   24 tz 0 0  391.69  791.05   300.8  300.8
   25 tz 0 0  473.71  652.76   140.01 140.01
   26 tz 0 0  283.7   695.5     334.8 334.8
   27 tz 0 0   66.89  597.66   572.66 572.66
   28 tz 0 0  214.15  826.19   300.8  300.8
   29 tz 0 0  181.28  731.74   400.8  400.8
   30 tz 0 0  202.19  542.9    590.8  590.8
   31 kz -1339.148  0.7345  1
c
c    ------------------------------------
c    |   first wall: cu-layer 5 mm       |
c    ------------------------------------
c
  842 tz 0 0   41.51  1291.05  801.3  801.3
  843 cz 489.75
  844 tz 0 0  391.69  791.05   301.3  301.3
  845 tz 0 0  473.71  652.76   140.51 140.51
  846 tz 0 0  283.7   695.5     335.3 335.3
  847 tz 0 0   66.89  597.66   573.16 573.16
  848 tz 0 0  214.15  826.19   301.3  301.3
  849 tz 0 0  181.28  731.74   401.3  401.3
  850 tz 0 0  202.19  542.9    591.3  591.3
  871 kz -1339.917  0.7345  1
c
c    ----------------------------------
c    |   back wall contour ib --> ob   |
c    ----------------------------------
c
   51 kz  1380.5  0.081633  -1
   52 tz 0 0  41.51  1291.05 875.  875.
   54 cz 440.95
   55 tz 0 0 424.65 741.0   300.  300.
   56 tz 0 0 473.98 652.87  199.  199.
   57 tz 0 0 283.7  695.5   394.  394.
   58 tz 0 0 66.89  597.66  634.  634.
   59 tz 0 0 164.51 685.57  500.  500.
   60 tz 0 0 231.57 978.19  200.  200.
   61 cz 1178.19
   62 cz 1186.19
   63 tz 0 0 14.64  978.19  200.  200.
   64 tz 0 0 14.64  978.19  208.  208.
   65 kz -1667.25   0.53      1
   66 kz -1680.92   0.53      1
   67 tz 0 0 -372.5 874.28   50.   50.
c
c    ----------------------------------------
c    | cylinders for plasma chamber/blanket |
c    ----------------------------------------
c
   41 cz 612.66
   43 cz 700.0
   45 cz 820.0
   47 cz 874.28
```

```
   50 cz 1100.0
c
c    -------------------------------
c    | planes for blanket segments |
c    -------------------------------
c
c    inb./bottom ---> top ---> outb. bottom
c
  301 pz -380.
  302 pz -343.79
  303 pz -205.0
  305 pz -153.5
  306 pz   41.51
  307 pz  391.69
  308 pz  424.65
  309 pz  544.73
  310 pz  570.
  312 pz  530.
  314 pz  376.
  315 pz  312.75
  316 pz  280.
  317 pz  231.5
  318 pz  14.64
  319 pz -105.
  320 pz -184.04
  321 pz -400.
  323 kz -606.6 22.55 1
  399 pz  137.26
c
c    -----------------------------------------
c    | planes/cyl. for vacuum vessel segments |
c    -----------------------------------------
c
c    inb./bottom ---> top ---> outb. bottom
c
  341 pz -409.5
  342 pz  428.0
  343 pz  540.0
  344 pz  572.0
  345 pz  636.0
  346 pz  408.0
  347 pz  168.0
  348 pz -416.0
  349 pz -560.0
  350 pz -512.0
  351 cz  608.0
  352 cz  864.0
  353 cz  572.0
  354 cz  616.0
  355 cz  785.0
  356 cz  888.0
  357 cz  950.0
  360 cz  548.0
c
c    -----------------------------
c    |  vacuum vessel front plate  |
c    -------------------------------
c
  101 cz  436.
  151 cz  433.
```

```
  102 tz 0 0  428.0    736.0   300.   300.
  152 tz 0 0  428.0    736.0   303.   303.
  103 tz 0 0  473.98   652.87  205.   205.
  153 tz 0 0  473.98   652.87  208.   208.
  104 tz 0 0  283.78   695.5   400.   400.
  154 tz 0 0  283.78   695.5   403.   403.
  105 tz 0 0   65.76   595.0   640.   640.
  155 tz 0 0   65.76   595.0   643.   643.
  106 tz 0 0   31.4    385.8   852.   852.
  156 tz 0 0   31.4    385.8   855.   855.
  107 tz 0 0  -459.12  807.7   205.   205.
  157 tz 0 0  -459.12  807.7   208.   208.
  108 kz  -523.5    31.5     -1
  158 kz  -526.55   31.5     -1
  109 tz 0 0  -477.25  593.78   150.  150.
  159 tz 0 0  -477.25  593.78   153.  153.
  110 tz 0 0  -409.5   885.0    449.  449.
  160 tz 0 0  -409.5   885.0    452.  452.
c
c    ---------------------------
c    | vacuum vessel back plate |
c    |            &             |
c    |  n-gamma shield (5 cm)   |
c    --------------------------
c
  201 cz  393.45
  251 cz  390.45
  271 cz  385.45
c    ---------------------------------------
  202 tz 0 0  424.0    882.0   488.55  488.55
  252 tz 0 0  424.0    882.0   491.55  491.55
  272 tz 0 0  424.0    882.0   496.55  496.55
c    ---------------------------------------
  203 tz 0 0  480.94   649.37  249.05  249.05
  253 tz 0 0  480.94   649.37  252.05  252.05
  273 tz 0 0  480.94   649.37  257.05  257.05
c    ---------------------------------------
  204 tz 0 0  288.2    687.6   445.55  445.55
  254 tz 0 0  288.2    687.6   448.55  448.55
  274 tz 0 0  288.2    687.6   453.55  453.55
c    ---------------------------------------
  205 tz 0 0   66.77   597.6   684.55  684.55
  255 tz 0 0   66.77   597.6   687.55  687.55
  275 tz 0 0   66.77   597.6   692.55  692.55
c    ---------------------------------------
  206 tz 0 0  -5.5     473.1   828.55  828.55
  256 tz 0 0  -5.5     473.1   831.55  831.55
  276 tz 0 0  -5.5     473.1   836.55  836.55
c    ---------------------------------------
  207 tz 0 0  -76.53   597.2   685.55  685.55
  257 tz 0 0  -76.53   597.2   688.55  688.55
  277 tz 0 0  -76.53   597.2   693.55  693.55
c    ---------------------------------------
  208 tz 0 0  -291.5   697.0   448.55  448.55
  258 tz 0 0  -291.5   697.0   451.55  451.55
  278 tz 0 0  -291.5   697.0   456.55  456.55
c    ---------------------------------------
  209 tz 0 0  -479.19  661.62  257.55  257.55
  259 tz 0 0  -479.19  661.62  260.55  260.55
  279 tz 0 0  -479.19  661.62  265.55  265.55
```

```
c     ---------------------------------------
   210 tz 0 0  -409.5   885.0   491.55  491.55
   260 tz 0 0  -409.5   885.0   494.55  494.55
   280 tz 0 0  -409.5   885.0   499.55  499.55
c
c     ---------------------------
c     |    front and back        |
c     |         of               |
c     |       TF coils           |
c     ---------------------------
c
   281 cz  370.45
   291 cz  272.45
c     ---------------------------------------
   282 tz 0 0  424.0    882.0   511.55  511.55
   292 tz 0 0  424.0    882.0   609.55  609.55
c     ---------------------------------------
   283 tz 0 0  480.94   649.37  272.05  272.05
   293 tz 0 0  480.94   649.37  370.05  370.05
c     ---------------------------------------
   284 tz 0 0  288.2    687.6   468.55  468.55
   294 tz 0 0  288.2    687.6   566.55  566.55
c     ---------------------------------------
   285 tz 0 0   66.77   597.6   707.55  707.55
   295 tz 0 0   66.77   597.6   805.55  805.55
c     ---------------------------------------
   286 tz 0 0  -5.5     473.1   851.55  851.55
   296 tz 0 0  -5.5     473.1   949.55  949.55
c     ---------------------------------------
   287 tz 0 0  -76.53   597.2   708.55  708.55
   297 tz 0 0  -76.53   597.2   806.55  806.55
c     ---------------------------------------
   288 tz 0 0  -291.5   697.0   471.55  471.55
   298 tz 0 0  -291.5   697.0   569.55  569.55
c     ---------------------------------------
   289 tz 0 0  -479.19  661.62  280.55  280.55
   299 tz 0 0  -479.19  661.62  378.55  378.55
c     ---------------------------------------
   290 tz 0 0  -409.5   885.0   514.55  514.55
   300 tz 0 0  -409.5   885.0   612.55  612.55
c
c     ----------------------------------------------
c     | toroidal segmentation assuming 24 TF coils  |
c     ----------------------------------------------
c
  400*   py 0
  420*   p  0.03273661 -1 0 0 $half divertor section
c        -----> side of TF coil
  435    py 58.8
c
c     ------------------------------
c     | surfaces for outside world  |
c     ------------------------------
c
  933 pz -1000.
  935 cz 1600.
  936 pz  1000.
c        ---------------------------------------
c        !      contour of divertor            !
c        ---------------------------------------
```

```
  606 tz 0 0 31.4 385.8 830 830
  607 tz 0 0 -459.12 807.7 185 185
  608 kz -503 31.5 -1
  609 tz 0 0 -477.25 593.78 130 130
  610 tz 0 0 -409.5 885 430 430
  612 kz -989.55 .7744 1
  613 kz -315.3 29 -1
  614 kz 51.58 .852 -1
  615 kz -902.7 1.462 1
   616 cz 499.1
  617 kz -849.6 2.7 1
  618 kz -362.1 42.75 -1
  619 kz 586 .465 -1
  620 kz -867.2 7.99 1
  621 kz 1354.4 .1905 -1
  622 kz -400 314.26 -1
  623 cz 980
  624 cz 905
  625 cz 835
  626 kz -32.7 2.136 -1
  627 kz -1375 1 1
  628 pz -527
  629 kz 330.6 0.37 -1
  631 kz -838.7 4.785 1
  632 kz -3.71 3.39 -1
  633 kz -460 31.5 -1
  634 kz -6710 .01235 1
  635 kz -6439 .01235 1
  636 kz -1022.9 .7744 1
  637 kz -102.7 2.64 -1
  661 kz -948 2.33 1
  662 kz 543 0.41 -1
c     -----> surfaces for divertor pumping slots
c     toroidal boundaries
  639 p .03274 -1 0 7.0037
  640 p .03274 -1 0 -7.0037
  641 p .09849 -1 0 7.0339
  642 p .09849 -1 0 -7.0339
c     at outer dump plate
  644 pz -587.5
  645 pz -599.5
  646 kz 440.8 .621 -1
  647 kz 398.8 .621 -1
c     at middle leg
  648 kz -1661.4 .49 1
  649 kz -1609.1 .49 1
  650 kz -6628.9 .01235 1
  651 kz -6520.3 .01235 1
  652 kz 583.7 .292 -1
  653 kz 520.6 .292 -1
c      at inner dump plate
  654 cz 526.5
  655 cz 500.5
  656 pz -526.5
  657 pz -514.5
c -------------------
c |  Cell Splitting |
c -------------------
1001 cz 498.1 $inner leg
1002 pz -528 $lower inner leg
```

```
 1003 kz -1026.1 1 1 $ ambiguity inner leg
 1004 kz -33.7 2.136 -1 $outer leg
 1005 cz 836 $outer leg
 1007 kz -363.1 42.75 -1 $dome

 mode  n
 imp:n 1 167r 0 11r
 thtme
 tmp    5e-3 0.01 5.8e-8 78r 4.08e-8 24r 4.94e-8 3r 7.52e-8 1r 4.94e-8
        7.52e-8  4.94e-8 2r 7.52e-8 1r 4.94e-8 1r 3.22e-8 16r 2.53e-8 9r
         3.22e-8 10r 2.53e-8 11r
 vol   1 179r
 sdef axs 0 1 0 erg d1 pos 863.54 0 162.2 rad d2 cel 10000 ext d3
 si1 2.4 2.5 13.8 14.2
 sp1 0 0.01 0 0.99
 si2 100.8
 si3 32
 c    ----------------------------------------------------------------
 c       materials definitions
 c    ----------------------------------------------------------------
m1 4009.50c 1 $Natural Beryllium
c m1 4009.50c -.99 8016.50c -.0076 13027.50c -.0004 6000.50c -.0008
c       26000.55c -.0006
c       12000.50c -.0004 14000.50c -0.0002 $S-65 Be
c m2 74000 1 $natural tungsten
c m3 6000 1 $natural carbon
m4 29000.50c 1 $natural copper
m5 82000 1 $natural lead
c 316LN Stainless Steel Fusion Engineering & Design - Tavassoli
c 66.9% Fe  17% Cr 12% Ni 2.5% Mo 1.6% Mn
m6 26000.55c -.669 24000.50c -.17 28000.50c -.12 42000.50c -.025 25055.50c -.016
c Inconel 600 (Fontana Corr Eng)
m7 28000.50c -.76 24000.50c -.16 26000.55c -.08
c Nb3Sn with Cu
m8 41093.50c .375 50120.35c .125 29000.50c .5
c    ------------------------------
c    |    Tally Ho                 |
c    ------------------------------
f14:n 206 1216 1226 204 1204 1213 1223 203 1206 1203
f24:n 1223 $upper outer dump plate
fc24  Be dpa
sd24 1141.14
e24   4.14e-7  8.76e-7  1.86e-6  3.93e-6  8.32e-6  1.76e-5  3.73e-5
      7.89e-5  1.67e-4  3.54e-4  7.48e-4  1.58e-3  3.35e-3  7.1e-3
      1.5e-2   3.18e-2  6.74e-2  1.23e-1  0.166    0.224    0.302
      0.408    0.55     0.743    1.0      1.35     1.83     2.47
      2.73     3.01     3.33     3.68     4.07     4.49     4.97
      5.49     6.07     6.7      7.41     8.19     9.05     10
      11.05    12.2     13.5     14.2
 em24 0.13608e+00 0.34349e-01 0.23622e-01 0.16231e-01 0.11156e-01
     0.76658e-02 0.52678e-02 0.30894e-01 0.98047e+00 0.28554e+01
     0.62503e+01 0.12944e+02 0.24332e+02 0.54130e+02 0.10150e+03
     0.17001e+03 0.30886e+03 0.42725e+03 0.49573e+03 0.52522e+03
     0.53536e+03 0.54441e+03 0.53143e+03 0.67853e+03 0.58125e+03
     0.51489e+03 0.37024e+03 0.35109e+03 0.58819e+03 0.69454e+03
     0.58719e+03 0.53418e+03 0.49255e+03 0.48881e+03 0.49686e+03
     0.49761e+03 0.49903e+03 0.49839e+03 0.49331e+03 0.48927e+03
     0.48550e+03 0.48034e+03 0.47326e+03 0.46427e+03 0.44900e+03
     0.44089e+03
f34:n 1213 $ outer dump plate
```

```
fc34 Be dpa in 1213
sd34 1217.165
e34   4.14e-7  8.76e-7  1.86e-6  3.93e-6  8.32e-6  1.76e-5  3.73e-5
      7.89e-5  1.67e-4  3.54e-4  7.48e-4  1.58e-3  3.35e-3  7.1e-3
      1.5e-2   3.18e-2  6.74e-2  1.23e-1  0.166    0.224    0.302
      0.408    0.55     0.743    1.0      1.35     1.83     2.47
      2.73     3.01     3.33     3.68     4.07     4.49     4.97
      5.49     6.07     6.7      7.41     8.19     9.05     10
      11.05    12.2     13.5     14.2
em34 0.13608e+00 0.34349e-01 0.23622e-01 0.16231e-01 0.11156e-01
     0.76658e-02 0.52678e-02 0.30894e-01 0.98047e+00 0.28554e+01
     0.62503e+01 0.12944e+02 0.24332e+02 0.54130e+02 0.10150e+03
     0.17001e+03 0.30886e+03 0.42725e+03 0.49573e+03 0.52522e+03
     0.53536e+03 0.54441e+03 0.53143e+03 0.67853e+03 0.58125e+03
     0.51489e+03 0.37024e+03 0.35109e+03 0.58819e+03 0.69454e+03
     0.58719e+03 0.53418e+03 0.49255e+03 0.48881e+03 0.49686e+03
     0.49761e+03 0.49903e+03 0.49839e+03 0.49331e+03 0.48927e+03
     0.48550e+03 0.48034e+03 0.47326e+03 0.46427e+03 0.44900e+03
     0.44089e+03
f44:n 1226 $lower inner dump plate
fc44 Be dpa in 1226
sd44 393.986
e44   4.14e-7  8.76e-7  1.86e-6  3.93e-6  8.32e-6  1.76e-5  3.73e-5
      7.89e-5  1.67e-4  3.54e-4  7.48e-4  1.58e-3  3.35e-3  7.1e-3
      1.5e-2   3.18e-2  6.74e-2  1.23e-1  0.166    0.224    0.302
      0.408    0.55     0.743    1.0      1.35     1.83     2.47
      2.73     3.01     3.33     3.68     4.07     4.49     4.97
      5.49     6.07     6.7      7.41     8.19     9.05     10
      11.05    12.2     13.5     14.2
em44 0.13608e+00 0.34349e-01 0.23622e-01 0.16231e-01 0.11156e-01
     0.76658e-02 0.52678e-02 0.30894e-01 0.98047e+00 0.28554e+01
     0.62503e+01 0.12944e+02 0.24332e+02 0.54130e+02 0.10150e+03
     0.17001e+03 0.30886e+03 0.42725e+03 0.49573e+03 0.52522e+03
     0.53536e+03 0.54441e+03 0.53143e+03 0.67853e+03 0.58125e+03
     0.51489e+03 0.37024e+03 0.35109e+03 0.58819e+03 0.69454e+03
     0.58719e+03 0.53418e+03 0.49255e+03 0.48881e+03 0.49686e+03
     0.49761e+03 0.49903e+03 0.49839e+03 0.49331e+03 0.48927e+03
     0.48550e+03 0.48034e+03 0.47326e+03 0.46427e+03 0.44900e+03
     0.44089e+03
f54:n 1216
fc54 Be dpa in 1216 uppper inner dump plate
sd54 628.43
e54   4.14e-7  8.76e-7  1.86e-6  3.93e-6  8.32e-6  1.76e-5  3.73e-5
      7.89e-5  1.67e-4  3.54e-4  7.48e-4  1.58e-3  3.35e-3  7.1e-3
      1.5e-2   3.18e-2  6.74e-2  1.23e-1  0.166    0.224    0.302
      0.408    0.55     0.743    1.0      1.35     1.83     2.47
      2.73     3.01     3.33     3.68     4.07     4.49     4.97
      5.49     6.07     6.7      7.41     8.19     9.05     10
      11.05    12.2     13.5     14.2
em54 0.13608e+00 0.34349e-01 0.23622e-01 0.16231e-01 0.11156e-01
     0.76658e-02 0.52678e-02 0.30894e-01 0.98047e+00 0.28554e+01
     0.62503e+01 0.12944e+02 0.24332e+02 0.54130e+02 0.10150e+03
     0.17001e+03 0.30886e+03 0.42725e+03 0.49573e+03 0.52522e+03
     0.53536e+03 0.54441e+03 0.53143e+03 0.67853e+03 0.58125e+03
     0.51489e+03 0.37024e+03 0.35109e+03 0.58819e+03 0.69454e+03
     0.58719e+03 0.53418e+03 0.49255e+03 0.48881e+03 0.49686e+03
     0.49761e+03 0.49903e+03 0.49839e+03 0.49331e+03 0.48927e+03
     0.48550e+03 0.48034e+03 0.47326e+03 0.46427e+03 0.44900e+03
     0.44089e+03
f64:n 1204
```

```
fc64 Be dpa in Dome armor
sd64 2058.93
e64   4.14e-7  8.76e-7  1.86e-6  3.93e-6  8.32e-6  1.76e-5  3.73e-5
      7.89e-5  1.67e-4  3.54e-4  7.48e-4  1.58e-3  3.35e-3  7.1e-3
      1.5e-2   3.18e-2  6.74e-2  1.23e-1  0.166    0.224    0.302
      0.408    0.55     0.743    1.0      1.35     1.83     2.47
      2.73     3.01     3.33     3.68     4.07     4.49     4.97
      5.49     6.07     6.7      7.41     8.19     9.05     10
      11.05    12.2     13.5     14.2
em64 0.13608e+00 0.34349e-01 0.23622e-01 0.16231e-01 0.11156e-01
     0.76658e-02 0.52678e-02 0.30894e-01 0.98047e+00 0.28554e+01
     0.62503e+01 0.12944e+02 0.24332e+02 0.54130e+02 0.10150e+03
     0.17001e+03 0.30886e+03 0.42725e+03 0.49573e+03 0.52522e+03
     0.53536e+03 0.54441e+03 0.53143e+03 0.67853e+03 0.58125e+03
     0.51489e+03 0.37024e+03 0.35109e+03 0.58819e+03 0.69454e+03
     0.58719e+03 0.53418e+03 0.49255e+03 0.48881e+03 0.49686e+03
     0.49761e+03 0.49903e+03 0.49839e+03 0.49331e+03 0.48927e+03
     0.48550e+03 0.48034e+03 0.47326e+03 0.46427e+03 0.44900e+03
     0.44089e+03
f74:n 1223 $upper outer dump
fc74 He production in Be
sd74 1141.14
e74   4.14e-7  8.76e-7  1.86e-6  3.93e-6  8.32e-6  1.76e-5  3.73e-5
      7.89e-5  1.67e-4  3.54e-4  7.48e-4  1.58e-3  3.35e-3  7.1e-3
      1.5e-2   3.18e-2  6.74e-2  1.23e-1  0.166    0.224    0.302
      0.408    0.55     0.743    1.0      1.35     1.83     2.47
      2.73     3.01     3.33     3.68     4.07     4.49     4.97
      5.49     6.07     6.7      7.41     8.19     9.05     10
      11.05    12.2     13.5     14.2
em74 0.          0.          0.          0.          0.          0.
     0.          0.          0.          0.          0.          0.
     0.          0.          0.          0.          0.          0.
     0.          0.          0           0           0           0.38310e-05
     0.15900e-02 0.54780e-02 0.20850e-01 0.70440e-01 0.16230e+00 0.57090e+00
     0.87580e+00 0.10280e+01 0.11040e+01 0.11420e+01 0.11670e+01 0.11870e+01
     0.12040e+01 0.12050e+01 0.11890e+01 0.11780e+01 0.11670e+01 0.11560e+01
     0.11430e+01 0.11250e+01 0.10760e+01 0.10520e+01
f84:n 1213 $lower outer dump plate
fc84 He production in Be
sd84 1217.165
e84   4.14e-7  8.76e-7  1.86e-6  3.93e-6  8.32e-6  1.76e-5  3.73e-5
      7.89e-5  1.67e-4  3.54e-4  7.48e-4  1.58e-3  3.35e-3  7.1e-3
      1.5e-2   3.18e-2  6.74e-2  1.23e-1  0.166    0.224    0.302
      0.408    0.55     0.743    1.0      1.35     1.83     2.47
      2.73     3.01     3.33     3.68     4.07     4.49     4.97
      5.49     6.07     6.7      7.41     8.19     9.05     10
      11.05    12.2     13.5     14.2
em84 0.          0.          0.          0.          0.          0.
     0.          0.          0.          0.          0.          0.
     0.          0.          0.          0.          0.          0.
     0.          0.          0           0           0           0.38310e-05
     0.15900e-02 0.54780e-02 0.20850e-01 0.70440e-01 0.16230e+00 0.57090e+00
     0.87580e+00 0.10280e+01 0.11040e+01 0.11420e+01 0.11670e+01 0.11870e+01
     0.12040e+01 0.12050e+01 0.11890e+01 0.11780e+01 0.11670e+01 0.11560e+01
     0.11430e+01 0.11250e+01 0.10760e+01 0.10520e+01
f94:n 1226 $lower inner dump plate
fc94 He production in Be
sd94 393.986
e94   4.14e-7  8.76e-7  1.86e-6  3.93e-6  8.32e-6  1.76e-5  3.73e-5
      7.89e-5  1.67e-4  3.54e-4  7.48e-4  1.58e-3  3.35e-3  7.1e-3
```

```
      1.5e-2   3.18e-2  6.74e-2  1.23e-1  0.166    0.224    0.302
      0.408    0.55     0.743    1.0      1.35     1.83     2.47
      2.73     3.01     3.33     3.68     4.07     4.49     4.97
      5.49     6.07     6.7      7.41     8.19     9.05     10
      11.05    12.2     13.5     14.2
em94 0.          0.          0.          0.          0.          0.
     0.          0.          0.          0.          0.          0.
     0.          0.          0.          0.          0.          0.
     0.          0.          0           0           0           0.38310e-05
     0.15900e-02 0.54780e-02 0.20850e-01 0.70440e-01 0.16230e+00 0.57090e+00
     0.87580e+00 0.10280e+01 0.11040e+01 0.11420e+01 0.11670e+01 0.11870e+01
     0.12040e+01 0.12050e+01 0.11890e+01 0.11780e+01 0.11670e+01 0.11560e+01
     0.11430e+01 0.11250e+01 0.10760e+01 0.10520e+01
f104:n 1216 $upper inner dump plate
fc104 He production in Be
sd104 628.43
e104  4.14e-7  8.76e-7  1.86e-6  3.93e-6  8.32e-6  1.76e-5  3.73e-5
      7.89e-5  1.67e-4  3.54e-4  7.48e-4  1.58e-3  3.35e-3  7.1e-3
      1.5e-2   3.18e-2  6.74e-2  1.23e-1  0.166    0.224    0.302
      0.408    0.55     0.743    1.0      1.35     1.83     2.47
      2.73     3.01     3.33     3.68     4.07     4.49     4.97
      5.49     6.07     6.7      7.41     8.19     9.05     10
      11.05    12.2     13.5     14.2
em104 0.          0.          0.          0.          0.          0.
      0.          0.          0.          0.          0.          0.
      0.          0.          0.          0.          0.          0.
      0.          0.          0           0           0           0.38310e-05
      0.15900e-02 0.54780e-02 0.20850e-01 0.70440e-01 0.16230e+00 0.57090e+00
      0.87580e+00 0.10280e+01 0.11040e+01 0.11420e+01 0.11670e+01 0.11870e+01
      0.12040e+01 0.12050e+01 0.11890e+01 0.11780e+01 0.11670e+01 0.11560e+01
      0.11430e+01 0.11250e+01 0.10760e+01 0.10520e+01
f114:n 1204 $Dome armor
fc114 He production in Be
sd114 2058.93
e114  4.14e-7  8.76e-7  1.86e-6  3.93e-6  8.32e-6  1.76e-5  3.73e-5
      7.89e-5  1.67e-4  3.54e-4  7.48e-4  1.58e-3  3.35e-3  7.1e-3
      1.5e-2   3.18e-2  6.74e-2  1.23e-1  0.166    0.224    0.302
      0.408    0.55     0.743    1.0      1.35     1.83     2.47
      2.73     3.01     3.33     3.68     4.07     4.49     4.97
      5.49     6.07     6.7      7.41     8.19     9.05     10
      11.05    12.2     13.5     14.2
em114 0.          0.          0.          0.          0.          0.
      0.          0.          0.          0.          0.          0.
      0.          0.          0.          0.          0.          0.
      0.          0.          0           0           0           0.38310e-05
      0.15900e-02 0.54780e-02 0.20850e-01 0.70440e-01 0.16230e+00 0.57090e+00
      0.87580e+00 0.10280e+01 0.11040e+01 0.11420e+01 0.11670e+01 0.11870e+01
      0.12040e+01 0.12050e+01 0.11890e+01 0.11780e+01 0.11670e+01 0.11560e+01
      0.11430e+01 0.11250e+01 0.10760e+01 0.10520e+01
f12:n 616 628 618 626 625
e12 4.14e-7  8.76e-7  1.86e-6  3.93e-6  8.32e-6  1.76e-5  3.73e-5
      7.89e-5  1.67e-4  3.54e-4  7.48e-4  1.58e-3  3.35e-3  7.1e-3
      1.5e-2   3.18e-2  6.74e-2  1.23e-1  0.166    0.224    0.302
      0.408    0.55     0.743    1.0      1.35     1.83     2.47
      2.73     3.01     3.33     3.68     4.07     4.49     4.97
      5.49     6.07     6.7      7.41     8.19     9.05     10
      11.05    12.2     13.5     14.2
sd12 628.43 393.986 2058.93 1217.165 1141.14
idum  101 151 1
rdum  8. 9.3333333 400. -700.
```

```
c
c     ---------------
c     ---------------
files  21 srcdat s f 0
nps 200000
c ctme  9.
print
```

APPENDIX B

Materials Supplier Information

In this appendix, the information supplied by the manufacturers of the candidate armor materials, i.e. Toyo Tanso IG-11 Graphite, CLIMAX Specialty Metals WP-1 Tungsten plate and Brush Wellman S-65 grade Beryllium, is listed.

B.1 Toyo Tanso IG-11 Isotropic Graphite

Typical Grades / Properties

	Bulk density	Hardness	Specific Resistivity μΩ cm	μΩ·m	Flexural Strength kg/cm²	MPa	Compressive Strength kg/cm²	MPa	Tensile Strength kg/cm²	MPa	Modulus of Elasticity kg/mm²	GPa	C. T. E. 10^{-6}/°C 10^{-6}/K	Thermal Conductivity kcal/m·h·c	W/(m·k)
IG-11	1.77	55	1100	11.0	400	39	800	80	250	25	1000	10	4.6	100	115
IG-12	1.77	60	1150	11.5	460	45	900	90	290	28	1100	10	4.7	90	105
IG11P	1.83	60	1000	10.0	470	46	950	95			1150	11	4.6		
IG-14	1.85	60	1000	10.0	450	44	850	85	270	26	1100	11	4.7	115	135
IG-15	1.90	60	950	9.5	500	49	1050	105	300	29	1200	12	4.8	120	140
IG-43	1.82	55	900	9.0	550	54	900	90	380	37	1150	11	4.8	120	140
IG-56	1.77	60	1250	12.5	440	43	900	90	280	27	1050	10	4.7	90	105
IG-70	1.85	65	1000	10.0	530	52	1000	100	320	31	1200	12	4.6	110	130
IG-73	1.75	65	1300	13.0	450	44	1050	105	300	29	950	9	5.5	90	105
ISEM-1	1.70	50	1350	13.5	370	36	700	70	200	20	900	9	4.2	80	95
ISEM-2	1.78	55	1100	11.0	420	39	850	80	250	25	1000	10	4.6	100	115
ISEM-3	1.85	60	1000	10.0	500	49	1050	105	300	29	1200	12	4.6	110	130
ISEM-8	1.77	65	1450	14.5	500	49	1100	110	330	32	950	9	5.5	80	95
ISO-61	1.80	75	1500	15.0	630	62	1500	150	450	44	1250	12	5.2	60	70
ISO-63	1,83	85	1650	16.5	750	74	1850	180	530	52	1400	14	5.5	60	70
ISO-88	1.90	90	1500	15.0	1000	98	2000	195	750	74	1400	14	6.5	70	80
ISO-90	1.82	80	1500	15.0	720	71	1650	160			1250	12	6.3	70	80
ISO-95	1.87	90	1550	15.5	800	79	1800	175			1350	13	6.5	70	80
SIC-6	1.85	60	1000	10.0	500	49	1050	105	300	29	1200	12	5.0	110	130
SIC-10	1.78	55	1100	11.0	420	39	850	85	250	25	1000	10	4.8	100	116
SIC-12	1.77	60	1150	11.5	460	45	900	90	290	28	1100	10	4.7	90	105
KC-65	1.82	95	2100	21.0	850	83	2200	215							

Data are typical.

Notes

1. CTE data are for the temperature range of 350~450°C.
2. The above grades can be purified (typical ash contents: 10ppm), and/or high purified (2ppm) upon requirement.
3. Conversion to SI units:-

μΩ cm × 0.01 → μΩ·m
kg/mm² × 0.0098 → GPa
kg/cm² × 0.098 → MPa
Kcal/m·h·°C × 1.16 → W/(m·k)

Introduction

As the first Japanese manufacturer of high density,
fine grain isotropic graphite,
TOYO TANSO have developped top quality graphite products for
wide application range.
This brochure is intended to show the basic knowledge and characteristics
of our major isotropic grades for those who are selecting the most
suitable graphite for given application and also who examine
expansion of application of graphite.

Applications

	Metallurgy						EDM				Semiconductor (Purified Products)				
	Continius Casting Iron Casting	Non-ferrous Metal	Hot Press	Crucible	Heater	Boat Others	Rough Machin-ing	Finishing	Rression Machin-ing	Ultra-Precision Works	Crucible	Heater	SiC PyC Coating	Boat Others	Maximum Block Dimension (mm)
IG-11	◎	◎	◎	◎	◎	◎					◎	◎	◎	◎	305×635×2040、ϕ610×900
IG-12	○	◎	◎	○	◎	○					○	◎	○	◎	305×620×1000、ϕ610×775
IG-11P		◎				○									230×540×1000
IG-14		◎				○									230×540×1000
IG-15		◎				○								○	230×620×1000
IG-43		◎	○	○		○					○			○	305×620×1000、ϕ305×900
IG-56			◎	◎	◎	○					○	◎	○	◎	ϕ1100×610
IG-70	○	◎	◎	○	○	○					◎	○		○	305×620×1000、ϕ610×775
IG-73			○	○	◎	○					○	◎	○	○	305×620×1200
ISEM-1					○	○	◎							◎	305×635×2040、ϕ1000×700
ISEM-2		○			○	○	◎	○				◎		◎	305×620×1500
ISEM-3		◎			○	◎	○	◎				◎		◎	305×620×1500
ISEM-8						○	○	◎	○					○	305×620×1200
ISO-61						○		◎	◎	○				○	305×540×850
ISO-63			◎	○		◎		◎	◎	○	○	◎		◎	305×540×850
ISO-88			◎			◎			◎	◎				◎	75×260×1300、ϕ150×1800
ISO-90						○			◎	◎				○	150×150×620
ISO-95						○			◎	◎				○	75×150×460
SIC-6													◎		305×620×1500
SIC-10													◎		305×620×1500
SIC-12					◎								◎		273×765×765
KC-65						◎									(Fom jigs for glass to metal sealing)

Notes
1. Other grades for special applications are available upon requests.Please contact our agent or representative for the details.
2. Standard block sizes may change without notice.
3. ◎···Suitable ○···Applicable

High Temperature Properties (Data are for reference only)

Electrical Resistivity

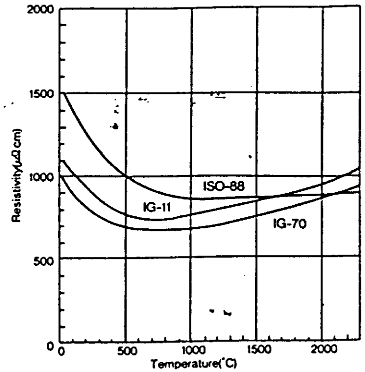

Resistivity at each temperature should be always considered when designing heaters as each grade has each characteristic.

Strength
(Grade : IG-11)

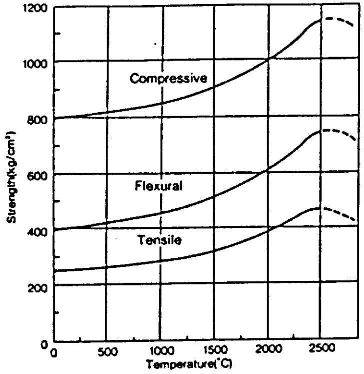

A remarkable feature with graphite compared with other engineering materials is that strength increases according as the temperature rises(till 2500°C) and the maximum strength becomes almost double of that at room temperature. Thus graphite is considered as one of the essential materials in the high temperature applications.

Thermal Expansion

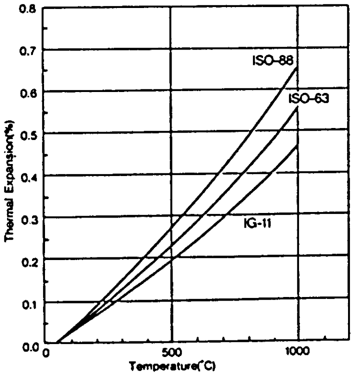

$$\text{C.T.E.}(10^{-6}/^{\circ}\text{C}) = \frac{\text{Thermal expansion ratio (\%) X } 10^{-2}}{\text{Temperature difference (}^{\circ}\text{C)}}$$

Comparison of C.T.E.

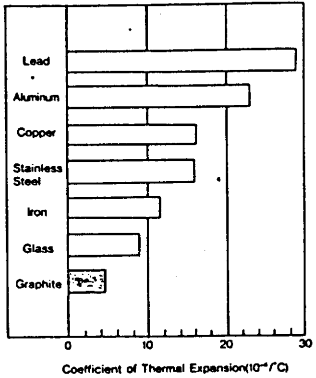

C.T.E. of graphite is much lower than general metallic materials and graphite shows dimensional stability when used at high temperature.

Thermal Conductivity

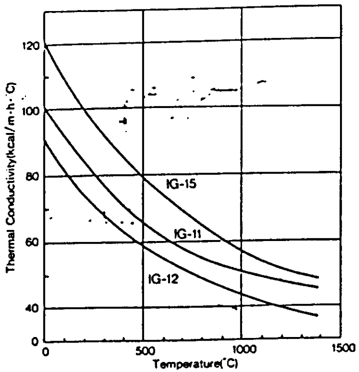

Measurement by Laser flash method

Comparison of Thermal Conductivity

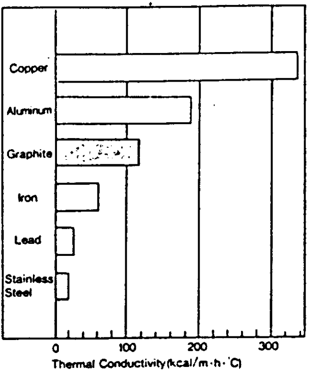

Thermal conductivity of graphite is considerably high and C.T.E. is very low. This brings superior thermal shock resistance with graphite materials. By Wiedemann Franz's law, the relation between thermal conductivity and resitivity of graphite is indicated as below:-

$$\text{Thermal conductivity(kcal/m.h.°C)} = \frac{0.1116 \times 10^6}{\text{Resistivity}(\mu\Omega\text{cm})}$$

Specific Heat

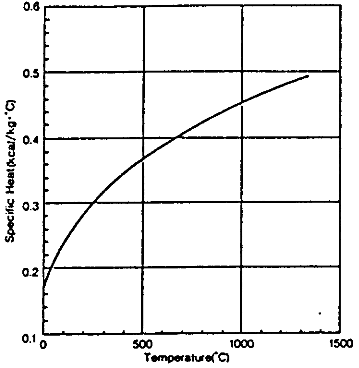

Due to anisotropy of graphite crystals, specific heat of graphite is around 1/3 of general solid. The most of thermodynamic functions are led by this essential incident. Specific heat at high temperature of graphite materials tends to have similar transition regardless of grades.

Conversion to SI units:-
kcal/(kg·°C) x 4.186 X 10^3 → J/(kg·K)

Thermal Diffusivity

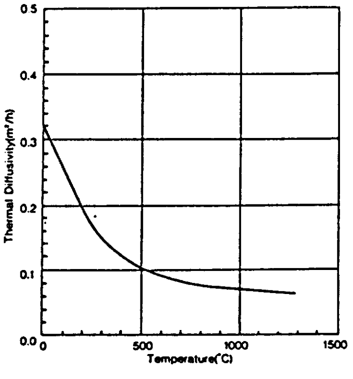

Thermal diffusivity shows thermal transitability of materials. Large thermal diffusivity indicates that the material transfers heat quickly. Graphite has extremely higher thermal diffusivity than other materials.

Conversion to SI units:-

$$\underset{(\text{m}^2/\text{h})}{\text{Thermal diffusivity}} = \frac{\text{Thermal conductivity(kcal/m.h.°C)}}{\text{Specific heat(kcal/kg·°C)} \times \text{Density(g/cm}^3)}$$

Physical Properties (Data are for reference only)

Stress Strain (Grade: IG-12)

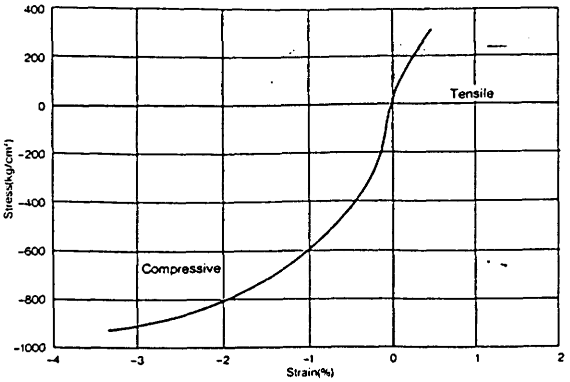

Generally, graphite shows elastic-plastic deformation. However, attention shall be paid to a charactor that fracturing behavior is different between tension and compression.
(Under tensile stress, graphite is not so strong)

Pore Size Distribution

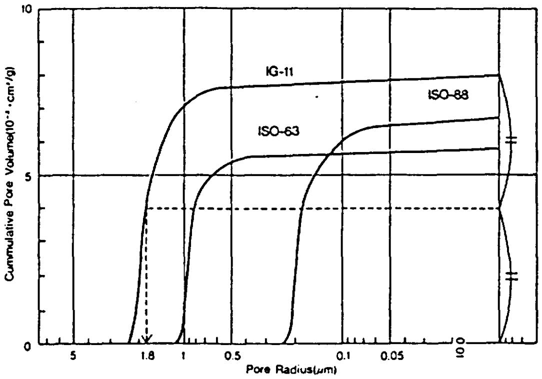

Above data are measured by mercury porosimeter. Pore distribution has a close relation with gas transmittance property and other unique propeties of graphite.

The position at 1/2 of cummulative pore volume indicates an averaged pore radius.

For Example: IG-11
$8/2 = 4 \times 10^{-2} \cdot \mathrm{cm}^3/\mathrm{g} \rightarrow 1.8\mu\mathrm{m}$

Machining Standard

Dimensional Tolerance

unit: mm

Nominal Dimension			Dimensional Tolerance
0.5	–	6	±0.1
	–	30	±0.2
	–	120	±0.3
	–	315	±0.5
	–	1000	±0.8
	–	2000	±1.2

Tolerance as per JIS B 0405-1977 to be applied, unless otherwise stated in working drawing.

Surface Roughness

Finishing Notation	Machining surface roughness		Finishing Method	JIS B 0601	
	Rmax	Ra		Rmax	Ra
▽▽▽▽	3s	0.75a	Honing Lapping	0.8s	0.2a
▽▽▽	12s	3.0a	Grinder, Lathe Milling cutter	6.3a	1.6a
▽▽	35s	8.75a	Milling cutter, Lathe	25s	6.3a
▽	100s	25.0a		100s	25.0a
–	No prescript		Band Saw	No prescript	

Graphite materials have more porous structure compared with metallic materials. Therefore, surface roughness will appear a little greater than metals.

Manufacturer may change specification without notice

Chemical Properties

Reaction Starting Temperature of Graphite in Gas Atmosphere

Atmosphere	Reaction Starting Temp.	Reaction
The air	380 – 400°C	Oxydation
Water vapor	700 – 750	ditto
CO_2	800 – 900	ditto
H_2	1000 – 1200	Methanidation
N_2	2000 – 2500	Cyanidation
CL_2	2500	(Graphite sublimates)
Ar	3000	(ditto)
Vacuum	2200	(ditto)

Although oxydation starting temperature of graphite is comparatively low in oxydation atmosphere, graphite shows chemical and thermal stability in non-oxydation atmosphere, which expands applications of graphite materials.

Reaction Starting Temperature of Graphite with Other Substances

Substance	Reaction Starting Temperature	Compound	
Al	800°C	Al_4C_3	
B	1600	B_4C	
Fe	600 – 800	Fe_3C	
Na	400 – 450	C_8Na intercalation compound (under O_2 atmosphere)	
Co	218	CoC, Co_2C	
Mo	700	Mo_2C	
Ni	1310	Carburisation into Ni	
Si	1150	SiC	
Cu	No reaction		
Mg	〃		
Pb	〃		
Sn	〃		
W	1400	W_2C, WC(under H_2 atmosphere)	
K	300	C-K or other intercalation compound	
Li	500	Li_2C_2	
Be	900	Be_2C(under vacuum or He atmosphere)	
B_2O_3	1200	CO_2 + Reduced substance	
V_2O_5	438		〃
Fe_2O_3	485		〃
TiO_2	930		〃
SiO_2	1250	SiC	〃
Al_2O_3	1280	Al_4C_3	〃
BeO	960	Be_2C	〃
MgO	1350		〃
ZrO_2	1300	ZrC	〃

Vapor Pressure

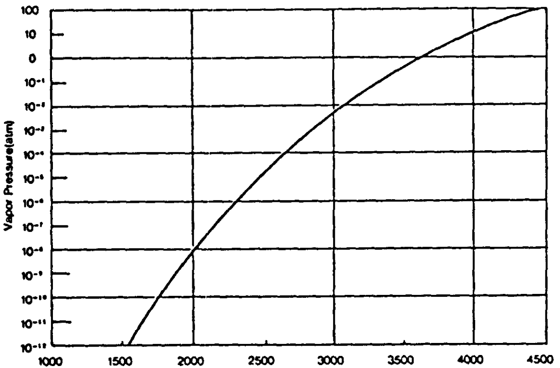

Graphite is a very stable material under 2200°C, but vapor pressure increases under higher temperature and/or lower pressure. Graphite wear by vaporization should be considered in these cases.

Gas Desorption

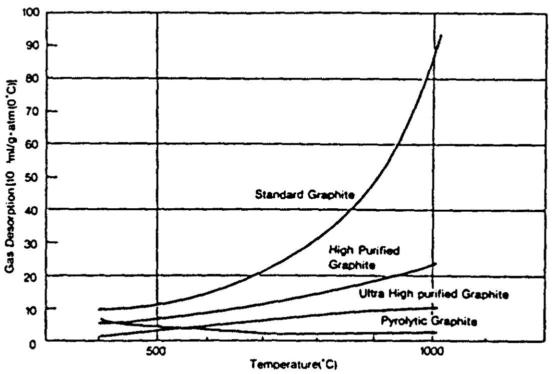

Graphite discharges absorbed gasses under high temperature atmosphere.
Applications such as semiconductor field employ pyrolytic or high purified graphite which discharges less gasses.

Typical Impurity Level(ppm)

— Not Detected

Purity Level		Elements	Al	As	B	Be	Bi	Ca	Cd	Ce	Cr	Cu	Fe	Ga	Ge	Hg	In	K	Li	Mg	Mn	Na	Ni	P	Pb	Si	Sn	Ti	Zn
Ultra High Purity	2ppm		—	—	—	—	—	—	—	—	—	—	—	—	—	—	—	—	—	—	—	—	—	—	—	—	—	—	—
High Purity	10ppm		⟨0.3	—	—	—	—	—	—	—	—	—	⟨1.0	—	—	—	—	—	—	⟨0.1	—	—	—	—	—	⟨0.1	—	—	—
General Graphite	400ppm		14	—	3	—	—	6	—	—	—	—	26	—	—	—	—	—	—	0.2	—	—	4	—	—	2	—	33	—

The ash content of standard graphite is about 400 ppm but applications such as semiconductor usually call for higher purity. For these requirements, we can reduce impurity level into a few ppm by halogenation treatment at high temperature.

B.2 CLIMAX Specialty Metals Pure Tungsten Plate WP-1

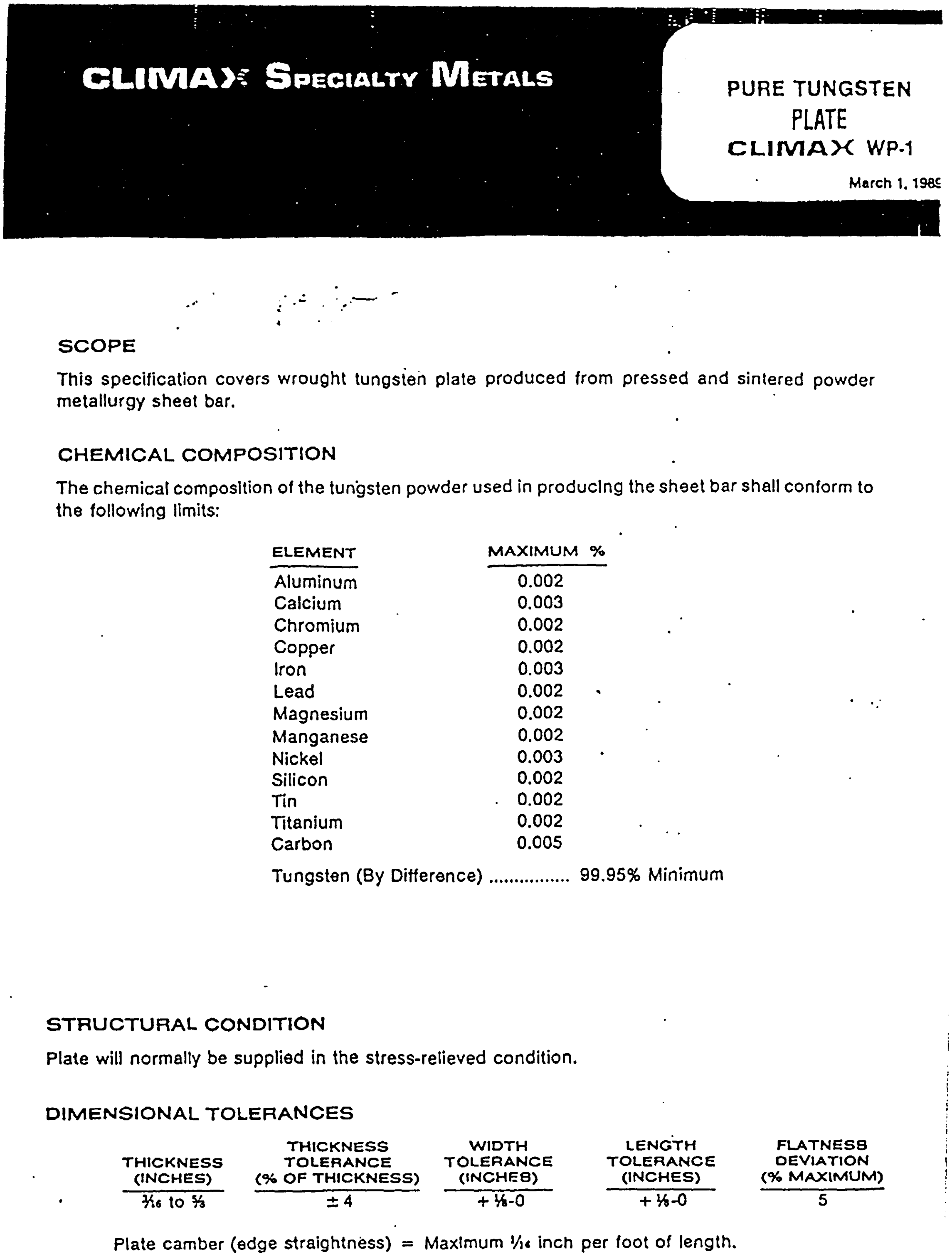

CLIMAX SPECIALTY METALS

PURE TUNGSTEN
PLATE
CLIMAX WP-1
March 1, 198

SCOPE

This specification covers wrought tungsten plate produced from pressed and sintered powder metallurgy sheet bar.

CHEMICAL COMPOSITION

The chemical composition of the tungsten powder used in producing the sheet bar shall conform to the following limits:

ELEMENT	MAXIMUM %
Aluminum	0.002
Calcium	0.003
Chromium	0.002
Copper	0.002
Iron	0.003
Lead	0.002
Magnesium	0.002
Manganese	0.002
Nickel	0.003
Silicon	0.002
Tin	0.002
Titanium	0.002
Carbon	0.005

Tungsten (By Difference) .... 99.95% Minimum

STRUCTURAL CONDITION

Plate will normally be supplied in the stress-relieved condition.

DIMENSIONAL TOLERANCES

THICKNESS (INCHES)	THICKNESS TOLERANCE (% OF THICKNESS)	WIDTH TOLERANCE (INCHES)	LENGTH TOLERANCE (INCHES)	FLATNESS DEVIATION (% MAXIMUM)
3/16 to 5/8	± 4	+ 1/8-0	+ 1/8-0	5

Plate camber (edge straightness) = Maximum 1/16 inch per foot of length.

DIMENSIONAL TOLERANCES (continued)

The deviation from flatness is determined by the formula:

$$H/L \times 100 = \%\ \text{Flatness Deviation}$$

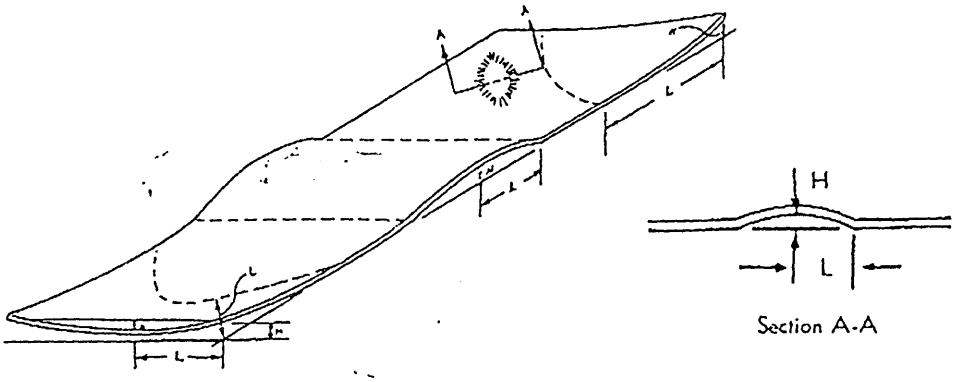

H — Maximum vertical distance between flat surface and lower surface of sheet.

L — Minimum horizontal distance between highest point on sheet and point of contact with flat surface.

SURFACE CONDITION

Tungsten plate is normally supplied with a uniform matte finish, clean and free of foreign matter. Minor surface defects will be removed by grinding, provided the conditioning does not reduce dimensions beyond the specified tolerance.

IDENTIFICATION

Material will be identified with the specification number, powder lot number and nominal size. Shipping containers will be identified with name of the customer and the purchase order number.

REJECTION

CLIMAX SPECIALTY METALS must receive written notification of rejected material with the reason for rejection. The right is reserved to inspect rejected material at customer plant for claim validation and material may be returned only after proper authorization.

B.3 Brush Wellman S-65 Structural Grade Beryllium Block

BRUSHWELLMAN
ENGINEERED MATERIALS
Brush Wellman Inc. • Elmore Ohio 43416 • Phone 419/862-2745 • TWX 810/490-2300

S-65 STRUCTURAL GRADE BERYLLIUM BLOCK

Effective: July 1, 1987
Revision: C
Supersedes: S-65, Rev. B, 6/15/83

1. SCOPE

1.1 This specification defines the requirements for a structural grade of hot pressed beryllium block which is designated S-65. This material is recommended for applications requiring high ductility.

2. CHEMICAL COMPOSITION

2.1 The chemical composition shall conform to the following:

w/o

Beryllium Assay, % minimum (1)	99.0
Beryllium Oxide, % maximum (2)	1.0
Aluminum, % maximum (3)	0.06
Carbon, % maximum (4)	0.10
Iron, % maximum (3)	0.08
Magnesium, % maximum (3)	0.06
Silicon, % maximum (3)	0.06
Other Metallic Impurities, % maximum (3)	0.04

Note: (1) Difference (i.e. 100%-other elements)
(2) Leco Inert Gas Fusion
(3) DC plasma emission spectrometry
(4) Leco Combustion

3. DENSITY

3.1 The minimum bulk density shall be 99.0% Theoretical Density.

3.2 The theoretical density is to be calculated using the following formula:

$$\text{Theoretical Density} = \frac{100}{\frac{100-\%\text{BeO}}{1.8477} + \frac{\%\text{BeO}}{3.009}}\ \%$$

3.3 Density shall be determined using the water displacement method.

4. TENSILE PROPERTIES

4.1 Minimum tensile properties for the material at room temperature, as determined per ASTM E-8, and MAB-205 M shall be:

Ultimate Tensile Strength, psi, minimum	42,000
Yield Strength (0.2% offset), psi, minimum	30,000
Elongation (% in 4 diameters), minimum	3.0

TABLE I — PHYSICAL PROPERTIES

• Atomic Number	4	• Reflectivity:	Optical reflectivity 50%, ultraviolet reflectivity 55%, infrared (10.6 um) reflectivity 98%.
• Atomic Weight:	9.02		
• Latent Heat of Fusion:	560 BTU/lb.	• Sonic Velocity:	Velocity of sound in beryllium is 41,300 ft./sec., two and one-half times that in steel.
• Specific Gravity:	1.85 grams/cc	• X-ray Transparency:	Due to its low atomic number, beryllium transmits x-rays seventeen times better than an equivalent thickness of aluminum. Beryllium x-ray windows allow the most efficient use of generated radiation in medical and analytical applications.
• Melting Point:	2345 F (1285 C)		
• Electrical Conductivity:	40.7% of IACS		
• Magnetic Characteristics:	Beryllium is diamagnetic, -1.0×10^{6} CgS units		

TABLE II — THERMAL PROPERTIES COMPARISON AT ROOM TEMPERATURE

Metal	Specific Heat $\left[\frac{\text{BTU}}{\text{lb. }^\circ\text{F}}\right]$	Melting Point [°F]	Thermal Conductivity $\left[\frac{\text{BTU-ft}}{\text{hr. ft}^2\ ^\circ\text{F}}\right]$	Coeff. of Linear Expan. $[\times 10^{-6}$ in/in/°F]
Beryllium	0.46	2345	104	6.4
Aluminum	0.22	1220	128	13.1
Steel	0.12	2800	27	8.3
Copper	0.09	1980	226	9.8
2124 T6-30% V/O SiC	0.19	1220	72	7.5
2024 T6-25% V/O F-9	0.20	1220	89	9.1

APPENDIX C

DKR-PULSAR Input Files

C.1 Toyo Tanso IG-11

indkrC

```
DKR run for IG-11 Graphite
1 1 1 1 5 5 1 0 5 1 1
2 0 0 0 0 2 1 0 0
3.0 1.0 1.0 3000 1.0e-24
100.0 100.1 0.0 4.0e-9 1000.0
1 1.0 1.0
'pulsar'
2 2
1000 1000.0 2200.0
1 0.0 0.0
'one-d'
5
100.0 876495.52 1811278.24 2113858.72 2596492.96 4177751.2
1 1 1 1 1
1 1 1
2 1 1
3 1 1
4 1 1
5 1 1
'Graphite'
1 1 1 1 1
1.0
1 6 1 8.88e+22
1 12 1 4.38e+15
1 13 1 1.184e+16
1 14 1 3.79e+15
1 26 1 1.9e+16
1000 s
1000.0
Cell averaged flux for 14top
1.99e+13 2.19e+12 1.18e+12 9.66e+11 7.47e+11 9.05e+11 5.96e+11 8.76e+11
6.75e+11 5.92e+11 6.61e+11 6.93e+11 7.09e+11 7.41e+11 7.64e+11 9.18e+11 9.67e+11
1.38e+12 5.03e+12 6.46e+12 8.5e+12 1.08e+13 1.39e+13 1.63e+13 1.81e+13 1.96e+13
1.92e+13 1.9e+13 3.6e+13 4.02e+13 3.47e+13 3.1e+13 2.59e+13 2.17e+13 2.0e+13 1.68e+13
1.34e+13 1.19e+13 1.05e+13 8.9e+12 7.41e+12 5.97e+12 4.62e+12 3.38e+12 2.28e+12 2.07e+12
```

C.1.1 IG-11 Fluxin File

```
fluxinC

int     1
3.8e+12 5.8e+11 2.48e+11 2.09e+11 1.99e+11 3.17e+11 1.54e+11 2.47e+11
1.74e+11 1.52e+11 1.81e+11 2.03e+11 1.63e+11 2.23e+11 2.06e+11 2.31e+11
1.89e+11 3.55e+11 1.2e+12 1.8e+12 2.43e+12 3.16e+12 4.25e+12 4.95e+12
6.01e+12 6.69e+12 6.78e+12 6.82e+12 1.37e+13 1.71e+13 1.62e+13 1.54e+13
1.34e+13 1.21e+13 1.18e+13 1.01e+13 8.63e+12 7.72e+12 7.07e+12 6.11e+12
5.24e+12 4.17e+12 3.39e+12 2.48e+12 1.69e+12 1.71e+12
int     2
4.37e+12 5.03e+11 2.81e+11 2.68e+11 1.74e+11 2.55e+11 1.19e+11 1.71e+11
1.87e+11 1.57e+11 1.79e+11 2.34e+11 1.55e+11 2.03e+11 1.69e+11 2.34e+11
2.3e+11 3.81e+11 1.26e+12 1.73e+12 2.52e+12 3.24e+12 4.55e+12 5.25e+12
5.94e+12 7.05e+12 7.05e+12 7.3e+12 1.5e+13 1.77e+13 1.75e+13 1.64e+13
1.44e+13 1.32e+13 1.27e+13 1.11e+13 9.15e+12 8.55e+12 7.62e+12 6.67e+12
5.74e+12 4.7e+12 3.54e+12 2.69e+12 1.86e+12 1.7e+12
int     3
6.22e+11 3.82e+11 9.23e+10 1.5e+11 1.59e+11 1.93e+11 1.45e+11 1.03e+11
1.44e+11 9.55e+10 1.51e+11 2.35e+11 1.39e+11 1.96e+11 1.58e+11 1.24e+11 1.86e+11
2.88e+11 1.14e+12 1.94e+12 2.47e+12 2.99e+12 4.58e+12 5.25e+12 6.39e+12 7.52e+12
7.37e+12 7.55e+12 1.5e+13 1.79e+13 1.69e+13 1.54e+13 1.29e+13 1.11e+13 1.12e+13
9.55e+12 7.73e+12 7.08e+12 6.37e+12 5.34e+12 4.42e+12 3.6e+12 2.78e+12 2.19e+12 1.34e+12 1.0e+12
int     4
2.3e+11 3.12e+11 1.7e+11 2.02e+11 2.12e+11 1.64e+11 1.13e+11 1.55e+11
7.88e+10 1.7e+11 1.6e+11 1.45e+11 1.83e+11 1.95e+11 2.22e+11 1.72e+11
2.05e+11 2.71e+11 1.31e+12 1.81e+12 3.04e+12 3.95e+12 5.45e+12 6.62e+12
7.71e+12 8.94e+12 8.81e+12 8.94e+12 1.77e+13 2.19e+13 2.08e+13 1.85e+13
1.59e+13 1.43e+13 1.37e+13 1.16e+13 9.2e+12 8.54e+12
7.7e+12 6.4e+12 5.41e+12 4.6e+12 3.62e+12 2.5e+12 1.47e+12 1.4e+12
int     5
1.99e+13 2.19e+12 1.18e+12 9.66e+11 7.47e+11 9.05e+11 5.96e+11 8.76e+11
6.75e+11 5.92e+11 6.61e+11 6.93e+11 7.09e+11 7.41e+11 7.64e+11 9.18e+11 9.67e+11
1.38e+12 5.03e+12 6.46e+12 8.5e+12 1.08e+13 1.39e+13 1.63e+13 1.81e+13 1.96e+13
1.92e+13 1.9e+13 3.6e+13 4.02e+13 3.47e+13 3.1e+13 2.59e+13 2.17e+13 2.0e+13 1.68e+13
1.34e+13 1.19e+13 1.05e+13 8.9e+12 7.41e+12 5.97e+12 4.62e+12 3.38e+12 2.28e+12 2.07e+12
```

C.2.1 Tungsten Fluxin File

```
W-FLUX

int     1
4.00e+12 3.29e+11 5.66e+10 8.7e+10 1.28e+11 1.26e+11 1.03e+11 1.15e+11
9.7e+10 1.01e+11 1.2e+11  1.56e+11 1.6e+11 2.33e+11 1.93e+11 1.86e+11
2.3e+11 2.95e+11 1.16e+12 1.72e+12 2.71e+12 4.27e+12 6.83e+12 7.78e+12
8.64e+12 9.75e+12 9.12e+12 8.84e+12 1.73e+13 1.76e+13 1.5e+13  1.22e+13
8.47e+12 7.19e+12 5.51e+12 3.56e+12 2.73e+12 2.96e+12 2.56e+12 1.05e+12
7.95e+11 5.12e+11 4.9e+11  4.45e+11 1.99e+11 1.22e+11
int     2
4.73e+12 2.43e+11 6.31e+10 1.06e+11 1.04e+11 9.88e+10 1.01e+11 6.37e+10
1.02e+11 8.97e+10 1.23e+11 1.34e+11 1.36e+11 1.52e+11 1.87e+11 2.32e+11
2.5e+11 3.09e+11 1.17e+12 1.83e+12 2.72e+12 4.19e+12 6.68e+12 7.9e+12
8.94e+12 9.87e+12 9.25e+12 9.47e+12 1.78e+13 1.86e+13 1.58e+13 1.24e+13
9.24e+12 8.05e+12 6.02e+12 4.07e+12 3.19e+12 3.21e+12 2.9e+12  1.14e+12
9.95e+11 6.42e+11 5.55e+11 4.53e+11 2.26e+11 1.48e+11
int     3
5.72e+11 2.77e+11 7.93e+10 1.1e+11 1.0e+11 1.54e+11 9.1e+10 7.72e+10
9.53e+10 1.04e+11 1.39e+11 2.15e+11 1.25e+11 2.31e+11 1.22e+11 1.07e+11
1.73e+11 2.12e+11 1.06e+12 1.53e+12 2.72e+12 4.09e+12 6.35e+12 7.61e+12
8.26e+12 1.01e+13 9.13e+12 9.01e+12 1.67e+13 1.67e+13 1.52e+13 1.21e+13
8.91e+12 8.28e+12 6.22e+12 4.32e+12 3.36e+12 3.65e+12 2.81e+12 1.09e+12
1.13e+12 7.06e+11 4.82e+11 4.18e+11 2.68e+11 1.59e+11
int     4
2.24e+11 3.43e+11 1.4e+11 2.19e+11 1.48e+11 1.4e+11 5.82e+10 6.77e+10
6.93e+10 1.39e+11 1.62e+11 1.59e+11 1.68e+11 1.84e+11 2.0e+11 2.43e+11
2.75e+11 2.55e+11 1.31e+12 2.03e+12 3.49e+12 5.11e+12 8.11e+12 9.07e+12
1.17e+13 1.36e+13 1.17e+13 1.29e+13 2.33e+13 2.42e+13 2.09e+13 1.63e+13
1.22e+13 1.14e+13 8.18e+12 6.03e+12 4.79e+12 4.87e+12 4.3e+12 1.58e+12
 1.38e+12 1.07e+12 8.34e+11 7.2e+11 3.78e+11 2.37e+11
int     5
2.25e+13 1.28e+12 3.32e+11 5.09e+11 5.15e+11 3.88e+11 4.03e+11 4.09e+11
4.46e+11 4.72e+11 4.78e+11 5.26e+11 6.58e+11 7.36e+11 8.3e+11 8.52e+11
9.29e+11 1.21e+12 5.04e+12 7.29e+12 1.08e+13 1.49e+13 2.01e+13 2.29e+13
2.49e+13 2.55e+13 2.3e+13 2.18e+13 3.91e+13 4.05e+13 3.26e+13 2.69e+13
1.95e+13 1.63e+13 1.27e+13 8.82e+12 6.9e+12 7.13e+12 6.09e+12 2.63e+12
2.38e+12 1.7e+12 1.55e+12 1.29e+12 7.8e+11 4.8e+11
```

C.3 Brush Wellman S-65 Beryllium

```
indkrBe

DKR run for S-65 Beryllium
1 1 1 1 5 5 1 0 7 1 1
0 0 0 0 0 2 1 0 0
3.0 1.0 1.0 1.0 1.0e-24
100.0 100.1 0.0 4.0e-9 1000.0
1 1.0 1.0
'pulsar'
2 2
1000 1000.0 2200.0
1 0.0 0.0
'one-d'
5
100.0 219198.88 452894.56 528539.872 649198.432 1044512.992
1 1 1 1 1
1 1 1
2 1 1
3 1 1
4 1 1
5 1 1
'Beryl'
1 1 1 1 1
1.0
1 4 1 1.24e+23
1 6 1 9.283e+19
1 8 1 5.588e+20
1 12 1 2.75e+19
1 13 1 2.476e+19
1 14 1 2.38e+19
1 26 1 1.592e+19
1000 s
1000.0
Cell averaged flux for Beryllium Dome
4.76e+13 6.55e+12 7.17e+12 8.03e+12 9.10e+12 1.05e+13 1.19e+13 1.37e+13 1.53e+13 1.69e+13
1.93e+13 2.20e+13 2.39e+13 2.63e+13 2.98e+13 3.38e+13 3.61e+13 3.10e+13 1.60e+13 1.61e+13
1.70e+13 1.61e+13 1.45e+13 1.15e+13 9.66e+12 8.20e+12 7.34e+12 4.95e+12 1.12e+12 8.62e+11
9.61e+11 1.02e+12 1.15e+12 1.16e+12 1.16e+12 1.11e+12 1.06e+12 9.11e+11 1.02e+12 1.15e+12
1.31e+12 1.57e+12 1.62e+12 9.51e+11 2.18e+12 2.22e+13
```

C.2 Climax Specialty Metals Tungsten

indkrW

```
DKR run for Tungsten
1 1 1 1 5 5 1 0 14 1 1
0 0 0 0 0 2 1 0 0
3.0 1.0 1.0 1.0 1.0e-24
100.0 100.1 0.0 4.0e-9 1000.0
1 1.0 1.0
'pulsar'
2 2
1000 1000.0 2200.0
1 0.0 0.0
'one-d'
5
100.0 219198.88 452894.56 528539.872 649198.432 1044512.992
1 1 1 1 1
1 1 1
2 1 1
3 1 1
4 1 1
5 1 1
'Tungsten'
1 1 1 1 1
1.0
1 6 1 4.838e+19
1 12 1 9.6e+18
1 13 1 8.605e+18
1 14 1 8.273e+18
1 20 1 8.713e+18
1 22 1 4.851e+18
1 24 1 4.468e+18
1 25 1 4.225e+18
1 26 1 6.224e+18
1 28 1 5.938e+18
1 29 1 3.659e+18
1 50 1 1.958e+18
1 74 1 6.31e+22
1 82 1 1.12e+18
1000 s
1000.0
Cell averaged flux for Tungsten Dome
2.25e+13 1.28e+12 3.32e+11 5.09e+11 5.15e+11 3.88e+11 4.03e+11 4.09e+11
4.46e+11 4.72e+11 4.78e+11 5.26e+11 6.58e+11 7.36e+11 8.3e+11 8.52e+11
9.29e+11 1.21e+12 5.04e+12 7.29e+12 1.08e+13 1.49e+13 2.01e+13 2.29e+13
2.49e+13 2.55e+13 2.3e+13 2.18e+13 3.91e+13 4.05e+13 3.26e+13 2.69e+13
1.95e+13 1.63e+13 1.27e+13 8.82e+12 6.9e+12 7.13e+12 6.09e+12 2.63e+12
2.38e+12 1.7e+12 1.55e+12 1.29e+12 7.8e+11 4.8e+11
```

C.3.1 Beryllium Fluxin File

```
Be-FLUX

int     1
1.10e+12 9.65e+11 1.57e+12 2.31e+12 3.08e+12 3.68e+12 4.32e+12 5.04e+12 5.68e+12 6.36e+12
8.12e+12 9.93e+12 1.06e+13 1.25e+13 1.46e+13 1.57e+13 1.72e+13 1.45e+13 7.33e+12 7.28e+12
7.92e+12 6.86e+12 6.17e+12 4.51e+12 3.38e+12 2.37e+12 1.77e+13 1.41e+12 2.69e+11 2.04e+11
2.39e+11 2.38e+11 3.30e+11 2.70e+11 2.35e+11 1.54e+11 1.75e+11 1.84e+11 1.68e+11 1.68e+11
1.85e+11 2.63e+11 2.22e+11 2.17e+11 7.6e+11 4.04e+12
int     2
1.05e+12 9.15e+11 1.55e+12 2.28e+12 3.03e+12 3.69e+12 4.52e+12 5.37e+12 6.07e+12 6.46e+12
8.34e+12 1.06e+13 1.11e+13 1.24e+13 1.49e+13 1.62e+13 1.75e+13 1.50e+13 7.36e+12 7.58e+12
8.03e+12 7.44e+12 6.47e+12 4.71e+12 3.46e+12 2.42e+12 1.9e+12  1.31e+12 3.41e+11 1.91e+11
2.22e+11 1.99e+11 1.83e+11 1.72e+11 2.19e+11 1.49e+11 1.54e+11 1.35e+11 9.24e+10 1.55e+11
1.85e+11 2.12e+11 2.03e+11 1.77e+11 5.66e+11 4.8e+12
int     3
9.36e+11 9.14e+11 1.56e+12 2.03e+12 2.92e+12 3.29e+12 4.27e+12 5.16e+12 5.93e+12 6.46e+12
7.89e+12 1.0e+13  1.05e+13 1.21e+13 1.49e+13 1.66e+13 1.76e+13 1.53e+13 7.69e+12 7.88e+12
7.98e+12 7.51e+12 6.66e+12 5.04e+12 3.8e+12  2.60e+12 1.81e+12 1.24e+12 2.31e+11 1.82e+11
1.68e+11 1.49e+11 2.29e+11 1.64e+11 3.10e+11 1.44e+11 1.01e+11 8.70e+10 1.19e+11 1.31e+11
1.60e+11 1.03e+11 1.69e+11 9.63e+10 3.11e+11 5.75e+11
int     4
1.28e+12 1.27e+12 2.07e+12 3.11e+12 3.90e+12 4.79e+12 5.72e+12 6.76e+12 7.76e+12 8.79e+12
1.12e+13 1.39e+13 1.47e+13 1.63e+13 1.97e+13 2.27e+13 2.39e+13 2.07e+13 1.05e+13 1.06e+13
1.07e+13 9.73e+12 8.40e+12 6.39e+12 4.62e+12 3.35e+12 2.14e+12 1.45e+12 3.19e+11 2.64e+11
2.86e+11 1.85e+11 2.41e+11 1.81e+11 1.89e+11 1.60e+11 1.69e+11 8.17e+10 1.07e+11 7.34e+10
1.87e+11 2.53e+11 2.18e+11 1.66e+11 3.51e+11 2.37e+11
int     5
4.76e+13 6.55e+12 7.17e+12 8.03e+12 9.10e+12 1.05e+13 1.19e+13 1.37e+13 1.53e+13 1.69e+13
1.93e+13 2.20e+13 2.39e+13 2.63e+13 2.98e+13 3.38e+13 3.61e+13 3.10e+13 1.60e+13 1.61e+13
1.70e+13 1.61e+13 1.45e+13 1.15e+13 9.66e+12 8.20e+12 7.34e+12 4.95e+12 1.12e+12 8.62e+11
9.61e+11 1.02e+12 1.15e+12 1.16e+12 1.16e+12 1.11e+12 1.06e+12 9.11e+11 1.02e+12 1.15e+12
1.31e+12 1.57e+12 1.62e+12 9.51e+11 2.18e+12 2.22e+13
```

REFERENCES

[1] Detail of the ITER Outline Design Report: The ITER Machine Vol. II, San Diego Joint Work Site, January 10-12 1994.

[2] Janeschitz, G., Design Description Document, ITER: Garching Site, 1995.

[3] Allen, S.L. et al, "Development of a Radiative Divertor for DIII-D,". Proceedings of the November 1994 Meeting of the American Physical Society, Division of Applied Plasma Physics, Minneapolis, MN.

[4] Cohen, S.A. K.A. Werley, M.F.A. Harrison, V. Pistunovitch, A. Kukushkin, S. Krashenninikov, M. Sugihara, L.J. Perkins, R. Bulmer, D.E. Post, J.Wesley and the ITER Team, "The Status of ITER Divertor Design Concepts," Journal of Nuclear Materials, 196-198 (1992) 50-58.

[5] Granetz, R., Lecture Notes on ELMs from MIT Course 22.602, Spring 1994.

[6] Ehst, D.A. and A. Hassanein, "Dynamic Modeling of Plasma-Vapor Interactions during Plasma Disruptions," Journal of Nuclear Materials, 196-198 (1992) 680-685.

[7] Goel, B., W. Höbel, I. Landman, G. Piazza and H. Würz, Report on European ITER Task ETA-EC-DPI-1-3: Development of Divertor Materials Modelling of Off-Normal (Disruption) Plasma-Materials Interactions, "Plasma Stream Interaction: radiative energy transport and first results on divertor erosion under ITER disruptive conditions," March 4, 1994, NET PM 94-002.

[8] Sestero, A., Report on European ITER Task ETA-EC-DPI-1-3: Development of Divertor Materials Modelling of Off-Normal (Disruption) Plasma-Materials Interactions,"Formation and Evolution of a Wall Protective Plasma Shield in a Hard Disruption, March 4, 1994, NET PM 93-002.

[9] Lengyel, L., Report on European ITER Task ETA-EC-DPI-1-3: Development of Divertor Materials Modelling of Off-Normal (Disruption) Plasma-Materials Interactions, "IPP Progress Report 1993: Studies on Wall Erosion during Off-Normal (Disruptive) Tokamak Operation," March 4, 1994, NET PM 94-003.

[10] Hobel, W., "Numerical Simulation of Vapor Shielding and Range Shortening for Ions Impinging on a Divertor during Plasma Disruptions, " Journal of Nuclear Materials, 196-198 (1992) 537-542.

[11] J.W. Davis, D.E.Driemeyer., J.R. Haines and R.T. McGrath, "Engineering and Materials Issues in Designing a Cold-gas Divertor," Journal of Nuclear Materials, 212-215 (1994) 1353-1359.

[12] G. Janeschitz, K.B., G. Federici, Y. Igithanov, A. Kukushkin, H.D. Pacher, G.W. Pacher, and M. Sugihara, "The ITER Divertor Concept," Journal of Nuclear Materials, 220-222 (1995) 73-88.

[13] Driemeyer, D., Blueprints of Half Divertor Cassette, McDonnell Douglas Aerospace, St. Louis, MO, 1995.

[14] "S-65 Structural Grade Beryllium Block: Revision C, " Brush Wellman Engineered Materials, 1995.

[15] Stonehouse, A. James and James M. Marder, "Beryllium," Metals Handbook, 10th Edition, Volume 2: Properties and Selection: Nonferrous Alloys and Special-Purpose Materials, ASM International, 1990.

[16] Batsanova, A.V and L.R. Batsanova, Analytical Chemistry of Beryllium, Analytical Chemistry of Elements, ed. A.P. Vinogradov. 1969, Ann Arbor: Ann Harbor-Hunphrey Science Publishers.

[17] Material information on Pure Tungsten Plate CLIMAX WP-1. 1989, CLIMAX Specialty Metals, 1995.

[18] Yih, S.W.H., "Tungsten,"Metals Handbook, 9th Edition, Volume 2: Properties and Selection: Nonferrous Alloys and Pure Metals, ASM International, 1979.

[19] Isotropic Graphite Engineering Data, Toyo Tanso Company, Ltd.

[20] Ma, B.M., Nuclear Reactor Materials and Applications, New York: Van Nostrand Reinhold Company,1983.

[21] Robinson, M.T., "Basic Physics of Radiation Damage Production,"Journal of Nuclear Materials, 216 (1994) 1-28.

[22] Russell, K., "Phase Stability under Irradiation. " Progress in Materials Science, 28 (1984) 229-434.

[23] Gittus, J., Irradiation Effects in Crystalline Solids, Barking, Essex, England: Applied Science Publishers Ltd. , 1978.

[24] Wesson, J., Tokamaks, Claredon Press, Oxford, 1987.

[25] Wu, C.H. and U. Mszanowski, "A Comparison of Lifetimes of Beryllium, Carbon, Molybdenum and Tungsten as Divertor Armor Materials," Journal of Nuclear Materials, 218 (1995) 293-301.

[26] Dalle Donne, M., F. Scaffidi-Argentina, C. Ferrero and C. Ronchi, "Modelling of swelling and tritium release in irradiated beryllium," Journal of Nuclear Materials, 212-215 (1994) 954-960.

[27] Sannen, L., Ch. De Raedt, F. Moons and Y. Yao, "Helium content and induced swelling in neutron irradiated beryllium," Fusion Engineering and Design, 29 (1994) 470-474.

[28] D.S. Gelles, G.A. Sernyaev, M. Dalle Donne and H. Kawamura, "Radiation Effects in Beryllium used for Plasma Protection," Journal of Nuclear Materials, 212-215 (1994) 29-38.

[29] Longhurst, G.R., INEL, personal communication, Friday, October 13, 1995.

[30] S. Nomura, J.S., Y. Sasaki, T. Oku, H. Imai, M. Eto, Y. Fukuda, K. Fujisaki, Effects of Neutron Irradiation on Physical and Mechanical Properties of SM1-24 and IG-11 Graphites, February 1979, JAERI-M 8068.

[31] G.B. Engle and B.T.Kelly, "Radiation Damage of Graphite in Fission and Fusion Reactor Systems," Journal of Nuclear Materials, 122-123 (1984) 122-129.

[32]I.V. Gorynin, V.A.I., V.V. Rybin, S.A. Fabritsiev, V.A. Kazakov, V.P. Chakin, V.A. Tsykanov, V.R. Barabash and Y.G. Prokofyev, "Effects of Neutron Irradiation on Properties of Refractory Metals," Journal of Nuclear Materials, 191-194 (1992) 421-425.

[33] Breismeister, J., MCNP - A General Monte Carlo N-Particle Transport Code , LA-12625-M, November 1993, Los Alamos National Laboratory.

[34] M.E. Sawan, Y.Gohar and R. Santoro, "Shielding Analysis for the ITER Divertor and Vacuum-Pumping Ducts. " Fusion Engineering and Design, 28 (1995) 429-436.

[35] Y. Farawila, Y. Gohar and C. Maynard, "KAOS/LIB-V: A Library of Nuclear Response Functions Generated by KAOS-V Code from ENDF/B-V," Argonne National Laboratory Report ANL/FPP/TM-241 (April 1989).

[36] K. Koizlik, H.H., J. Linke, H. Nickel and E. Wallura, Neutron Irradiation of Non-Metallic First Wall Materials for Fusion Devices, Kernforschungsanlage Jülich GmbH, Institut für Reaktorwerkstoffe, Jül-2280, May 1989.

[37] Brooks, J.N., Temperature Limit of a Graphite Divertor Surface due to Particle Erosion, March 1989, ANL/FPP/TM-236.

[38] Brooks, J.N., ITER Divertor Sputtering Erosion - Recent Analysis for Carbon, Beryllium, Tungsten, and Niobium Surfaces, July 1991, ANL/FPP/TM-255.

[39] Henderson, D.L. and O. Yasar, DKRICF: A Radioactivity and Dose Rate Calculation Code Package, Vol. I,1986, University of Wisconsin Fusion Technology Institute, Madison, WI.

[40] F. William Walker, D.G.Miller, and Dr. Frank Feiner, Chart of the Nuclides, Thirteenth Edition, 1984, General Electric Company.

[41] Tavassoli, A.A., "Assessment of Austenitic Stainless Steels," Fusion Engineering & Design, 29 (1995) 371-390.

[42] Fontana, M.G., Corrosion Engineering, 1986, New York: McGraw-Hill, Inc.

6213-64